Vibrational spectroscopy as a tool to understand plant silicification

D i s s e r t a t i o n

zur Erlangung des akademischen Grades

d o c t o r r e r u m n a t u r a l i u m

(Dr. rer. nat.)

im Fach Chemie

eingereicht an der

Mathematisch-Naturwissenschaftlichen Fakultät der

Humboldt-Universität zu Berlin

von

M. Sc. Victor Manuel Rodriguez Zancajo

Präsidentin der Humboldt-Universität zu Berlin

Prof. Dr.-Ing. Dr. Sabine Kunst

Dekan der Mathematisch-Naturwissenschaftlichen Fakultät

Prof. Dr. Elmar Kulke

Gutachter/in: 1. Prof. Dr. Janina Kneipp

2. Prof. Dr. Rivka Elbaum

3. Dr. Franziska Emmerling

Tag der mündlichen Prüfung: 21 Apr 2021

Zusammenfassung

Die Ablagerung von Siliziumdioxid in Pflanzen ist ein verbreitetes Phänomen, das mit der Toleranz von Pflanzen gegenüber verschiedenen biotischen und abiotischen Belastungen korreliert. Die Pflanzen akkumulieren das amorphe Siliziumdioxid, in mikroskopisch kleinen Partikeln, den Phytolithen. Diese Ablagerung erfolgt hauptsächlich in den Zellwänden, der Mechanismus ist jedoch noch nicht aufgeklärt. Ziel dieser Arbeit ist es, am Beispiel von Blättern von Sorghumhirse ein besseres Verständnis der Prozesse zu erhalten, welche die Ablagerung von Kieselsäure in den Pflanzen steuern. Zu diesem Zweck wurden verschiedene mikroskopische und spektroskopische Methoden verwebdet, welche Informationen aus den Pflanzengeweben und molekularen Modellen in unterschiedlichen Längenskalen liefern.

Festkörper-NMR und thermogravimetrische Analyse extrahierter Blattphytolithe zeigen die Abhängigkeit der molekularen Struktur von der jeweilingen Extraktionsmethode. Abhängig vom Zelltyp, in welchem die Kieselsäure sich ablagert, umfassen Phytolithe eine Vielzahl an morphologischen Strukturen. Basierend auf Raman- und IR-Daten einzelner Phytolithe lassen sich die verschiedenen Strukturen, verkieselte lange Zellen, Stacheln und Bilobat-Silica-Zellen, unterscheiden. Aus den Variationen innerhalb der Strukturen und Zusammensetzungen von Sorghum-Phytolithen lässt sich schlussfolgern, dass die biologischen Prozesse der Ablagerung des Siliciumdioxids sich zwischen diesen Zelltypen unterscheiden müssen. Die Pflanzengewebe und die entsprechende biologische bzw. organische Umgebung, in denen Siliciumdioxid abgelagert ist, wurden unter Verwendung eines multimodalen Ansatzes charakterisiert, welcher Fluoreszenz-, Hellfeld- und Rasterelektronenmikroskopie beinhaltet. Insbesondere wurde die chemische Zusammensetzung der Pflanzengewebe hinsichtlich der Kieselsäure-Supplementierung unter Verwendung von Raman- und FTIR-Mikrospektroskopie kartiert. Die Wirkung von Siliziumergänzung bzw. -entzug auf die Pflanze wurde für verschiedene Gewebetypen unter Verwendung der spektroskopischen Daten und multivariaten Analysen bewertet. Überdies wurde ein neuartiger Ansatz zur

Untersuchung von Pflanzengeweben, basierend auf der optischen Nahfeldmikroskopie (s-SNOM) im mittleren Infrarotbereich (IR) eingesetzt. Dadurch konnten IR-Nanospektren sowohl aus fixierten als auch erstmals aus nativen Pflanzenproben aufgenommen werden. Die Strukturen chemisch extrahierter Phytolithe wurden mit silifizierten und nicht-silifizierten Zellwänden verglichen. Die Korrelation der Nano-IR-Bilder und der aus mechanischen Phaseninformation erzeugten Bilder ermöglicht eine kombinierte Analyse von mechanischen Materialeigenschaften mit der chemischen Zusammensetzung und Struktur. Auf diese Weise können sowohl die Zellwände, als auch die Phytolithstrukturen untersucht werden. Um die Rolle der organischen Matrix zu verstehen, wurden Modellverbindungen betrachtet, die die Ablagerung von Kieselsäure in den Pflanzen induzieren können. Es wurden in-vitro-Reaktionen durchgeführt, die eine gleichzeitige Präzipitation von Lignin und Siliciumdioxid sowie eine Polymerisation zusammen mit Peptiden simulieren. Dadurch können Wechselwirkungen und eine mögliche Rolle dieser Verbindungen in der Kieselsäure-Ablagerung in der lebenden Pflanze bewertet werden. Die Ergebnisse lassen starke Wechselwirkungen zwischen diesen Verbindungen und Siliciumdioxid vermuten. Neben einem besseren Verständnis verschiedener Aspekte der Silifizierung von Pflanzen werden in dieser Arbeit völlig neue Methoden zur Charakterisierung von Pflanzenproben vorgeschlagen. Mit diesen können nicht nur die chemischen Prozesse der Silifizierung von Pflanzen, sondern auch eine Reihe anderer physiologischer Vorgänge besser untersucht und kontrolliert werden.

Schlüsselwörter:

Phytolithe, Biosilizifizierung, Raman, FTIR

Abstract

Silica deposition in plants is a common phenomenon that correlates with plant tolerance to various stresses. Plants accumulate silicon in the form of silicic acid, which is precipitated as amorphous silica in microscopic particles termed phytoliths. Deposition occurs mostly in cell walls, but its mechanism is unclear. The aim of this work is to gain a better understanding of the processes that govern silica deposition in plants using the example of sorghum leaves. With that purpose, different vibrational techniques were used to obtain information in plant tissues and molecular models, addressing different length scales.

Solid-state NMR and thermogravimetric analysis of extracted leaf phytoliths showed the dependency of the structure on the extraction methods. Phytoliths comprise a variety of morphologies according to the cell type in which the silica is deposited. Based on Raman and IR data of individual phytoliths, silicified long cells, prickles and bilobate silica cells could be discriminated. The variations in structure and composition of sorghum phytoliths suggest that the biological pathways leading to silica deposition vary between these cell types. The plant tissues where silica is deposited were characterized using a multimodal approach consisting of fluorescence, brightfield and scanning electron microscopies. In order to study the biological/organic environment where silica is deposited in the plant, the chemical composition was mapped using Raman and FTIR microspectroscopy, specifically regarding the silicon supplementation in the plant. The effect of silicon supplementation/deprivation was assessed for the tissue types using the spectroscopic data and multivariate analyses. Moreover, a new approach to study plant tissues based on scattering-type near-field optical microscopy (s-SNOM) in the mid-infrared (IR) region was used here to collect IR nanospectra from both fixed and for the first time from native plant samples. The structures of chemically extracted phytoliths were compared to silicified and nonsilicified cell walls. The correlation of the nano-IR images and the mechanical phase image enabled a combined probing of mechanical material properties together with the chemical composition and structure of both the cell walls and the phytolith structures. To study the role of the organic matrix, model compounds that could

induce silica deposition in plants were considered. *In vitro* reactions simulating lignin-silica co-precipitation and silica polymerization with peptides were performed to evaluate their interactions and the feasibility of silica deposition in the plant mediated by these compounds. The results suggest strong interactions between these compounds and silica. In addition to adding a better understanding of several aspects of plant silicification, this thesis suggests new methodologies to characterize plant samples, provides a better understanding of the chemical process that control plant silicification, and evaluates the current methods used in plant science.

Keywords:

Phytoliths, Biosilicification, Raman, FTIR

Contents

Chapter 1 Introduction **1**

Chapter 2 Research background **5**

2.1. Silicon, silica and their chemistry 5
2.2. Silicon in agriculture 6
2.3. Uptake, transport and location of silicon in plants 7
2.4. Advantages of silica deposition 8
2.5. Mechanisms of silica deposition in plants 8
2.6. Proteins that precipitate silica 9
2.7. Sorghum as silicification model 10
2.8. Phytolith extraction for further analysis 11
2.9. Microscopy of plant tissues 12
2.10. Raman and FTIR spectroscopy of complex samples 12
2.10.1. Microspectroscopy and imaging 13
2.10.2. Pre-processing and interpretation of vibrational spectra 14
2.11. Applications of vibrational spectroscopy in plant science 15
2.12. Nano IR 16

Chapter 3 Materials and methods **17**

3.1. Chemicals 17
3.2. Plant material and growing conditions 17
3.3. Sap analysis 18
3.4. Phytolith extraction 18
3.5. Thermogravimetric analysis of extracted phytoliths 19
3.6. Solid-State Nuclear Magnetic Resonance of extracted phytoliths 19
3.7. X-Ray Diffraction of extracted phytoliths 20
3.8. Raman spectroscopy of extracted phytoliths and sorghum leaves cross-sections 20
3.9. Synchrotron FTIR microspectroscopy of extracted phytoliths and tissue sections 21
3.10. Data pre-processing 22
3.11. Scanning Electron Microscopy Energy-dispersive X-ray spectroscopy (SEM-EDX) of sorghum leaf cross-sections and extracted phytoliths 23
3.12. Fluorescence images of sorghum leaf cross-sections 23
3.13. Nano IR analysis of plant samples 24

3.14. Lignin synthesis and lignin-silica coprecipitation 25
3.15. Precipitation of silica by peptides 25
Chapter 4 Sorghum biosilica location and structural characterization. 27
4.1. Location and types of phytoliths 28
4.2. Amount of silicic acid and silica in sorghum 29
4.3. Effect of the extraction method on the silica 30
4.3.1. Solid State - Magic Angle Spinning - Nuclear Magnetic Resonance (SS-MAS-NMR) of extracted silica 30
4.3.2. Thermogravimetric Analysis of extracted silica 32
4.3.3. Extracted silica is build of spherical particles 33
4.4. Vibrational spectroscopic discrimination of sorghum phytoliths . 35
4.4.1. Raman analysis 35
4.4.2. Comparison of synchrotron infrared microspectra of long cells and silica cells phytoliths 41
4.5. Conclusions 43
4.5.1. Differences between phytolith types 44
4.5.2. Potential plant biosilica formation mechanisms 45
Chapter 5 Sorghum leaf as a model for multimodal microspectroscopic analysis 47
5.1. Fluorescence images of cross-sections 50
5.2. Raman and IR spectra of sorghum leaves and band assignment .. 51
5.3. Chemical images of sorghum leaf cross-sections 55
5.3.1. Raman band imaging 56
5.3.2. FTIR band imaging 58
5.4. Multivariate imaging of Raman data of sorghum leaves 62
5.5. Tissue classification and chemical differences between tissue types 64
5.6. Evaluation of the chemical differences between tissue systems by multivariate analysis 66
5.6.1. Chemical differences between the epidermis and sclerenchyma 66
5.6.2. A high concentration of waxes is found in the epidermis and cork cells 67
5.6.3. Chemical differences between xylem, phloem, and bundle sheath 68
5.6.4. Tissue comparison by silicon treatments 70
5.7. Evaluation of the laser-induced fluorescence 72
5.7.1. Lignin autofluorescence and structure 74
5.7.2. Deconvolution of the lignin bands 75

5.7.3. Relationship between the laser induced fluorescence and the Raman spectra due to lignin bond types and structure 76
5.8. Conclusions 79
Chapter 6 Nano FTIR applied to plant tissues 83
6.1. FTIR nanospectra of isolated phytoliths 85
6.2. Reproducibility 87
6.3. Silica structure of extracted phytoliths 87
6.4. Structure and distribution of biosilica in the cell walls of wheat awns 90
6.5. FTIR nanospectra of unfixed leaf tissues 96
6.6. Conclusions 98
Chapter 7 *In vitro* silica precipitation assays 101
7.1. Coniferyl alcohol and ferulic acid polymers establish nucleation sites for silica deposition in vitro 102
7.2. Silica gel and coprecipitated silica-lignin showed spectroscopic differences 106
7.3. Silica is deposited after lignin formation 107
7.4. Peptide-silica precipitation 108
7.5. Conclusions 111
Chapter 8 Summary and outlook 113
Bibliography 117
List of abbreviations 138
List of Figures 139
List of Tables 143
List of publications 144
Acknowledgements 146
Declaration 147

Chapter 1

Introduction

The scientific interest in plant silicification goes back very long in time. Davy was the first one to study silicon in 1808 and its effect in plants in 1814. But research on plant silicification *per se* started when Crüger found silica bodies in cauto bark after acid digestion in 1857.[1] He hypothesised that silica deposition in plants occurs in dead cells. In 1861, Von Mohl, father of the cellular theory, corroborated Crüger's observations but disagreed with the hypothesis that silica deposition always occurs in dead cells.[2] He found silica filling entire cells in various plants and used hydrofluoric acid to dissolve the silica and leave the organic material. Since then, plant silicification has attracted the attention of many scientists and it is investigated in biology, geology, palaeontology and material sciences. Several thousands of articles have been published on the topic, with a renewed special interest after 1994, and especially since 2010.[3] Plant silicification is an amusing and fascinating topic. From the material science point of view, it is intersting since plants are able to deposit silica at neutral pH, low temperatures and ambient pressure with similar properties than the industrial silica currently produced at low pH, high temperature and high pressure[4] using mechanisms that still puzzle the plant scientific community.[5] In botany, the interest arises from the occurrence and role of phytoliths, the silica microscopic particles formed in several organs[6] within plants and among plant groups. Phytoliths are morphologically very diverse, each plant species presents its types, and even in the same species, many types of phytoliths have been described, especially in grasses.[7] They are very resilient and are preserved for hundreds and even thousands of years, therefore they are also extensively used in paleoenvironmental studies and examined in geology and archaeology to reconstruct ancient environments, vegetation and ecosystems.[8-14] And above all, the interest from the agricultural point of view, that arises from the beneficial effects of silicon, which are well documented.[15] The reported

benefits range from increased yields, tolerance against biotic and abiotic stresses, alleviating toxicity of heavy metals, resistance to drought and many more.[15] Yet the mechanisms are not completely understood.[3] Silicon alleviates the two major adverse climatic factors that restrain plant growth: drought and extreme temperatures. According to the current climate change models, drought and temperatures will increase in the future.[16] Understanding the role of silica on a subcellular level may allow to developing plants for better crop yields with controlled amounts of silica optimised for additional industrial applications. Biosilica potential nanotechnology usages have been reviewed recently,[17] and plant silica has already been used for the production of low-cost ultra-high performance concrete,[18] also diatom biosilica has been used as drug-delivery vehicles in biomedical research.[19] The advantage of biosilica from plants over biosilica from diatoms is the huge availability, plant silica bodies are formed in parts of plants that are not consumed, and they can easily be obtained as a by-product for many crops.

The still vast number of open questions and uncertainty surrounding plant silicification after so much research effort is a consequence of the inherent difficulty to study the plant silica and the interactions and mechanisms of deposition at the cellular level. Little is known on the biochemistry and physiology of plant biosilicification, and few and confusing data are available on the cellular conditions which lead to silicification.[5, 20] Plant biosilica has been extracted and characterized in many occasions using a variety of techniques such as Nuclear Magnetic Resonance, X-Ray Diffraction, electron microscopy, Fourier-transform infrared (FTIR) spectroscopy,[21-29] yet the true nature and chemical and molecular structure of the plant silica before extraction remains unknown. To study the interactions at the cellular level, a combination of different imaging and structure analysis tools is required.

To understand the effects of silica on plant cells, the connection between the molecular composition, the metabolic status, and the microscopic and macroscopic phenotype of a plant cell during silicon biomineralization must be made. To achieve this, the samples have to be investigated using methods that assess different length scales, ranging from the nanoscale and chemical composition to the microscopic level and heterogeneities and observation of macroscopic parameters.

This work aims to bring a better understanding of the processes that govern silica deposition in plants. This goal will be reached by addressing the following aspects: characterizing isolated silica, the organic matrix *in situ* and getting a better understanding of the interactions and feasibility of specific biomolecules to deposit silica. This thesis focusses on the study of sorghum leaves silicification by a combination of methods that meet the above named criteria. Different microscopy and vibrational methods were combined with multivariate analysis. Brightfield, fluorescence and scanning electron microscopies were used to visualize the tissues and to evaluate the silicification patterns at the cellular level. Complementary to this, vibrational spectroscopies providing complete molecular characterizations were obtained by Raman and FTIR. Moreover, high spatial resolution near field IR spectra helped to assess the chemical composition at nanometre resolution.

This thesis is organized as follows. Chapter 2 provides information on the current knowledge of plant silica and the state-of-the-art of the methods used for its study. Chapter 3 contains details on the experimental methods used to obtain the results presented in chapters 4-7. In Chapter 4, the silicification patterns in sorghum leaves are described, structural analysis and, more interestingly, analysis of individual extracted phytoliths using vibrational spectroscopy (both Raman and IR) and the differences found between morphotypes are discussed. Chapter 5 presents a multimodal approach to image the biochemical composition of the plant cell wall *in situ* in the presence and absence of silica. Thereby, the characterization of the chemical environment in which the silica is deposited is performed. Furthermore, the utility and feasibility of several multivariate methods are discussed. Chapter 6 deals with the novel application of nano FTIR spectroscopy which is based on scattering-type near-field optical microscopy (s-SNOM), to study plant samples with nanometre resolution in the context of plant silicification. Chapter 7 shows the results of *in vitro* silica precipitation assays and discusses the plausibility of cell wall components and proteins to precipitate silica under physiological conditions. Finally, the main conclusions from the results obtained in this work are summarized in Chapter 8 along with an outlook on potential future research on the topic.

Chapter 2

Research background

This chapter provides fundamental aspects needed to study plant silicification. First, a brief overview is provided on silicic acid and silica chemistry and the conditions in which it is used by the plants. This includes the current knowledge on location, mechanisms and reasons for silica deposition. Then, the state-of-the-art to study plant silicification and more general plant science are reviewed, focusing on the methods used in the experiments undertaken in this work. Mainly Raman and infrared (IR) spectroscopies and their combination with multivariate analysis.

2.1. Silicon, silica and their chemistry

Silicon (Si) is the second most abundant element in earth crust after oxygen, together they form silicate minerals which constitute more than 90% of the earth crust.[30] The soluble form of silicon and therefore the form in which silicon is available for plants is orthosilicic acid ($Si(OH)_4$). Several factors influence the amount of silicon uptaken from plants, including the pH of the soil and the content of iron and aluminium oxides.[31] Orthosilicic acid is a weakly acidic molecule (pKa 9.8) with silicon tetrahedrally coordinated to four hydroxyl groups. Even at very low concentrations (2mM), it generates oligomers and rapidly polymerizes.[30] The condensation process is spontaneous, first small oligomers are formed and these serve as nuclei for the formation of stable particles, a gel or aggregate network. The molecules condense maximizing the number of Si–O–Si bonds, with cyclic species being formed early in the condensation process. Almost all silicas contain high proportions of cyclic species unless they have been formed under conditions of extreme acidity.[32] When the concentration of orthosilicic acid decreases near the solubility limit a process known as Ostwald ripening occurs. The smaller particles dissolve, releasing silicic acid that

redeposits onto the larger particles present. At neutral pH (6.0–8.0), particles continue growing until the levels of soluble silica reach the solubility of amorphous silica. The particles are negatively charged at the surface and repel one another. When salts are present (like in a biological environment), the surface charge is reduced or cancelled, and the particles form dense 3D networks. The materials contain silanol groups at the surface. The environment and precipitation conditions in which the mineral forms make the silica to vary in solubility, density, hardness and composition.[33] The solubility of silica is dependent on its structural form and hydration level. Thus, the solubility of anhydrous non-porous amorphous, SiO_2, is 70 ppm but increases for amorphous silica consisting of small particles or porous aggregates. Most powders and gels have a solubility of 100-130 ppm. On the other hand, the solubility of crystalline silica (such as quartz) can be as low as 6ppm. Silica or silicon dioxide, (SiO_2), is an amorphous material and it is the form in which silicification occurs in the biological world and the major component of sand. Biosilica occurs in bacteria, algae, plants, and animals (invertebrates and vertebrates).

2.2. Silicon in agriculture

Silicon is ubiquitous and abundant in soils. The concentration in soils is estimated to range between 0.01 to 2.0 mM, and it is available for almost all plants. The amount of silicon present in plants varies greatly because of the differences in Si uptake. Terrestrial plants contain Si in varying amounts ranging from 0.02 to 10 % of shoot dry weight. *Equisetum hyemale*, that belongs to one of the oldest living plant families, Equisetaceae, is an extreme case of silicon accumulator and can contain up to 25-33 % of Si in its dry weight.[34] Despite its omnipresence in both soils and plants, Si is not considered an 'essential' mineral element of any terrestrial higher plant taxon, except for the members of Equisetaceae.[35] Nevertheless, the ability of silicon dioxide to reduce biotic and abiotic stresses in plants is well documented.[15] Si has a strong influence on the life of plants and the performance of crops. It enhances growth, yield and quality and provides mechanical strength; provides resistance to herbivores and to plant diseases caused by fungi, bacteria, viruses and nematodes; resistance to metal toxicity, salinity stress; drought and to extreme temperatures, promotion of photosynthesis;

resistance to ultraviolet (UV) radiation alleviation of stress from excess or deficiency of other minerals.

2.3. Uptake, transport and location of silicon in plants

The capability to accumulate Si of different plant species was attributed to the specific ability of roots to take up Si.[36] In 1990 Takahashi et al.[37] proposed the classification of higher plants according to the uptake in relation to the estimation of silicon uptake with water: active (higher Si uptake than expected with water uptake), passive (similar to the expected with water uptake), and rejective (lower than expected with water uptake). Due to the differences in silicon uptake by the roots, silicon accumulation differs greatly between plant species. Rice (*Oryza sativa*), wheat (*Triticum aestivum*), barley (*Hordeum vulgare*), maize (*Zea mays),* pumpkin (*Cucurbita moschata*) and horsetail (*Equisetum arvense*), all silicon accumulators, actively transport Si through an identified and described mechanism.[36,38] In grasses, Si uptake by roots is mediated through the cooperative action of membrane proteins, an aquaporin-like channel and a proton antiporter, encoded by the *Lsi1* and *Lsi2* genes respectively.[36] *Lsi6* encodes an influx transporter involved in xylem unloading of Si also identified in gramineous species, rice, barley and corn.[36] After transportation in the xylem promoted by evapotranspiration silicon eventually polymerizes to form hydrated silica ($SiO_2 \cdot nH_2O$) in several tissues.

The amorphous hydrated silica forms mineral structures that have various shapes and properties depending on the cell in which are formed and are called phytoliths.[6] Silica is deposited in cell walls, cell lumen, and intercellular space. The distribution and diversity of phytoliths in monocotyledons have been reported on several occasions.[5, 7, 24, 25, 39-41] In the roots of grasses (*Poaceae)*, silica is deposited in the endodermis. In the stems, leaves and inflorescence bracts, the main deposition sites are in the epidermis, and small amounts are deposited in the seed in brush hairs. Silica bodies occur in the leaf epidermis both adaxially and abaxially, and rarely in mesophyll or diaphragm cells combined of diverse cell types.[7] Cells specific for silica deposition are arranged in parallel rows on the epidermal cells of grasses. They are called silica cells or bilobate cells. Less work has been done on species other than grasses and cereals, but in general,

the leaf epidermis is the major location for most silica deposition.[6] Silica is also deposited as a thin layer beneath the cuticle layer, forming a cuticle–Si layer in leaf blades. Although silicon is mainly deposited as silica, there is some evidence indicating the presence of organosilicon in plant cell walls.[42-44]

2.4. Advantages of silica deposition

The reasons and mechanisms behind the silica phytolith formation are still unclear. The potential toxicity of silicic acid and silicification as a mechanism for its detoxification has been considered.[20] This hypothesis is supported by the fact that silicic acid is prone to polymerize in concentrations exceeding 2 mM. Therefore, random silica deposition might lead to silica scaling on the surfaces of membranes or enzymes and impair their functionality. Nevertheless, silica deposition provides many known benefits. The current consensus is that although it is not essential, it is important in the growth, strength, and management of many connective tissues. Traditionally, phytoliths have been considered as supporting structures improving the mechanical properties of plant tissues.[45, 46] The silica linked with the cell wall matrix improves the structural stability of cell walls. On a weight basis, the energetic cost of incorporating 1 g of SiO_2 is 27 times cheaper than incorporating 1 g of lignin. On a volume basis, the energetic advantage of SiO_2 is less but still amounts to some 20-fold for lignin and 10-fold for polysaccharides.[47] Nevertheless, if an organism relies on SiO_2 as a major component, depletion in its environment would be tragic. Once deposited, it creates a physical protective barrier against fungi[48] and insects.[49] The optical properties of plant silica cannot be ignored as silica reduces the amount of UV radiation entering the tissue[50] and encourages photosynthesis.[51] Deposited silica also protects against grazing animals and phytophagous insects, probably via abrasion and making their foliage indigestible.[52, 53]

2.5. Mechanisms of silica deposition in plants

Silica accumulation starts at a very young stage and continues after completion of cell expansion. The deposition is slow in winter, but rapid during spring and summer

suggesting than the accumulation pattern is the result of physiological plant activity.[54] Silica is deposited in cell walls, cell lumen, and intercellular space. Two main hypotheses have been proposed to explain silica deposition: the first, a passive form supported on the spatial correlation between silica deposition and water transpired from a specific organ, in which the cell wall components may affect the specific location of the silicification.[20] The facts supporting a passive form of silicification are the absence of any discovered silicon biochemistry and the non-essentiality of silicon in all plants and potentially toxic in some. Plant silicification has been described as a passive process that occurs simply as a consequence of biochemistry and cellular machinery which evolved to fulfil different requirements.[20] This type of silicification may be sufficient to explain the indiscriminate and continuous silicification of epidermal cells and prickles. The second hypothesis to explain silicification proposes a mechanism catalysed by biological entities such as proteins.[55, 56] Several reports support the existence of an active cellular deposition of silicon. For instance, a passive mechanism, cannot explain silicification in the bilobate silica cells. These cells do not accumulate silica after turgor loss, suggesting that a biological process may be involved in their silicification.[57] Early stages of silica accumulation of silica cells of wheat (*Triticum aestivum*) could not be detected, and complete silicification occurs in a few hours.[40] Silica deposition of silica cells of leaves of heath grass (*Sieghngia decumbens*) showed to be independent of transpiration.[58] And bilobate silica cells in sorghum (*Sorghum bicolor*) deposited silica independently of water evapotranspiration whereas the silica deposition takes place only during leaf development and in viable cells.[56] Based on all these facts, recently it has been suggested that active and passive mechanisms may be involved simultaneously.[5]

2.6. Proteins that precipitate silica

Kauss and co-workers proposed the involvement of a protein rich in lysine amino acids in the silica deposition in cucumber.[59] They concluded that the number of lysine amino acids was a determinant factor to precipitate silica. The high density of positively charged amino groups has a much bigger influence on the ability to deposit silica than the primary protein sequence. In addition, amino acids were recovered after hydrofluoric acid extraction of silicified hairs from the lemma of the grass *Phalaris*

canariensis[60] and the nitrogen/carbon ratio measured using nanoscale secondary ion mass spectrometry in wheat phytoliths is in agreement with the presence of amino acids.[61]

Very recently a previously uncharacterized protein in *Sorghum bicolor* named Siliplant1 have been presented and proposed as responsible for the silica deposition silica in sorghum silica cells.[62] This protein has seven repeat units rich in lysine, similar to diatoms silaffins[63] and several proline residues as in a proline-rich protein from cucumber.[59] It consists of 524 amino acids with random coil representing approximately 80%, α-helix 14% and no tertiary structure.[62] The peptide sequence HKKPVPPKPKPEPK is repeating in the domains. The potential of sorghum proteins to precipitate silica is further explored in Chapter 7.

Biosilicification is not exclusive of plants, diatoms and sponges also deposit silica, although the mechanisms of biomineralization in these organisms are inherently different. Silicification of diatoms and sponges has been widely studied and it is better understood than plant silicification. [4, 64-67] Diatoms use silaffins (small peptides) and long chain polyamines. Sponges use the enzyme silicatein. In both, proteins act as structural templates, and additional proteins which modulate the process are continuously discovered.[4] In diatoms, hydrofluoric acid has been used to dissolve silica and leave the proteins and then separated them by cation exchange chromatography, but not all are extractable.[4] Silaffins are repetitive peptides without tertiary structure.[63] The identified silaffins are able to precipitate silica within seconds from a solution rich in silicic acid.[63] Solution in absence of silaffins is stable but they coprecipitate with silica as long as there is silicic acid present and amount of precipitated silica is proportional to the amount of silaffins added. The process is a million times faster than the abiotic polymerization of silica.

2.7. Sorghum as silicification model

Traditionally, silicification has been studied in Equisetum, rice, maize and wheat. [36, 43, 68-75] For this dissertation, *Sorghum bicolor* was chosen as the reference model to study plant silicification and therefore the majority of the experiments are performed using

sorghum samples. Sorghum is an African grass grown for food, feed, fibre and fuel. It is related to sugar cane and maize and it is the fifth most important cereal crop in the world. It is especially important in dry regions such as northeast Africa and the southern plains of the United States due to its drought tolerance.[76] Sorghum is one of the most efficient biomass accumulators, with potential for use as cellulosic biofuel crops. The complete 730-megabase *Sorghum bicolor (L.) Moench* genome was presented in 2009.[76] In the past decade sorghum has become a very attractive research model of Saccharinae and other C4 grasses for research due to its small genome (730 Mb) and its economic importance. Many new mutants and hybrids to improve crop yields have been developed in the last years.[77] In the context of silicification, it is a perfect model as it accumulates silica in large quantities in roots and leaves.[57] A low silicon accumulating sorghum mutant was recently presented and described widening the opportunities to understand plant silicification.[57]

2.8. Phytolith extraction for further analysis

Phytoliths are commonly isolated for research purposes. The most common methods described in the literature to separate organic matter from the silica comprise dry ashing at high temperatures, wet ashing using strong acids such sulfuric or nitric acid and strong oxidants like hydrogen peroxide, microwave assisted digestion and enzymatic digestions.[24, 25, 78-80] Due to the importance of phytoliths on archaeological studies a considerable effort has been invested in development and optimise methods for the isolation and purification of phytoliths. Corbineau and co-workers reviewed the published protocols for phytolith extraction from plants used for morphological identification purposes.[81] They also proposed two optimized protocols using sorghum materials leading to pure phytoliths concentrates to perform isotopic analysis. At the molecular level, solid-state ^{29}Si Nuclear magnetic resonance (SS-NMR) allows for the observation of connectivity and degree of condensation in solid siliceous materials by comparing the intensities of the Q0, Q1, Q2, Q3 and Q4 signals,[21, 82, 83] that correspond to the number of hydroxyls bond to the silicon atom. Silica structure and bonding configuration can also be elucidated by IR and Raman spectroscopy,[84] as will be shown in Chapter 4 both can be used to characterize the silica in great detail.

2.9. Microscopy of plant tissues

To study plant biosilica in situ is challenging because the optical transparency and microscopic sizes of silica phytoliths do not allow their visualization and localization in the tissues by classical light microscopy methods. It is almost impossible to differentiate silicified cells or tissues from non-silicified cells using bright-field microscopy. To overcome these limitations several stains like silver chromate, methyl red or crystal violet lactone have been used to visualize the silica structures,[85] however they lack specificity. Silica phytolith visualization was achieved within the plant tissues by fluorescence microscopy at high pH allowing to study biomineralization at cellular.[86] Nevertheless, it is unclear if the fluorescence arises from the silica or some other colocalized organic compound. Scanning electron microscopy coupled with Energy Dispersive X-ray (EDX) has been successfully used to provide high-resolution images of the cell structures with the advantage of unambiguous identification and location of silicon.[28, 74] Environmental scanning electron microscope (ESEM) additionally presents the advantage of visualizing the silica in fresh tissues without the difficult and time-consuming traditional sample preparation required for SEM. Silica is also commonly studied by SEM and Transmission electron microscopy (TEM) to identify the sizes of fundamental particles and their interconnections.[21, 32, 87, 88] Due to the limitations to study plant biosilica *in situ*, phytoliths are commonly isolated from the organic materials of plant tissues before their morphological, physical and chemical analysis.

2.10. Raman and FTIR spectroscopy of complex samples

Most experiments and their results presented in this dissertation are based in vibrational spectroscopic methods and therefore the techniques used will be described in more detail. In general, the radiation incident on a sample can be reflected, absorbed, transmitted, or scattered. Experimentally, any of the intensity components can be used to measure the spectrum of the sample. The extent to which light is transmitted, reflected, scattered, or refracted depends on the sample morphology, crystalline state, the angle of the incident light, and the difference in refractive indices of the sample and surrounding matrix. Both Raman and Fourier transformed infrared (FTIR)

spectroscopy are vibrational spectroscopic methods, where characteristic frequencies are used for the elucidation of molecular structure.[89] They are complementary techniques, as some vibrations may both Raman and IR active. However, they are governed by different selection rules. IR spectroscopy is based on the absorption of mid-IR radiation, it directly measures transitions between molecular vibrational energy levels. This interaction depends on the electric dipole moment. The resulting spectrum represents the molecular absorption and in complex samples, it creates a molecular fingerprint of all IR active vibrations of all molecules in the sample.

Raman spectroscopy is an inelastic light scattering event. The exciting photon has much more energy than the vibrational quantum states and can be selected according to optical properties or other requirements of the sample. This enables the avoidance of fluorescence or the exploitation of resonance molecular enhancements. Raman activity involves a change in polarizability undergoing the vibration. The intensity of the Raman scattering is proportional to this polarizability change. Therefore, Raman and IR spectroscopy can provide complemental structural information.

2.10.1. Microspectroscopy and imaging

To obtain Raman and IR spectra of heterogeneous complex samples, such as a plant tissue sections both spectroscopy methods can be combined with microscopy. Microspectroscopy allows getting spatially resolved information regarding quantity, composition, structure, and distribution of chemical constituents in a tissue. IR and Raman have been very successfully coupled with a microscope permitting non-destructive, spatially resolved measurements with molecular specificity. The analytical problem dictates the choice of the microscopic technique. Sampling requirements, available diagnostic bands, spectral interferences, and spatial resolution must be carefully considered. Both techniques have applications in heterogeneous samples in industrial, forensic, and biological sciences. The spatial resolution of a microscopic method depends on the wavelength that is the laser excitation on the Raman, or the IR light used. Due to the diffraction limit, the spatial resolution of IR is not that good as the one provided by Raman microscopy. However, with the use of small apertures along with the higher brightness of a synchrotron source, high definition IR images can be obtained with an optimal pixel size of 1.1 μm.[90] Raman

microscopy has in general better resolution. The lateral resolution in typical Raman can be as low as 300 nm. Both Raman and IR spectroscopy have been used for biochemical analysis allowing characterization and imaging of biological tissues in the absence of any staining. By measurement of spectra of adjacent sample positions, a map can be obtained and images reconstructed. While the interpretation of peaks positions can help to understand the structure of the sample the analysis of the large data set requires the application of multivariate statistical analysis.

2.10.2. Pre-processing and interpretation of vibrational spectra

The pre-processing of vibrational spectra is a crucial part of the data analysis. It is performed to improve the interpretability of the spectra, and to obtain higher robustness and improve the accuracy of subsequent quantitative or classification analysis. It comprises several steps, outliers need to be excluded, the spectra must be normalized before meaningful comparison and generally also involves spike removal in the case of Raman data, interpolation and smoothing. Often, the baseline needs to be corrected, and sometimes derivatization is helpful for the interpretation or to reveal subtle features.[91] Baseline correction can be achieved by a variety of mathematical methods, including simple methods like offset correction, calculating derivatives, polynomial baseline correction, Savitzky–Golay baseline correction or Asymmetric Least Squares Smoothing (AsLS).[92] Pre-processing usually includes normalization of data, commonly done by Min-Max normalization, Standard Normal Variate or Vector normalization. Interpretation of spectra relies on peak positions and relative areas and can be achieved by inspection of individual spectra. Different approaches can be used to interpret vibrational spectra and to elucidate molecular structure and composition. Many empirical group frequencies for many molecules, organic and inorganic have been explained and refined over the past decades.[89] This has been achieved using the mathematical theoretical approaches (which also increases reliability) as well as different experiments like isotope exchange. Certain functional groups show characteristic vibrations in which only those atoms in that particular group are displaced. Since these vibrations are mechanically independent of the rest of the molecule, these group vibrations will have a characteristic frequency, which remains relatively unchanged regardless of the molecule in which is contained. But in general, the frequency of a group will also be affected by the chemical environment and the

presence of adjacent functional groups. And therefore, the vibrational spectroscopies represent a sensitive probe of the chemical interactions of complex samples. Structural interpretation is undertaken in this thesis in the structural interpretation of extracted and synthetic silica (Chapters 4 and 7). Nevertheless, to analyse the large spectroscopic data sets obtained after mapping multivariate statistical analysis tools such as Hierarchical cluster analysis (HCA) or Principal component analysis (PCA) are recommended.[93, 94] Such tools were required to understand the information contained in maps of vibrational spectra in Chapter 5.

2.11. Applications of vibrational spectroscopy in plant science

FTIR and Raman spectroscopy have been used widely used in plant science research. Both spectroscopy techniques allow obtaining spectra which present some characteristic key bands of components to determine the cell wall composition. FTIR absorption spectroscopy provides information to study cell wall constituents like proteins, aromatic phenols, cellulose, and to characterize biologically produced silica (also referred to as biogenic silica or biosilica).[95-98] Raman spectroscopy also was used to analyse cell wall polymers, silica, phenolics, and lipids in varied tissues.[74, 99-101] As early as the 1970s, vibrational spectroscopy was used to study chloroplast of green plants and algae.[102] The first plant cell wall investigations with Raman spectroscopy were carried out on wood cell walls in the mid-1980s. [103, 104] Since then it has been recurrently used in studies of wood and other lignocellulosic materials,[105-109] to understand the cell wall micromechanical properties,[110] to characterize the cell wall microfibrils containing crystalline and amorphous cellulose[111-113] and to understand the chemical composition and structure of lignins and lignin-like polymers.[103, 105, 109, 114-116]

One important consideration when choosing between FTIR and Raman is that water gives a strong absorption band in the IR (dipole) and only weak Raman scattering. The consequence is the ability of Raman to analyse plant samples in their native state but the need for fixation/dehydration for IR analysis. Therefore, IR spectroscopy is most applied to the analysis of dried or non-aqueous plant substances. Extensive research shows the ability of FTIR to classify pollen species and their quality and characterize the grains according to genetic background and environmental conditions.[117-121] Raman

is more suitable to perform in situ studies of fresh plant material because water has only weak Raman scattering properties.[122] However, the excitation wavelength used may interfere and induce fluorescence.

2.12. Nano IR

During the past two decades, several groups have shown that it is possible to collect infrared spectra in the near-field of an atomic force microscope (AFM) tip in a scattering-type near-field optical microscope (s-SNOM) that can be operated in the mid-IR to far-IR range,[123-125] even with significant enhancement.[126] This technique, IR nanospectroscopy, allows measuring IR spectra at an ultra-high spatial resolution as the effect is restricted to the near field, approximately equal to the radius of the probing tip (~20 nm),[127] far beyond the classical diffraction limit.[39, 128] The s-SNOM approach acquires simultaneously amplitude and phase images[128, 129] that give information on refractive and absorptive properties of the sample. The infrared image obtained with the s-SNOM is complemented with information on the sample topography provided by the AFM tip.[127] The lag between the driving oscillation and cantilever response through the analysed region, i.e., the AFM mechanical phase, can be used for imaging at high resolution and reflects the mechanical properties of the sample.[130] This approach and the feasibility of applying it to plant science is further discussed in Chapter 6 of this dissertation.

Chapter 3

Materials and methods

3.1. Chemicals

Hydrochloric acid (HCl, 37%) lot 5ZBF3160V, hydrogen peroxide (H_2O_2, 30%) lot SZBC3560V, potassium chlorate ($KClO_3$, ≥99%) lot R9-20/22-51/53, sodium molybdate (Na_2MoO_4, ≥98%), ethylenediaminetetraacetic acid iron(III) sodium salt powder (EDFS), ethanol, formaldehyde, acetic acid 37%, coniferyl alcohol (CoOH) (≥98%) lot MKCB2255V, ferulic acid (FA), horseradish peroxidase lot SLBR8171V, and tetramethyl orthosilicate (TMOS, ≥98%) lot 63238 were purchased from Sigma-Aldrich. Potassium hydroxide (KOH, 85%) was purchased from Frutarom. Potassium nitrate (KNO_3, ≥99%), cupric chloride dihydrate ($CuCl_2 \cdot 2H_2O$, ≥99%), potassium bromide, (KBr, spectroscopy grade) and potassium dihydrogen phosphate (KH_2PO_4, 99,9%) lot A837073708 were purchased from Merk. Zink chloride ($ZnCl_2$, ≥98%), calcium nitrate ($Ca(NO_3)_2 \cdot 4\ H_2O$), and magnesium sulphate ($MgSO_4$, ≥99%) were purchased from Riedel-de Haën. Ammonium dihydrogen phosphate ($NH_4H_2PO_4$, ≥99,9%) was purchased from Acros. Acetone (≥99,9%) was purchased from Gadot. Wheat arabinoxylan (AX), lot 40601, was purchased from Megazyme. Peptide-1 and peptide-3 were purchased from GL Biochem (Shanghai) Ltd., Shanghai, China.

3.2. Plant material and growing conditions

Plants of *Sorghum bicolor* (wild type; line BTx623) used for phytolith extraction and Si concentration measurements in sap were grown in soil pots at The Robert H. Smith Institute of Plant Sciences and Genetics greenhouse in Rehovot, Israel from September 2016 to January 2017.

Grains of similar morphology from *Sorghum bicolor* (L.) Moench (wild type; line BTx623) were selected and germinated in dark, at ambient temperature and wrapped in wet paper. Seedlings were grown in hydroponic media containing only Hoagland nutrient solution (KNO_3 0.5 mM, $Ca(NO_3)_2 \cdot 4H_2O$ 0.15 mM, $NH_4H_2PO_4$ 0.1 mM, $MgSO_4 \cdot 7H_2O$ 0.1 mM, $CuSO_4 \cdot H2O$ 0.03 μM, $Na_2MoO_4 \cdot 2H_2O$ 0.06 μM, $ZnSO_4 \cdot 7H_2O$ 0.16 μM, $MnCl_2 \cdot 4H_2O$ 0.91 μM, H_3BO_3 4.63 μM, EDFS ($C_{10}H_{12}N_2NaFeO_8$ 2μM) prepared with in-house Mili-Q (Millipore) water (-Si treatment), or Hoagland solution containing sodium silicate ($NaSiO_4$) at a final concentration of 2 mmol/L. These plants were used for the experiments described in Chapters 5 and 6 plants, they were grown under 18 hours/day artificial light at the chemistry department of the Humboldt-Universität zu Berlin. The hydroponic solutions were changed regularly every 3-4 days, and the pH was adjusted to 5.8. Aeration to the roots was provided by an air pump (200 l/hour). Up to 4 plants were grown in the same 2 litter pot for up to 185 days.

3.3. Sap analysis

Freshly flowing sorghum sap was collected after incision in mature plants grown in soil. 25 μl of sap aliquots were taken from 3 different visible healthy plants and diluted in 10 ml HNO_3 (1%) and sent for ICP analysis to the Interdepartmental Equipment Facility (ZBM) Analytical Lab, The Faculty of Agriculture, Food and Environmental Quality Sciences, The Hebrew University of Jerusalem, Israel.

3.4. Phytolith extraction

Leaf pieces and cross-sections were prepared manually using razor blades. Phytoliths were isolated from mature healthy leaves using two extraction methods: (a) $H_2SO_4/H_2O_2/HNO_3$ extraction (SONE) described in detail and referred as protocol 2,[81] which includes rinsing leave cut samples with 10 % HCl, then immersing the samples in a solution of 70 % H_2SO_4 at 70°C for 2 hours, and leaving overnight at room temperature, followed by heating the solution to 70°C and adding H_2O_2 at 30 % concentration until the supernatant became clear, and keeping it under heat for three

more hours. This was followed by rinsing with water 3 times, reheating to 70 °C and addition of concentrated HNO_3 and $KClO_3$. After an overnight incubation without heating, the samples were rinsed again with water and washed with 0.001 M KOH solution and rinsed 3 times with water. Afterwards, the samples were dried in an oven at 70 °C until their weight remained constant; (b) Microwave-assisted digestion (MAD) performed by Vasily Rosen at the Interdepartmental Equipment Facility (ZBM) Analytical Lab, The Faculty of Agriculture, Food and Environmental Quality Sciences, The Hebrew University of Jerusalem, Israel. The extraction was performed using a Discover SPD-80 sample digestion system (CEM, USA). The samples were pre-digested for 30 min at room temperature with 65 % HNO_3 in quartz vessels, afterwards, the temperature was raised linearly to 200 °C in 5 min and retained for 5 min more at a pressure of 200 psi. After that, samples were rinsed three times with water and dried at 70 °C. Phytolith samples for both extraction methods were stored in paraffine sealed Eppendorf tubes at ambient temperature.

3.5. Thermogravimetric analysis of extracted phytoliths

Thermogravimetric analysis (TGA) of the phytolith samples were performed with a Bargal Q500 instrument (Bargal Analytical Instruments Ltd, Israel). Approximately 5 mg of phytoliths were placed in a platinum crucible, equilibrated at 25°C and the weight variation recorded in the range of 30 to 900° C using the high-resolution sensitivity mode and a ramp of 30°C per min. Data were processed using the Universal Analysis 2000 software from TA instruments (Waters).

3.6. Solid-State Nuclear Magnetic Resonance of extracted phytoliths

Solid-state nuclear magnetic resonance (SS-NMR) experiments were performed by Nurit Filiba and Gil Goobes at the Department of Chemistry, Bar Ilan University, Ramat Gan, Israel. The measurements were performed under Magic Angle Spinning (MAS). Approximately 40 mg of extracted phytoliths were placed in the NMR rotor and the samples were spun at 10 kHz in all experiments. Spectra of ^{29}Si Direct-polarization (DP) MAS SSNMR and cross-polarization (CP) MAS SSNMR were

acquired at room temperature on a Bruker 11.7T Advance III spectrometer equipped with a 4-mm VTN CPMAS probe employing decoupling at a field of 85.7 kHz. The ^{1}H-29Si cross-polarization spectra were recorded using a CP contact time of 6 ms, recycle delay of 6 s and 2048 scans. The ^{29}Si direct polarization spectra were taken with a 3 μs 90° pulse followed by the acquisition of 2,048 points with 8 μs dwell time a recycle delay of 60 s and 137 scans. Time domain signals (2,048 points) were zero filled to 4,096 points and multiplied by exponential decaying function (with line broadening of 100 Hz) and then Fourier transformed, phase adjusted, and baseline corrected using automatic 5th order polynomial function. Line deconvolutions in all ^{29}Si NMR spectra shown were performed using the DMFIT program which minimizes the line shape generated by a set of simulated lines to the line shape of the convoluted spectrum.

3.7. X-Ray Diffraction of extracted phytoliths

High resolution X-Ray diffraction (XRD) measurements were performed by Hannes Kulla, Bundesanstalt für Materialforschung und prüfung (BAM), Berlin at the MS Beamline at Paul Scherrer Institute (PSI, Switzerland). 5 mg of each sample of phytoliths were packed in a capillary and analysed using synchrotron radiation with acquisition time 30 seconds and wavelength 0.7085238 Å using the Si standard SRM640d from NIST (and LaB6) to determine the sample-detector-distance. The focused spot size was 130 μm x 40 μm and flux at 10 keV of 2.5 x 10^{13} photons/sec with a current of 0.4 A.

3.8. Raman spectroscopy of extracted phytoliths and sorghum leaves cross-sections

For Raman spectroscopic analysis extracted phytoliths were placed directly in a CaF_2 window. Raman spectra of extracted phytoliths were collected with an NRS-4500 Dispersive Raman Spectrometer (Jasco) equipped with a 100x magnification objective. Raman spectra for each phytolith were collected using a laser of 532 nm wavelength at a laser power of 5.6 mW, which was focused on a spot diameter of 720 nm corresponding to an intensity of ~1.37 x 10^{6} W/cm^{2}. Spectra were detected with a spectrometer with a grating of 300 lines/mm with an air-cooled Peltier CCD detector.

Each phytolith spectrum was obtained with 30 s acquisition time and 10 accumulations in the spectral range 136 – 3977 cm^{-1}. The spectra were frequency calibrated using a spectrum of 4-acetamidophenol. They were pre-processed with MATLAB, the procedure included background correction using asymmetric least squares method (AsLS), spectra interpolation yielding a spectral resolution of 1.8 cm^{-1}, vector normalisation and selection of the spectral range of interest before principal component analysis (PCA). PCA was also performed with the first and second derivatives of the spectra.

Raman maps were collected from cross-sections of sorghum leaves manually cut placed between two CaF_2 windows for spectroscopy with a drop of water to prevent damage from the Raman laser and decrease fluorescence. The disks were sealed with paraffin to prevent water evaporation. Raman maps were acquired with a Horiba Lab Raman microspectrometer using a green laser as excitation source (532 nm) wavelength with a power of 8.5 mW, which was focussed on a theoretical spot diameter of 1.3 μm corresponding to an intensity of ~1.6 x 10^5 W/cm^2. Spectra were detected with a spectrometer with a grating of 300 lines/mm with a liquid nitrogen cooled CCD detector. Spectra were recorded with a step size of 1 μm, 2 sec acquisition time and 22 accumulations in the range 200 to 4000 cm^{-1}. A total of 12 maps of Si supplemented samples and 5 maps of Si starved were recorded. They were pre-processed with MATLAB, the procedure included background correction using AsLS, spectra interpolation yielding a spectral resolution of 1.8 cm^{-1}, vector normalization and selection of the spectral range of interest before PCA.

3.9. Synchrotron FTIR microspectroscopy of extracted phytoliths and tissue sections

Extracted phytoliths were placed directly on zinc selenide slides and their infrared (IR) transmission spectra were collected using a Fourier transformed infrared (FTIR) microscope (ThermoNicolet) at the IRIS beamline of BESSY-HZB, Berlin. The size of the microscope aperture, determining the spot size from which the spectrum is acquired, approximately 60 μm^2 (12 x 5 μm) was adapted to each phytolith to avoid contributions by Mie scattering and maximize the signal-to-noise ratio. Spectra were

taken with 128 accumulations in the range 700-4000 cm^{-1}. 35 FTIR spectra of bilobate silica cells and 36 FTIR spectra of silicified long cells were acquired. IR spectra of prickles were also measured; however, the conical shape of the prickles caused strong scattering effects and were excluded from the analysis. For the analysis of the IR spectra of phytoliths, pre-processing of the spectra included the selection of the spectral range of interest, baseline correction with AsLS, and vector normalization. Additionally, extended multiplicative signal correction (EMSC) was applied to the data to correct baseline variations, noise, and scattering effects caused by the size of the samples in the micron range. The window size and polynomial order of the fitting curve for the Savitzky–Golay numerical algorithm and EMSC were optimized following a procedure previously evaluated and described.[121] 9 detected spectra outliers during the EMSC were removed from the analysis.

For the FTIR maps of tissue sections, samples were collected from sorghum leaves, cut into pieces, fixed with FAA (formaldehyde, acetic acid and ethanol), dehydrated with an ethanol series (50, 60, 70, 80, 90 and 100% ethanol, 100 % isopropanol) and embedded in paraffin. The paraffin blocks were cut at 20 μm thick and mounted in zinc selenide windows for spectroscopy. Then, they were deparaffinized with hexane for 30 min.

IR transmission spectra were collected using an FTIR microscope (ThermoNicolet) at the IRIS beamline of BESSY-HZB, Berlin. The size of the microscope aperture, determining the spot size from which the spectrum is acquired, was set to 12x12 μm. Spectra were taken with 64 accumulations in the range 700-4000 cm^{-1}. The step size varied depending on the sample between 3 and 5 μm. A total of 9 maps of Si supplemented samples and 9 maps of Si starved were recorded.

3.10. Data pre-processing

The Raman spectra were pre-processed using MatLab (The MathWorks, Inc., Ismaning, Germany) and CytoSpec (CytoSpec, Inc., Berlin, Germany). Data pre-processing included the elimination of spikes, interpolation, smoothed based on the Savitzky-Golay algorithm, background correction using AsLS, vector-normalization,

and calculation of first and second derivatives. For chemical mapping, intensities were determined from the original spectra after baseline correction. The principal component analysis was carried out with vector-normalized spectra and first derivatives.

3.11. Scanning Electron Microscopy Energy-dispersive X-ray spectroscopy (SEM-EDX) of sorghum leaf cross-sections and extracted phytoliths

Leaves were dissected mechanically in segments; epidermis sections and cross-sections were prepared manually using razor blades. Plant tissues observations were performed with a JCM-6000PLUS NeoScope scanning electron microscope (JEOL, Japan) with accelerating voltage 15 kV using the low vacuum mode. The silicon elemental maps of the observed samples were obtained with the same instrument by energy-dispersive X-ray analysis. Si elemental maps were obtained by EDX with a dwell time of 2 ms, high probe current, and gain 1.

The scanning electron micrographs from phytoliths were obtained by Ines Feldman (Bundesanstalt für Materialforschung und -prüfung (BAM), Berlin, with an FEI/Philips XL-30 field emission with accelerating voltage 15 kV, after placing the samples in carbon tape and coating with layers of 5 and 10 nm of gold.

3.12. Fluorescence images of sorghum leaf cross-sections

Autofluorescence microscopy images were obtained after mounting the samples in calcium fluoride windows for the Raman maps or zinc selenide windows for the FTIR maps with a light microscope Olympus BX23, Hamburg, Germany, with 20x objective. The red autofluorescence images were recorded with excitation with a wavelength in the range 530-550 nm and a cut off filter at 575 nm. The blue autofluorescence images were recorded with excitation with a wavelength in the range 330-385 nm and a cut off filter at 420 nm. All images were taken using CellSens Standard Software 1.17 (Olympus, Hamburg, Germany).

3.13. Nano IR analysis of plant samples

Three types of plant samples were evaluated by FTIR nanospectroscopy: i) extracted silica phytoliths, ii) epoxy resin embedded awns of wheat and iii) fresh untreated cross-sections of *Sorghum bicolor* leaves. The extracted sorghum phytoliths were directly placed on a silicon wafer for spectroscopic experiments. The awns of domesticated durum wheat were embedded in propylene oxide in Epon (SPI-Pon™ 812 Epoxy Embedding Kit, SPI-CHEM, hard mixture) as reported by Peleg et al.[48] Fresh cross-sections of *Sorghum bicolor* wild type plants were manually cut with a razor blade without previous embedding and placed directly on a silicon wafer.

The selected samples were analysed with a commercial nano-FTIR setup (NeaSNOM, neaspec GmbH, Munich, Germany) comprising an Atomic force microscope (AFM) equipped with a 20 nm tip, a fibre-based, broadband mid-IR pulsed laser source using a difference frequency generator (Toptica Photonics AG, Gräfelfing, Germany) and an asymmetric Michelson interferometer. The broadband mid-infrared source was set to cover the frequency range 800–1800 cm^{-1}. Selected regions were mapped, and analysed. Nano-IR spectra were measured from regions of interest. In total, 3 regions were analysed from extracted phytoliths, 13 areas from embedded awns and 3 additional areas were examined from fresh sorghum leave tissues. The sample topography, mechanical amplitude, mechanical phase and IR reflection of the samples were recorded simultaneously using the tapping mode of the s-SNOM. The tapping amplitude was set to 80 nm. AFM tip oscillating vertically at frequency Ω~ 210 kHz was employed as near-field probe. The IR amplitude and phase spectra were measured at selected locations using intermittent contact mode for optical background suppression. The tip-scattered signal was demodulated at higher harmonics nΩ of the cantilever oscillation frequency, yielding near-field amplitude and phase signals. Spectra were obtained by averaging of 10 interferograms per spectrum at a spectral resolution of 13 cm^{-1} for the unembedded samples and 10 cm^{-1} for the resin embedded samples, normalized to a background scan acquired on the Silicon wafer substrate. A zero-fill factor of 4 was used so that the final spectra were saved at a nominal spectral resolution of 3.2. cm^{-1} for unembedded and 2.5 cm^{-1} for the resin embedded samples. The spectra shown are not normalized or further pre-processed.

3.14. Lignin synthesis and lignin-silica coprecipitation

Lignin synthesis was performed according to a protocol provided by Itan Preis, Robert H. Smith Faculty of Agriculture, Food and Environment, Hebrew University of Jerusalem, (personal communication). Oxidative coupling was carried out in several different substrate conditions: (i) (CoOH) alone, (ii) a 10/90 mixture of FA/CoOH (iii) a 50/50 mixture of FA/CoOH, (iv) a 10/90 mixture of AX/CoOH and (v) a 10/10/80 mixture of AX/FA/CoOH in the presence of horseradish peroxidase. The influence of the presence of silicic acid in the reaction media was also tested.

3 mg of substrate were dissolved in 100 μl acetone and then was added to phosphate buffer (3.7 mL, 0.1 M, pH 7.4), containing horseradish peroxidase (20 units, 20 μl) and hydrogen peroxide (30% solution, 4 μl). The solution was stirred, at room temperature, in the dark. Two time points for ending the reaction were tested 3 hours and 18 hours. Silica formation was evaluated by adding silicic acid in a concentration ranging from 5 to 90 mM. Silicic acid 1 M stock solution was obtained by adding TMOS 150 μl to 850 μl of HCl 1 mM and stirred for 5 min. The resulting suspension was then thoroughly washed with distilled water and centrifuge. The insoluble polymer was finally suspended in distilled water and dry, turning in to an amorphous powder. The products were weighed, placed in a CaF_2 slide and their Raman spectra were taken using an In Via spectrophotometer (Renishaw) at 532 nm and a Horiba Lab Raman instrument at 633 nm.

KBr pellets were prepared with 2% in mass of the obtained products and analysed using a Nicolet 6700 FTIR spectrometer, in the range 400-4000 cm^{-1} collecting 40 scans.

3.15. Precipitation of silica by peptides

Precipitation experiments were conducted with Nurit Filiba and Santosh Kumar at the Department of Chemistry, Bar Ilan University, Ramat Gan, Israel and Robert H. Smith Faculty of Agriculture, Food and Environment, Hebrew University of Jerusalem. They consisted in dissolving the 2 mg of peptide in 1ml of 0.1 M potassium phosphate buffer, pH 7.0, adding 63 μl of silicic acid stock solution (final concentration 60 mM) and

incubating for 30 min under gentle shaking. Silicic acid 1 M stock solution was obtained by adding TMOS 150 μl to 850 μl of HCl 1 mM and stirred for 5 min. Sediment was collected by centrifugation at 14000 g for 5 min. The supernatant was collected, and the pellet was washed three times with deionized water. For all the peptide–silica precipitation experiments, the same reactions lacking any peptide served as control. The precipitates were left to dry under ambient conditions.

Chapter 4

Sorghum biosilica location and structural characterization

This chapter is partially based on the publication *Frontiers in Plant Science* 2019, 10 (1571).

Silica deposition occurs in all tissues, including the roots, stems, leaves, inflorescences and seeds, but it is concentrated in certain organs and tissues. Phytoliths present very diverse morphologies between plant species but also in the same plant. Classification of phytoliths according to their morphology has been proposed.[131] According to the type of silicification, two main types of phytoliths exist, the cell wall types which are formed on a carbohydrate matrix, and the cell lumen types.[132] Differences in the chemical composition according to the type of phytoliths have been hypothesized, but not confirmed.[11] In order to study phytoliths, the plant tissue around them is digested, often by harsh chemistry, high temperature, or mild chemistry during very long time periods (including archaeologic or geologic).[6] These processes change the physical and chemical properties of phytoliths. [24, 133] Such processes were evaluated on several occasions showing that they are dependent on the phytolith morphotype.[134] Individual phytoliths were also characterized [10, 61, 88, 133, 135] and even variation in the silica structure was described within one phytolith type.[136] However, different phytolith morphotypes in the same plant have not been compared.

Raman and Fourier transformed infrared (FTIR) microspectroscopy enable the probing of individual phytoliths and assessing their mineral structure and occluded organic matter. These vibrational microspectroscopy methods provide information on chemical bonds and thereby on the structure and composition of a sample. By combining a microscope with FTIR or Raman spectrometer the spectra are collected at a micrometre resolution allowing single phytolith vibrational characterization.

In this chapter, the characterization of phytoliths found in sorghum leaves is presented. The location and distribution of silicified microstructures were observed using SEM-EDX. The phytoliths were extracted by two methods: sulphuric acid-hydrogen peroxide-nitric acid extraction (SONE)[81] and Microwave assisted digestion (MAD). After extraction, they were chemically characterized by Thermogravimetric analysis (TGA), X-ray diffraction (XRD), and Solid-state nuclear magnetic resonance (SS-NMR) spectroscopy as bulk samples and the effect of the digestion methods compared. Phytolith structure was characterized by SEM and individual phytoliths were analysed by vibrational microspectroscopy, using both Raman and FTIR. The influence of the extraction method on the silica structure and condensation and the composition of occluded organic matter in the phytoliths is discussed. As it will be shown different vibrational spectra were obtained from different phytolith morphotypes.

4.1. Location and types of phytoliths

Visualization of sorghum leaf epidermis revealed several types of phytoliths (Figure 4.1). Heavily silicified bilobate silica cells, also called dumbbell cells, intercalated by non-silicified cork cells form parallel rows along the veins (red arrows in Figure 4.1A); silicified long cells cover the whole epidermis; prickles appeared in the leaf borders and across the leaf surface (blue arrows in Figure 4.1A), and cross cells were randomly distributed between the long cells (black arrows in Figure 4.1A). These observations are consistent with the silica distribution in grasses reported previously.[7, 40] The SEM-EDX images of transverse cross-sections (Figures 4.1C-4.1F) showed silica deposition mainly in the outer tissues, comprising a thin layer of silica plant covering the epidermis under the cuticle that corresponds to silicified long cells, the existence of other silica accumulations like the heavily silicified of silica cells (red arrow Figure 4.1D) and other small agglomerations.

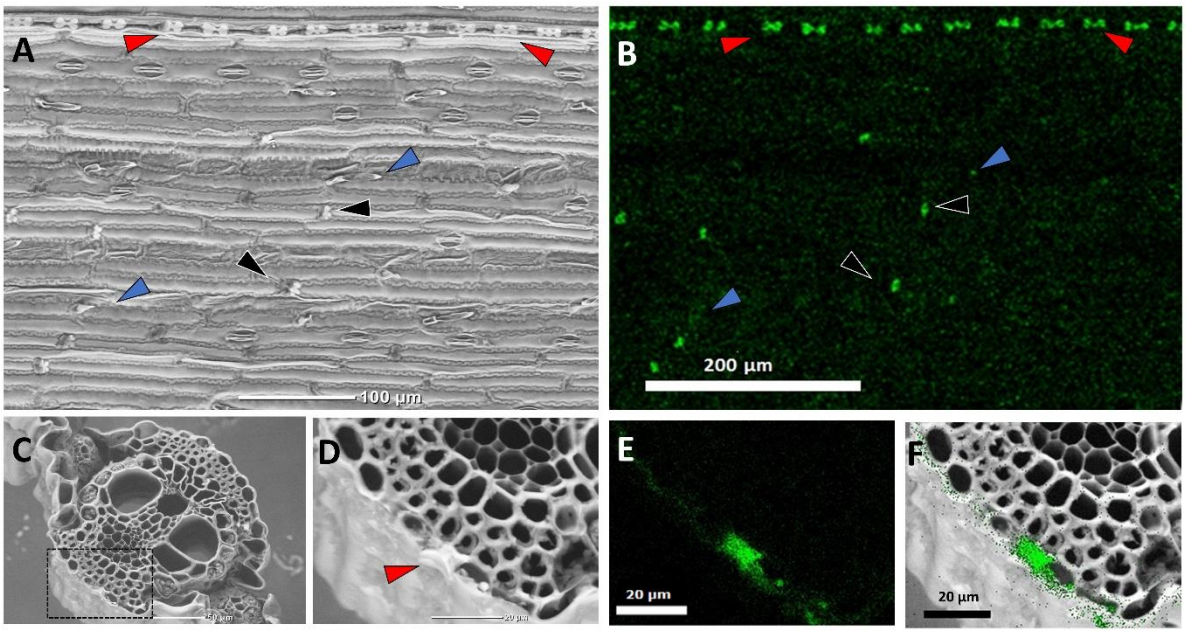

Figure 4.1: Scanning electron micrographs of sorghum leaves demonstrating typical silica deposition. (A) Epidermal surface showing a row of bilobate silica cells (red arrows), cross cells (black arrows) randomly distributed between epidermal long cells and prickles (blue arrows). (B) Si EDX map of the same region with silica accumulations visible in green. The bilobate cells and cross cells are heavily silicified and clearly visible, in contrast to the prickles where silica accumulates at the tips. (C) Leaf cross-section. The dashed rectangle is enlarged in panel D. (D) A bilobate cell cut transversally (arrow). (E) Si EDX map of the region in panel D, showing the silicon distribution in green. (F) Overlay of panels D and E. The bilobate cell volume is silicified, while in other epidermis cells only the cell wall accumulated silica. Figure reprinted with permission from Zancajo, V. M. R. et al. *Front. Plant Sci.* 10, (2019).

4.2. Amount of silicic acid and silica in sorghum

To determine the physiological conditions in which silica is deposited within the plant, the concentration of silicic acid in sorghum sap was measured using Inductively coupled plasma mass spectrometry (ICP-MS). The concentration of silicic acid in sap was 7 mMol measured just after incision but increased to 11.5 mMol collected 4 hours after incision, significantly higher (t-test, $p<0.01$) (Table 4.1). These values are in agreement with previous measures of silicic acid concentration in grass sap.[69, 137, 138] The

observed concentration is significantly higher than the solubility limit (2 mMol), above which it undergoes a spontaneous auto condensation. Nevertheless, this process is affected by pH, pressure, temperature, salts and other small molecules concentrations.[30, 139] The increase in concentration is probably a response to a traumatic event or injury (in this case section the whole plant) as silicon is involved in molecular, physical and biochemical defence mechanisms.[140]

Table 4.1: Average of silicic acid concentration and standard deviation measured in duplicate from three sorghum plants in sap just after incision and after 4 hours. The amount of silicic acid after 4 hours is significantly higher (t-test, $p<0.01$).

Time /hours	[Si] /mMol	Std
0	7	2.5
4	11.5	3.2

Plant biosilica was extracted by sulfuric acid digestion (SONE) and microwave assisted digestion (MAD). The amount of silica in sorghum leaves was estimated from the yield of the MAD extraction. According to the yield of the silica extraction, the amount of silica in sorghum leaves was 3 % of dry weight in mature leaves, slightly lower value to the 3.7 % of dry weight estimated after charring.[57]

4.3. Effect of the extraction method on the silica

4.3.1. Solid State - Magic Angle Spinning - Nuclear Magnetic Resonance (SS-MAS-NMR) of extracted silica

^{29}Si NMR provides quantitative spectra that relate the connectivity and degree of condensation of solid siliceous materials. Cross-polarization magic angle spinning (CP-MAS) ^{29}Si NMR enhances the signal intensity of Si nuclei near to the hydrogen atom because of polarization transfer from ^{1}H via heteronuclear dipolar couplings. ^{29}Si polarization spectra detected silicon atoms attached to oxygen atoms that were coordinated either to a different silicon atom or hydrogen, forming terminal hydroxyls (Figure 4.2). All silicon atoms detected were covalently bound to oxygen atoms.

Species of O_3-Si(OH) (termed Q^3) at a chemical shift of -101.6 ppm and O_4-Si (Q^4) at -111.3 ppm were detected in phytoliths from both extraction methods. Whereas Q^2 species (O_2-Si$(OH)_2$), shifted to -91.8 ppm, were found only in the MAD extracted phytoliths. The bulk (Q4) to surface (Q3+Q2) ratio was 2.9 in the MAD extraction method and 5.2 in the SONE method.

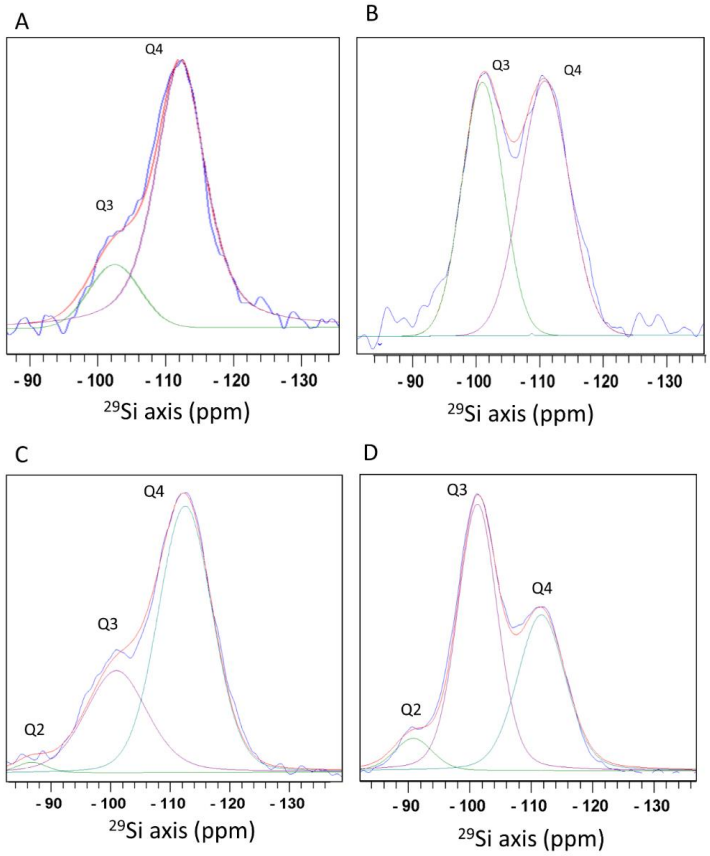

Figure 4.2: Solid State Magic Angle Spinning Nuclear Magnetic Resonance (SS-MAS-NMR) of ^{29}Si atoms in leaf silica extracted by SONE and MAD. Measurements of ^{29}Si direct polarization spectrum (blue) (A), and ^{1}H-^{29}Si cross-polarization spectrum (blue) (B) of silica extracted by SONE method. ^{29}Si direct polarization spectrum (blue) (C), and ^{1}H-^{29}Si cross-polarization spectrum (blue) (D) of silica extracted by MAD method. Spectral decomposition into 3 lines, Q_2 (green), Q_3 (purple) and Q_4 (cyan) is shown with the total simulated spectrum (red). Q_2 corresponds to a silicon atom bound to two hydroxyl groups, Q_3 to 1 hydroxyl group, and Q_4 to silicon surrounded by oxygen bridging atoms with no hydroxyl groups. Figure reprinted with permission from Zancajo, V. M. R. et al. *Front. Plant Sci.* 10, (2019).

The ^{1}H-^{29}Si cross-polarization spectrum obtained after selectively excite surface Si showed that in the SONE method the siloxane (Q_4) to silanol (Q_3) ratio is 1.2 at the surface. The MAD extracted phytoliths showed the typical silicon surface species intensity ratios of 6:55:39 for Q_2:Q_3:Q_4. The siloxane to silanol ratio on the surface was 0.6, calculated as Q_4 to (Q_3+Q_2). The higher ratio in the SONE extraction indicates a more hydrophobic surface than the MAD extracted phytoliths surface.

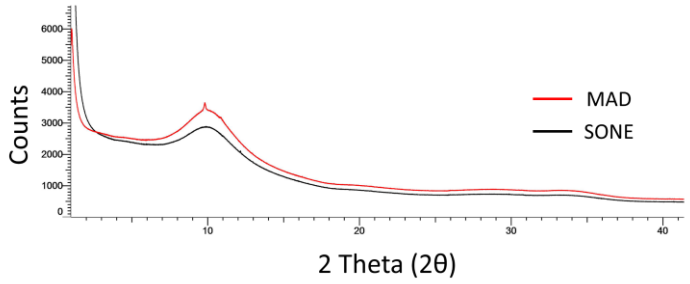

Figure 4.3: Diffractogram of sorghum phytoliths extracted by MAD in red, and SONE in black. The diffuse maximum at 2 θ=10° is characteristic of amorphous silica.

The diffraction pattern of phytoliths extracted by both digestion methods shows a diffuse maximum at 2 θ=10° and indicates an amorphous material, typical of biogenic opal (Figure 4.3). This pattern is consistent with previous reports of XRD data of plant biosilica.[27, 141]

4.3.2. Thermogravimetric Analysis of extracted silica

The thermogravimetric analysis allows monitoring the changes in the mass of a sample as a function of temperature. The change can be used to determine component percentages and determining the OH surface density and carbon content of silica.[142] During pyrolysis, the silica extracted by SONE lost about 17 % of its weight, while the silica extracted by MAD lost only about 12 % (Figure 4.4). The weight loss corresponds to bound water (up to 150°C) and organic matter (150-800°C). The peak in the differential thermal gravimetric (DTG) at 120°C (Figure 4.4) is associated to bound water, it represents a loss of 3.8 % of the weight of SONE and 4.9 % weight of the MAD silica. The TGA is consistent with the NMR analysis, showing a more hydrophilic character of the silica extracted by microwave digestion. The DTG broad peaks at 250°C, 380°C, 450°C and 700°C appear only in the SONE silica (Figure 4.4). The lack of

peaks in the DTG of the MAD extracted phytoliths indicates that much less organic matter remained after this extraction. The continuous weight loss between 150°C to 800°C in both extraction methods represents the changing of the surface chemistry from silanol to siloxane groups, as the OH groups in the surface of silica powders are removed.[142]

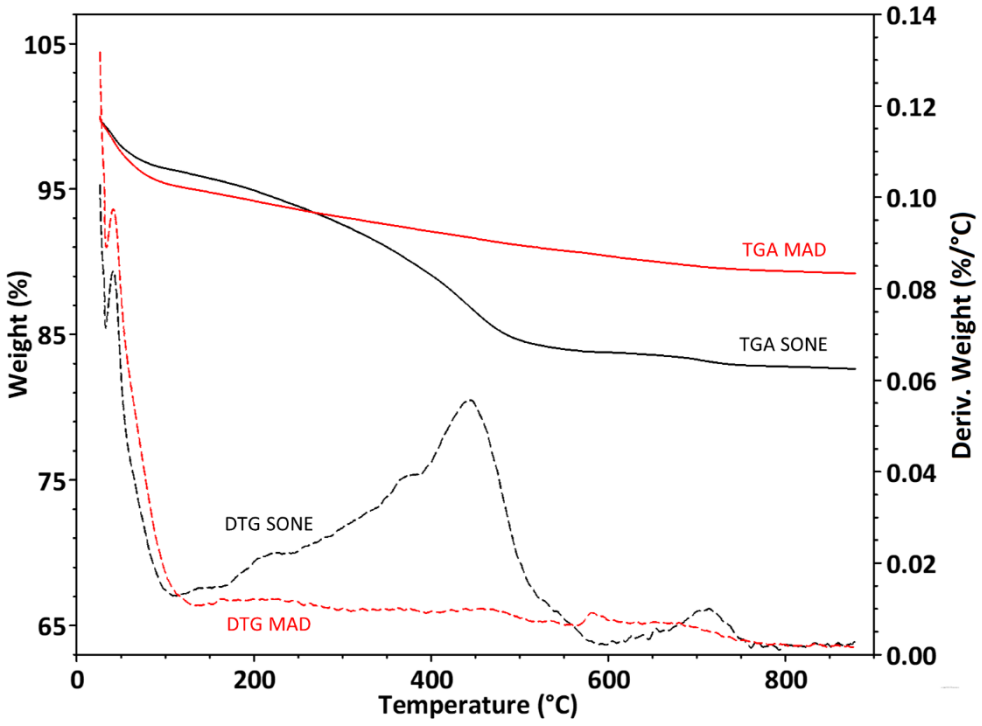

Figure 4.4: Thermogravimetric analyses of extracted phytoliths. Curves of per cent weight loss (full line, left Y-axis) and derivative of weight loss by temperature (dashed line, right Y-axis) of the microwaved-assisted digestion (MAD) (red) and sulphuric acid-hydrogen peroxide-nitric acid extraction (SONE) (black) samples. Figure reprinted with permission from Zancajo, V. M. R. et al. *Front. Plant Sci*. 10, (2019).

4.3.3. Extracted silica is build of spherical particles

Isolated phytoliths were visualized by scanning electron microscopy (SEM) which allowed identifying long cells, bilobate silica cells and prickles (Figure 4.5) as the most abundant types of phytoliths. High magnification scans revealed spherical silica particles forming all phytolith types. The silica particles appeared loosely aggregated in long cells, in comparison to densely packed particles in bilobate and cross-shaped cells. Long cell phytoliths were formed by silica spheres of 100-150 nm of diameter

when the phytoliths were extracted by wet digestion (Figure 4.5F), and 50-100 nm in the microwave extracted phytoliths (Figure 4.5J).

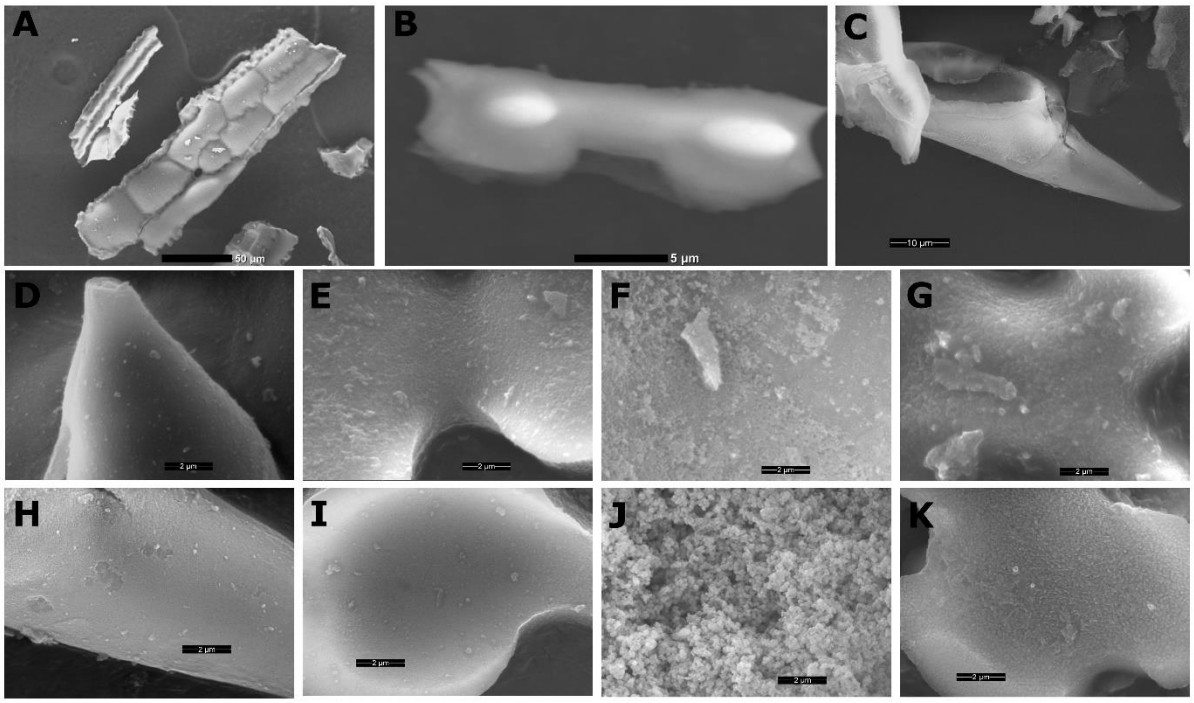

Figure 4.5: Scanning electron micrographs of silicified cells extracted by wet or microwave digestion. Low magnification (panels A-C), did not reveal differences between the extractions. (A) Long cells creating a silica skeleton imaged without gold coating, scale bar 50 μm. (B) Lateral view of uncoated bilobate silica cell showing asymmetric shape, scale bar 5 μm. (C) Lateral view of a prickle, scale bar 10 μm. High magnification scans of phytoliths extracted by wet ashing, showing the silica particles in a prickle (D), bilobate silica cell (E), long cell (F) and a cross cell (G). High magnification scans of phytoliths extracted by microwave digestion showing the silica particles in a prickle (H), bilobate silica cell (I), long cell (J), and a cross cell (K). The scale bars in panels C-K are 2 μm. Figure reprinted with permission from Zancajo, V. M. R. et al. *Front. Plant Sci*. 10, (2019).

4.4. Vibrational spectroscopic discrimination of sorghum phytoliths

4.4.1. Raman analysis

The Raman spectra of prickles, long cells and bilobate silica cells were very similar (Figure 4.6). All the observed Raman bands, assignment to the specific vibrations and molecules are summarised in Table 4.2. Due to the non-crystalline and non-uniform molecular structure of the silica, Raman signals appeared as very broad bands. The band extending from 400 to 500 cm^{-1} with a maximum at 478 cm^{-1} (Si-O-Si bending modes) corresponds to the presence of five, six and seven membered SiO ring.[143, 144]

Characteristic Raman silica bands also appeared at 808 cm^{-1} (Si-O-Si symmetric stretching), 970 cm^{-1} (Si-OH stretching mode of non-bridging oxygen atoms) and 1070 cm^{-1} (Si-O-Si asymmetric bond stretching).[143, 144] All other present bands in the spectra correspond to organic matter occluded within the silica: C-C twisting and rocking at 1153 cm^{-1}; CH_2 deformation in alkane long chains at 1298 cm^{-1} and CH_2 deformation vibrations in n alkanes at 1440 cm^{-1}. The small band at 1613 cm^{-1} corresponds to the C=C stretching or aryl stretching vibrations,[89] and most probably arises from the presence of lignin. The band at 1665 cm^{-1} appeared only in the Raman spectra of prickles (Figure 4.6, blue spectrum). It can be assigned to the C=C stretching, C=O stretching and Amide I vibrations.[89] In contrast the band at 1043 cm^{-1} was not observed in prickles spectra but was present at the variable intensity in the spectra of other phytoliths (Figure 4.6). It can be assigned to ring vibrations of substituted benzenes and C-C stretches in n-alkanes.[89] Small features at around 1550 cm^{-1} were also identified in the spectra of all phytoliths assigned to Amide II band of proteins.[89, 145] Ratios of band areas calculated in spectra of bilobate cells were significantly higher ($p < 0.05$) than prickles and long cells extracted under MAD (Figure 4.6 C) and sulphuric acid-hydrogen peroxide-nitric acid extraction (SONE) (Figure 4.6 D) methods.

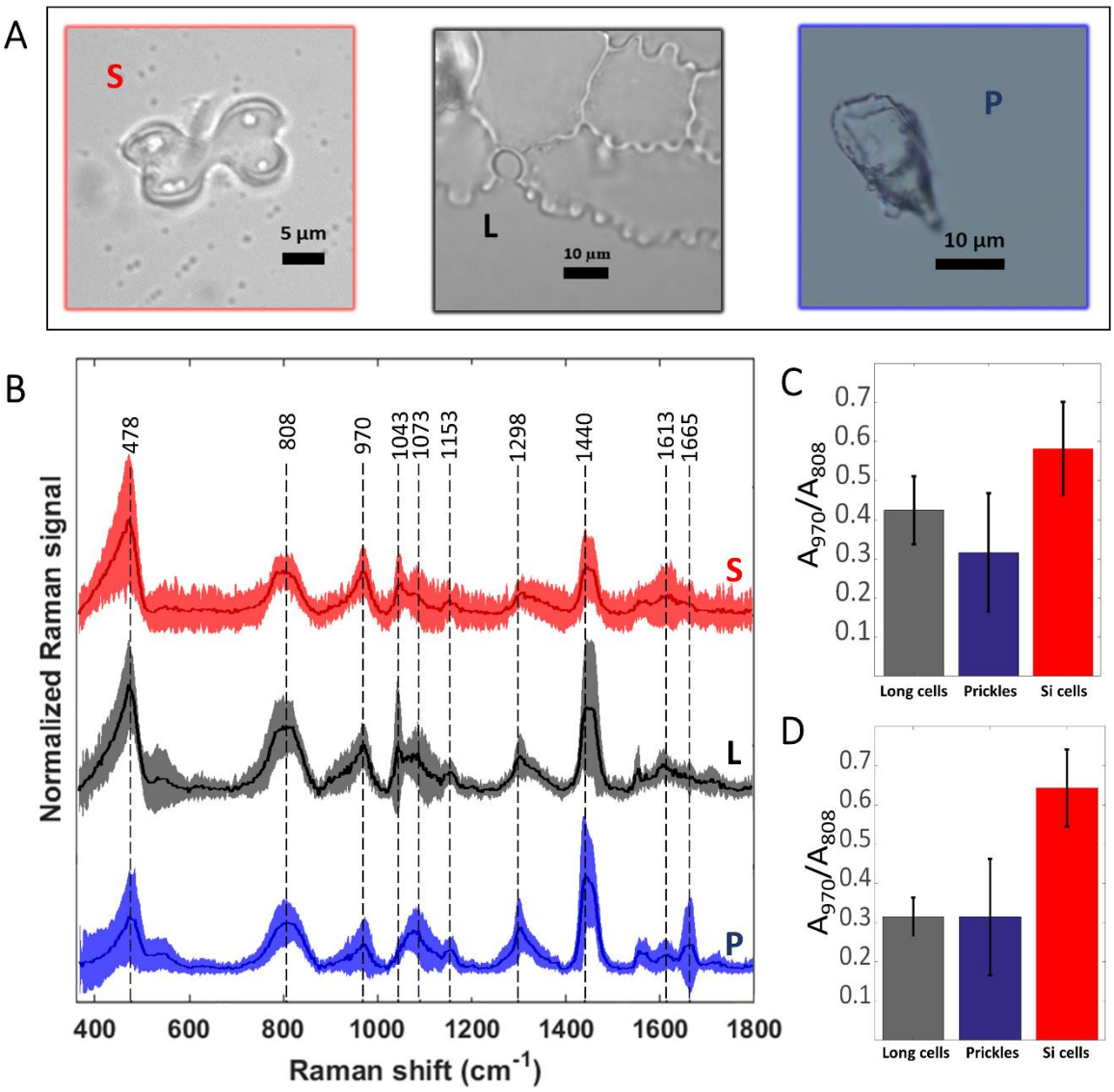

Figure 4.6: Preprocessed mean Raman spectra of the most abundant sorghum leaf phytoliths and intensity ratio of the Si-OH to Si-O-Si Raman bands. Bilobate silica cells (S, red), long cells or plates (L, black) and prickles (P, blue) are shown in bright-field micrographs (a). Mean spectra ± standard deviation are plotted in the same respective colour and denoted with the same abbreviations (B). Averages of 25 spectra of phytoliths of each type extracted by microwaved-assisted digestion (MAD) are shown. The area of the peak at 970 cm-1, assigned to Si-OH surface groups, was normalized to the area of the 808 cm-1 band, assigned to Si-O-Si stretching. Ratios of band areas calculated in spectra of bilobate cells were significantly higher ($p < 0.05$) than both prickles and long cells under MAD (C) and sulphuric acid-hydrogen peroxide-nitric acid extraction (SONE) (D) methods. Figure reprinted with permission from Zancajo, V. M. R. et al. *Front. Plant Sci*. 10, (2019).

Table 4.2: Raman shifts, IR absorbance maxima and tentative assignment of bands observed in the spectra of extracted phytoliths.

Wavenumber	IR/Raman	Assignment	Ref.
1665	Raman	C=C stretching, C=O stretching and amide I vibrations, Lignin, proteins	89, 145
1613	Raman	C=C stretching or aryl, Lignin and proteins	33,146
1550	Raman	Amide II, proteins	89, 145
1440	Raman	CH_2 deformation	89, 145
1298	Raman	CH_2 deformation in alkane long chains	89
1153	Raman	C-C twisting and rocking	89
1000-1250	IR	Si-O-Si asymmetric bond stretching	147
1073	Raman	Si-O-Si asymmetric bond stretching	144
1043	Raman	ring vibrations of substituted benzenes and C-C stretch	89
970	Raman	Si-OH stretching	144
808	Raman/IR	Si-O-Si symmetric stretching	144
478	Raman	Si-O-Si bending	143

PCA of the Raman spectra discriminates between the two extraction methods similar to the bulk analyses. Nevertheless, the separation was particularly clear when the PCA was applied only to the spectra of long cells (Figure 4.7A). The loadings indicate the source of the variation, reveal differences in the silica structure and the amount of occluded organic matter (Figure 4.7B).

When all spectra were included in the analysis, the separation between phytoliths from different cell types was achieved, regardless of the extraction method (Figure 4.8A). However, the phytolith types were better discriminated using only the Raman spectra of the phytoliths obtained by SONE (Figure 4.9A), highlighting the influence of the remaining organic matter. These differences in the spectra could be further studied based on the PCA loadings. In both, the full data set including both digestion methods (Figure 4.8B) as well as in the data set obtained only after wet digestion (Figure 4.9B), the highest variation, lies in the broad band between 440 and 500 cm^{-1} and the band at 1435 cm^{-1} and is represented by PC1 (Figure 4.9B). It increases as the band at 1435 cm^{-1} decreases and increases with the bands at 475, 808 and 970 cm^{-1}.

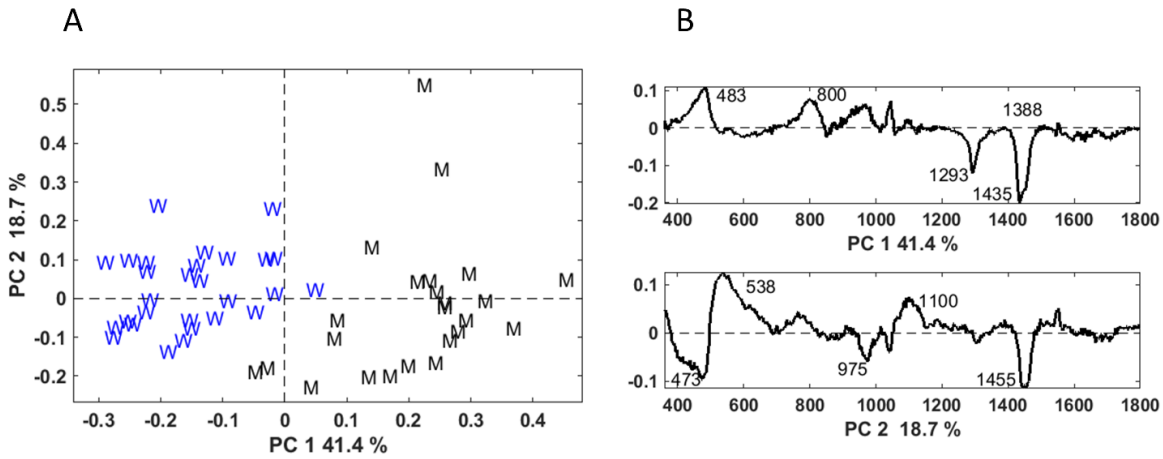

Figure 4.7: Discrimination between long cell phytoliths extracted by two methods based on Raman microspectroscopy. (A) PCA scores plot of long cell phytoliths (plate fragments). W in blue represents long cells extracted by SONE and M in black represents long cells extracted by MAD. (B) PCA loadings showing the contributions of original variables to PC 1 and PC 2 in panel A. The contribution to the loadings of the first principal component indicates that the separation was based on the organic matter present in the silica and the amount of silanol groups on its surface (bands at 483, 800 and 970 cm^{-1}). The band around 800 cm^{-1} was assigned to the Si-O-Si symmetric stretching mode, and at 975 cm^{-1} to silicon-oxygen stretching modes of Si-OH groups. Figure adapted with permission from Zancajo, V. M. R. et al. *Front. Plant Sci.* 10, (2019).

In the scores plot, long cells and prickles appeared at negative values of PC1, indicating a higher contribution of the 1435 cm^{-1} CH_2 deformation band, associated with the presence of lipids.[89] The vibrational modes of Si-O-Si and Si-OH also contribute to the highest variation and are directly related to the silica condensation. The silanol groups (Si-OH) stretching modes appeared in Raman spectra in the range 960-990 cm^{-1}. The intensity ratio of this band to the band at 808 cm^{-1} estimates the hydroxyl density in the different phytoliths (Figure 4.6 C and D). This last band can be used for normalization since it is a lattice band characteristic of the silica network and remains unchanged in different silicas.[148] The higher ratio for bilobate cells indicate a lower degree of condensation of the silica, and therefore a higher number of silanol groups, in the bilobate cells in comparison to that in prickles and long cells.

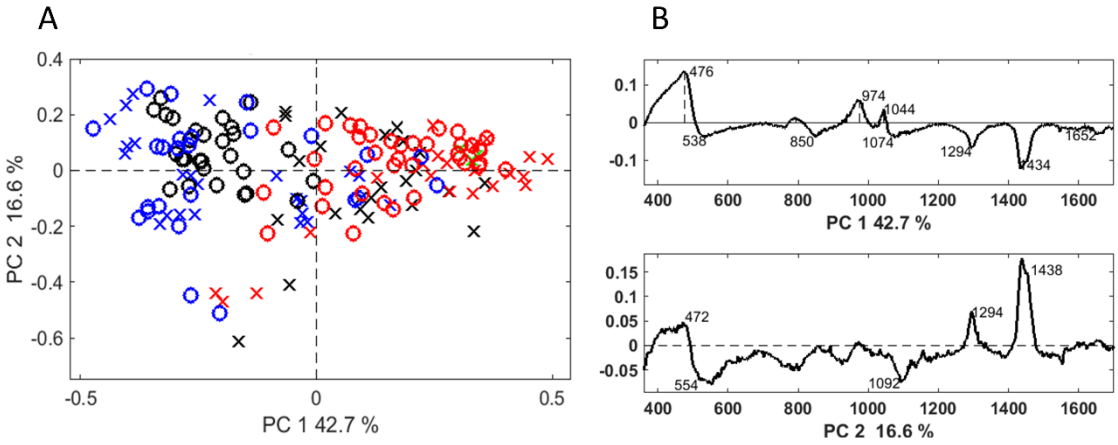

Figure 4.8: Discrimination of Raman spectra of individual phytoliths extracted by two methods. (A) PCA scores plot of the phytolith Raman spectra showing discrimination between phytolith types: prickles (blue), long cells (black), and bilobate silicified cells (red), extracted by MAD (X) or SONE (O). (B) Loading spectra of PC1 and PC2, indicating bands responsible for the separation. Figure adapted with permission from Zancajo, V. M. R. et al. *Front. Plant Sci*. 10, (2019).

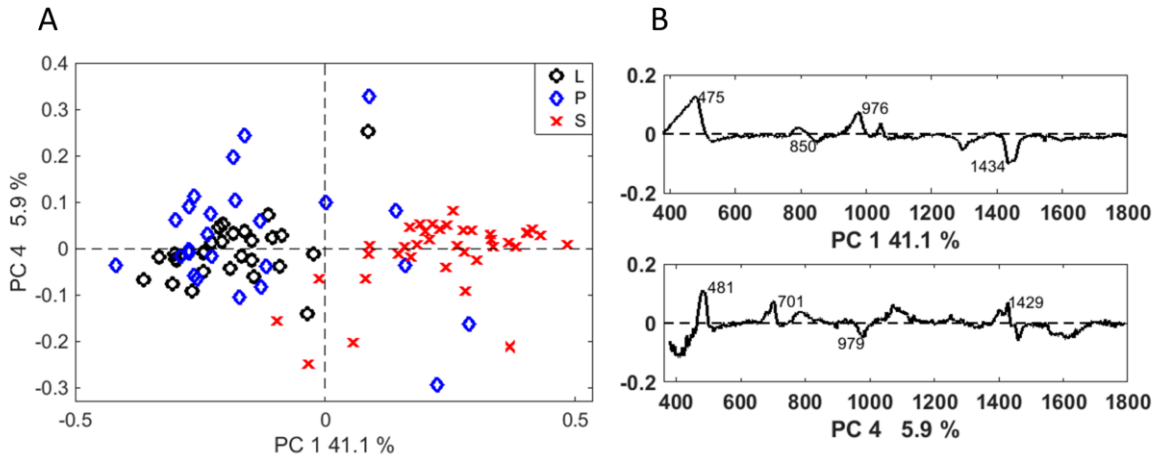

Figure 4.9: Discrimination of Raman spectra of individual phytoliths extracted by SONE. (A) PCA scores plot showing the discrimination between phytolith types (long cells (L, black), prickles (P, blue), and bilobate cells (S, red)). (B) Corresponding loading spectra of PC1 and PC4. Figure adapted with permission from Zancajo, V. M. R. et al. *Front. Plant Sci*. 10, (2019).

PCA was also applied to the derivatives of the phytolith Raman spectra (Figure 4.10). The variance explained by the principal components (Figure 4.10B) is smaller than in the analysis of the Raman original spectra (Figure 4.9). This indicates that the calculation of derivatives removes structural information contained in the baseline of the spectra. According to the loadings of the PCA, the discrimination was based on the differences in the shape of the band between 440 and 500 cm^{-1} and the spectra region between 1420 to 1460 cm^{-1}. Although the separation in this occasion was not so clear, phytolith types could be discriminated and interestingly the score plot showed higher dispersion and variation within the group of the bilobate silica cells.

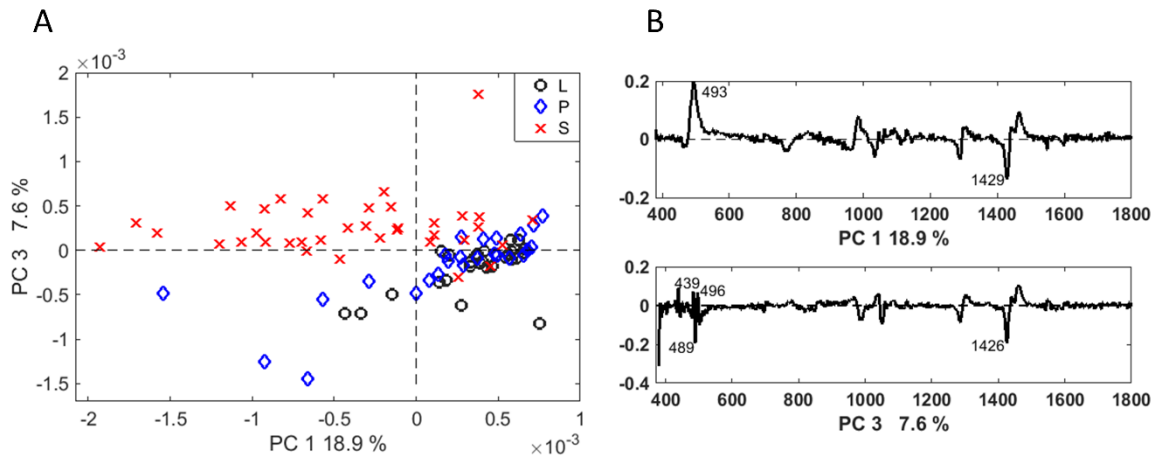

Figure 4.10: Discrimination between phytolith types based on the first derivatives of the Raman data shown in Figure 4.9. (A) PCA scores plot of long cells (L, black); prickles (P, blue); and bilobate cells (S, red). The long cells are more compactly grouped whereas the bilobate cells showed higher variation. (B) Loadings of the PCA indicating that the discrimination was based on the differences in the shape of the band between 440 and 500 cm^{-1} and the spectral region between 1420 to 1460 cm^{-1}. Figure adapted with permission from Zancajo, V. M. R. et al. *Front. Plant Sci*. 10, (2019).

4.4.2. Comparison of synchrotron infrared microspectra of long cells and silica cells phytoliths

The highly abundant long cells and bilobate silica cells were further characterized by FTIR microspectroscopy, aiming to complement the vibrational analysis obtained by Raman spectroscopy (Figure 4.9). The main features of the IR spectra were attributed to the silica itself: the band at 800 cm^{-1} is assigned to the deformation of Si-O-Si bonds bridging between two adjacent tetrahedra and the bands at 1000-1250 cm^{-1} were assigned to Si-O asymmetric stretching modes.[147] The highest absorbance values of silicified long cells appeared at 1093 cm^{-1}. In the silica cells, the maximum of the Si-O asymmetric stretching band was shifted to 1020 cm^{-1}, indicating variations in the mineral structure between the phytolith types of both cells (Figure 4.11A).

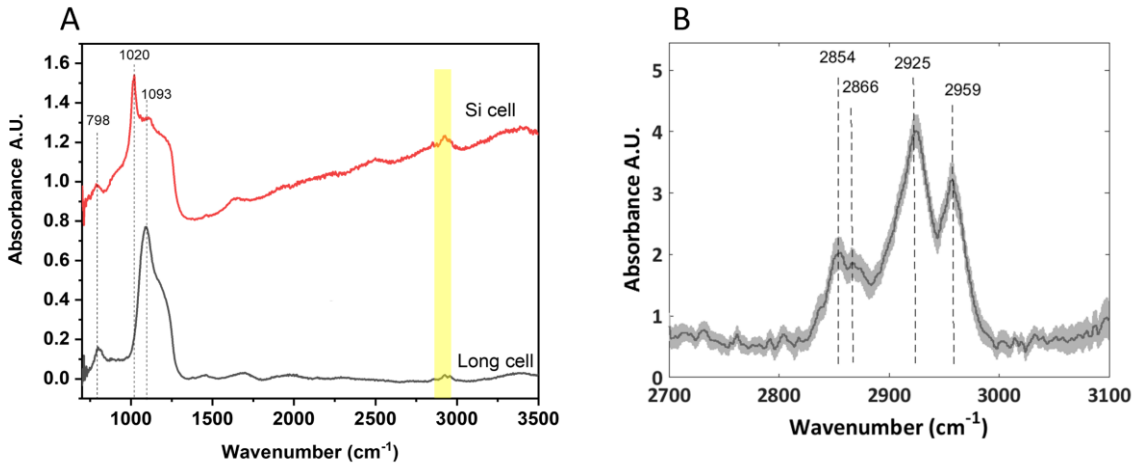

Figure 4.11: Synchrotron Fourier transform infrared (FTIR) spectra of long and bilobate cells extracted by SONE. (A) Representative spectra of long and bilobate cells. Yellow shade at 2,700–3,000 cm^{-1} showing bands typical to hydrocarbons. (B) Average FTIR spectra ± standard error of long cell phytoliths in the range 2,700 to 3,100 cm^{-1}. Figure adapted with permission from Zancajo, V. M. R. et al. *Front. Plant Sci.* 10, (2019).

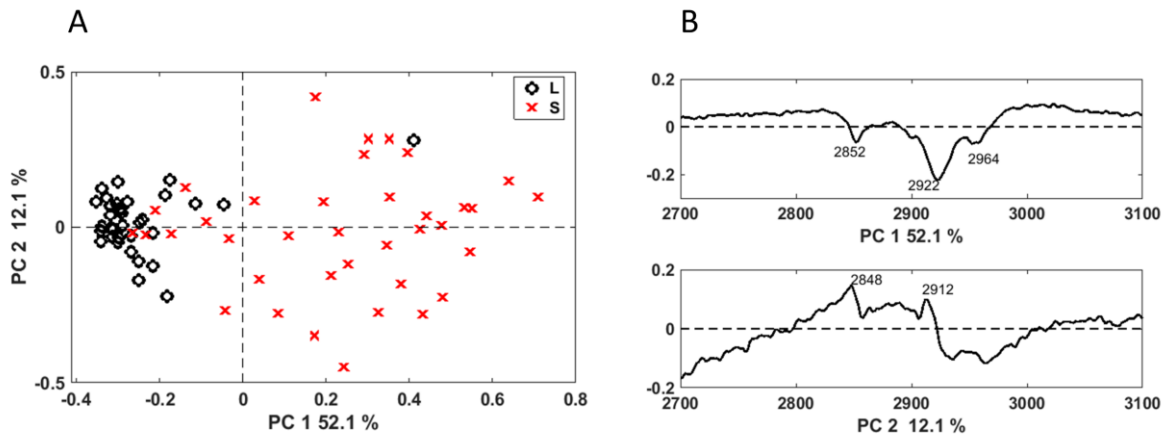

Figure 4.12: (A) Scores plot of a PCA at the spectral region 2700–3000 cm^{-1} attributed to the organic matter occluded in long (L) and silica (S) cells. The two phytolith types are separated. (B) Loadings of the PCA correlate the discrimination with the terminal -CH_3 and CH_2 groups absorption bands. Figure adapted with permission from Zancajo, V. M. R. et al. *Front. Plant Sci.* 10, (2019).

Vibrational bands in the 2700-3100 cm^{-1} region confirmed a considerable amount of organic matter remaining linked to the extracted silica. Magnification of this region of the average spectra of the long cells is shown in Figure 4.11 B, with bands at 2854, 2866, 2925 and 2959 cm^{-1} which are attributed to C-H stretching in -CH_3 and CH_2 groups.[149] These bands were expected in biological material due to the presence of terminal -CH_3 and of CH_2 groups in cellular components like proteins and carbohydrates, and especially lipids. PCA of the spectra in the range 2700-3100 cm^{-1} separated the data of long cells and bilobate silica cells (Figure 4.12A). As evidenced by the loadings (Figure 4.12B), the contributions of the organic material lead to this separation, indicating a higher amount of organic matter in the long cells. Spectra from long cells and bilobate silica cells were also discriminated based on Infrared spectra second derivatives (Figure 4.13 A). Loadings of the PCA (Figure 4.13 B) indicated differences between the phytolith types in the band around 1000 cm^{-1}, related to the silica structure, in agreement with the Raman analysis.

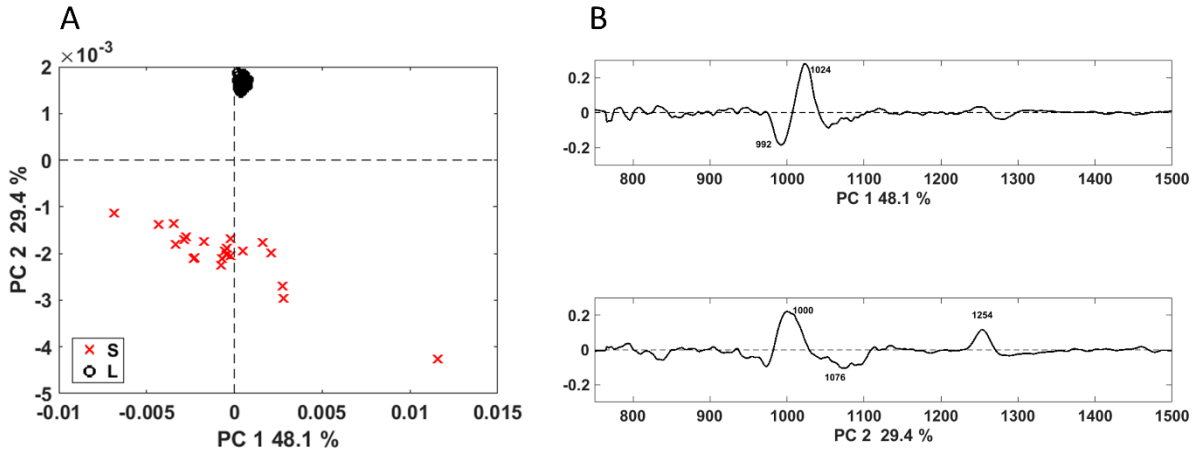

Figure 4.13: Discrimination between phytolith types based on Infrared spectra second derivatives. Synchrotron Fourier transform infrared spectra were collected from long (L) and bilobate (S) cells extracted by SONE. (A) PCA scores plot of the spectral second derivative in the range of 700-1500 cm^{-1} showing strong separation between the cell types. The silica cells exhibited high variation in the scopes of both PC1 and PC2 whereas the long cells seemed to be more homogeneous. (B) Loadings of the PCA indicated differences between the phytolith types in the band around 1000 cm^{-1}, related to the silica structure, in agreement with the Raman analysis (Figure 4.9). Figure adapted with permission from Zancajo, V. M. R. et al. *Front. Plant Sci*. 10, (2019).

4.5. Conclusions

This chapter presents the characterization of sorghum phytoliths in terms of location, structure and chemical composition by SEM-EDX, NMR, TGA and vibrational micro-spectroscopic methods combined with PCA. Silica is unevenly distributed in the sorghum leaf tissues (Figure 4.1B), it is deposited in trichomes, bilobate short cells in parallel rows in the veins, cross cells in regular patterns on the epidermis, papillae randomly distributed and a sparse layer beneath the leaf cuticle. Furthermore, sorghum biosilica forms several structures that exhibit different degrees of silicification. Differences between phytoliths are not limited to their distribution and location in the tissues but also exist in their chemical composition. Concerning to the aim of this thesis the structure of extracted phytoliths enables the following conclusions regarding the phytolith structure, types and formation possibilities.

4.5.1. Differences between phytolith types

All phytoliths are composed mainly of silica, but they have shown to differ in the remaining organic matter present after extraction and in the silica nanostructure and ultrastructure. In agreement with the initial hypothesis that the phytoliths produced by diverse cell types will vary in their chemical composition, it was possible to discriminate between phytolith types extracted from the same sorghum leaves. Bilobate silica cells, silicified long cells and silicified prickles were the most abundant types of phytoliths recovered. Long cells and prickles showed to contain a bigger fraction of organic matter in comparison with bilobate phytoliths and a lower amount of silanol groups. According to previous studies that discuss hydroxylation and amount of organic matter and dissolution rates.[150] The differences found here are expected to significantly influence the dissolution of phytoliths with important implications for morphotype-based archaeological and paleoecological interpretation.[134]

It was assumed that the harsh extraction conditions could alter and mask genuine variations between phytolith types.[61] Evidence is provided here that the extraction method changes the silica structure. The number of silanol groups on the silica surface was drastically altered upon extraction, this effect was particularly clear with long cells which react differently to the extractions. The silica extracted by both methods was formed by spheres, in agreement with previously reported extracted plant silica.[151] It is unlikely that the extracted silica represents the actual silica in the plant. Silica goes through the well-known process of Ostwald ripening,[32, 152] where smaller, more soluble spherical particles dissolve and subsequently the silica condensates on the surface of bigger silica particles with lower solubility until the equilibrium is reached. The solubility of the silica depends not only on the silica particles size but also on the temperature, pH, impurities and other ions present. Therefore, the extraction method has a strong influence on the structure of the silica. The extraction method also alters the remaining organic matter and needs to be carefully considered when extracting phytoliths. The best approach, although also much more challenging, to understand the formation mechanisms would be to study plant silicification *in situ* in the native tissues.

4.5.2. Potential plant biosilica formation mechanisms

The diversity of silica accumulations and microscopic distribution within the plant tissues together with the different chemical signatures suggest that the mineral deposits through a cell type-dependent pathway. Prickles and long cells comprised by a spongy silica structure intermixed with the cell wall components, could be the consequence of accumulation involving the mineral impregnation of a cuticle-cellulose matrix, slowly and over long periods of time.[87, 153-156] A passive way of silicification seems reasonable, as it would happen due to the high concentrations of silicic acid in the plant sap, the constant Si influx and the ability of cell wall to act as a template for silica deposition.[157-159] However, this passive type of silicification does not suffice to explain the intensive and distinctive silicification of the bilobate cells. Bilobate silica cells are heavily and compactly silicified with a low fraction of organic matrix, as indicated by the Raman and IR data presented here. The structural differences are in agreement with the different silicification mechanisms that have been proposed. The silicification mechanism of bilobate silica cells is suspected to be an active and physiologically regulated process,[56] they silicify over a few hours[5] and even in absence of transpiration[40] and under drought conditions, their silicification is preferred over other phytoliths like trichomes.[160] Protein involvement during their silicification is suspected. Acidic proteins and glycoproteins are found in association with mineral phases encapsulated in phytoliths.[60, 161] Specifically, in bilobate, protein residues were identified embedded in their silica.[61] A protein (Siliplant1) was identified inside sorghum bilobate cells able to precipitate silica in a similar way as silaffins and silicateins.[62] The possibility of this protein mediating silica deposition is further explored in Chapter 7. Nonetheless, although bands associated with amino acids and proteins were identified in all types of phytoliths, they did not contribute to the discrimination between phytolith types. Other organic compounds such as lipids and carbohydrates were found here to be much more abundant than proteins in the extracted sorghum phytoliths. The data presented here do not support previous observations reported as evidence of silicon covalently bound to organic components.[42-44] The presence of silicon atoms bound to organic components could not be excluded either, as their amount may be too small to be unambiguously detected. The results presented here show clear structural differences between phytolith types

and suggest that more than one mechanism of silica deposition is involved in sorghum leaf phytoliths formation. Observed variations in the silica are a consequence of the extraction processes, therefore more research is needed to elucidate the native state of the silica. This is attempted in the next chapters. More research is also needed to identify the occluded organic matter and the details of the chemical mechanisms that lead to the plant biosilica formation.

Chapter 5

Sorghum leaf as a model for multimodal microspectroscopic analysis

The visualization of microscopic areas of plant tissues is a prerequisite to understanding these complex structures, how are they formed and their specific physiological role. Visualizing and quantifying the different components of plant tissues has been a challenging but important research question that has attracted attention across a broad range of fields, including plant molecular biology, agronomy, plant physiology, plant nutrition, and ionomics. Early studies proved microscopic techniques such as bright-field microscopy,[25, 40] fluorescence microscopy[162] and scanning electron microscopy[162, 163] very useful and thus, they are still widely used. More recently Raman and infrared (IR) microspectroscopy have become routine tools applied in plant science to visualize the tissues. The advantage of fluorescence and microspectroscopy techniques is that in addition to images, they provide spatially resolved chemical information on the components present. Autofluorescence emission of intact leaves is a genuine property and characteristic of the cell walls of all green plants.[164] Fluorescence microscopy provides information regarding the chemical compounds present, for instance, it was used to locate ferulic acid in the pericarp layers.[162] But it is limited due to the need of using specific excitation sources and filters for each, when present, autofluorescence compounds. Micro-spectroscopic imaging or hyperspectral imaging, on the other hand, provides much more diverse chemical information. It refers to analytical techniques which map sample surfaces with micrometric resolution and acquire a full spectrum in every pixel of the resulting image. Both IR and Raman spectroscopies have been very successfully coupled with a

microscope and applied to plant analysis, in order to visualize micro-structures and provide their chemical composition. These methodologies allow obtaining spatially resolved information, in a non-destructive way, although each of them has its limitations and advantages. The limitations regarding sampling requirements, available diagnostic bands, spectral interferences, and spatial resolution generally dictate the choice to use one over the other. Nevertheless, both have been used in plant science,[165, 166] specially combined with multivariate methods.[167] Chemical imaging resolves spatially distributions of lignin, cellulose, carbohydrates, protein and lipids, which can be mapped, and therefore the differences in organ composition can be evaluated. Before creating the image, the band used should be unambiguously assigned. The assignment of a band to a specific vibration of a particular molecule is crucial but not trivial. Band assignment in Raman spectra of plant tissues is not easy, because, despite the vast and continuously increasing literature, it is a matter of debate and in some cases conjecture. Several approaches exist for band assignment of plant tissue components. Density functional theory (DFT) predictions of simulation models are commonly used.[168] Single components[169] or models,[170] precursors, or similar chemicals used as standards sometimes serve to assign the bands in the spectra. Additionaly, direct assignment of the compounds after chemically treat the tissues with a predicted result and comparison of spectra taken after the treatment and the original spectra show to be also useful.[171] All of these methods, though very helpful, have their limitations. Namely, calculations are approximations and give a good idea of what to expect but often are not in total agreement with experimental measurements, as complex matrix may influence the band position and shape. Vibrational spectra of monomeric compounds may not resemble the spectra of the polymers they form. This is the case of monolignols such as coniferyl alcohol and ferulic acid and the polymers that they form (see Raman spectra shown in Figure 7.1). The difficulties to obtain reliable assignments lay on the complex yet similar molecules that form the plant cell walls. Lignins, cellulose, hemicellulose, pectins and so on, all contain similar functional groups and types of bonds between C, H and O. They are big molecules and polymers which produce rich and complex vibrational spectra, and, in many cases, they crosslink to form the plant structures producing overlapping bands and similar Raman signals. The identification of single components is extremely challenging, nevertheless there are some specific vibrations than can be

unambiguously assigned to a specific compound. For example, the band around 1600 cm^{-1} is used to map the lignin distribution. When using excitation wavelength of 532 nm, it is a pre-resonantly enhanced Raman band, involving aromatic C=C and C=O stretches. Nevertheless, the spectra are complicated and before meaningful chemical maps can be created, a careful consideration of the spectra needs to be undertaken. The evaluation of large spectroscopic data sets is complex due to the huge amount of information contained. A common approach to assess large spectroscopic data set like Raman maps is the combination with multivariate analysis. Multivariate algorithms including vertex component analysis (VCA), non-negative matrix factorization and multivariate curve resolution–alternating least squares (MCR) were applied to plant Raman spectroscopic data sets to evaluate the chemical composition of plant tissues.[167] VCA was recommended as a preliminary approach due to its speed, not requiring many input parameters and the good resulting endmembers as an approximation of the raw data. Principal component analysis (PCA) is one of the preferred exploratory data analysis in data science and it is used in a wide variety of fields.[172] It is a simple, non-parametric method able to reduce and extract relevant information, and thus, it is particularly interesting to understand the chemical information contained in vibrational spectra.[93]

Scanning electron microscopy (SEM) achieves higher resolution than bright-field microscopy, providing greater detail of the plant tissues and tissue boundaries but also subcellular structures. Coupled with energy dispersive X-ray spectroscopy (EDX), SEM-EDX enables the visualization and mapping of the elemental composition.

This chapter presents the visualization by bright-field and fluorescence microscopy of leaf cross-sections freshly cut or after paraffin embedding, extracted from sorghum plants grown with and without silicic acid supplementation. The chemical composition was assessed by Raman and IR imaging combined with multivariate methods and the silica distribution and the details of the structures visualized by SEM-EDX. The information obtained and the capabilities of chemical imaging using multivariate methods such as PCA, VCA and hierarchical cluster analysis (HCA) are explored, evaluated and compared.

5.1. Fluorescence images of cross-sections

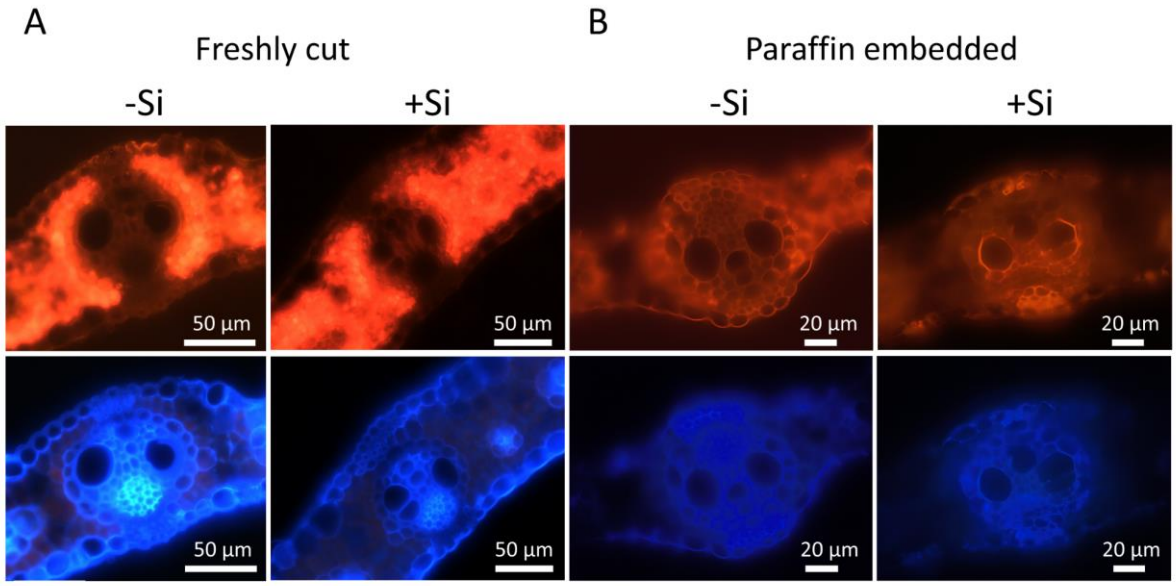

Figure 5.1: Fluorescence microscopy images of leaf cross-sections of sorghum plants grown with and without silicic acid supplementation. (A) freshly cut samples and (B) samples after fixation, dehydration and paraffin embedding. The upper images show red autofluorescence taken with excitation with wavelength at 530-550 nm and a cut off filter at 575 nm. The lower images show blue autofluorescence taken with excitation with wavelength at 330-385 nm and a cut off filter at 420 nm.

The red autofluorescence images taken with excitation at a wavelength at 530-550 nm, cut off filter at 575 nm of the freshly cut samples (Figure 5.1A upper images) showed high fluorescence in the chlorenchyma and bundle sheet, presumably due to chlorophyll fluorescence.[164] This strong fluorescence patterns observed in fresh samples were not observed in the samples prepared for IR analysis (Figures 5.1B upper images). This was probably a consequence of the fixation, dehydration, paraffined embedding and deparaffination process needed for the Fourier transformed infrared (FTIR) analysis, which seemingly removed or modified the compounds responsible for the fluorescence. Red fluorescence was also observed in some samples in the fibre cells (sclerenchyma) above and below the vascular bundle (Figure 5.1 B), however, it appeared randomly rather than associated to the silicon treatments. Strong blue autofluorescence in phloem regions, veins and some spots on the epidermis was

observed with excitation at 330-385 nm and 420 nm filter (Figure 5.1A lower images). The compound responsible for the autofluorescence on the epidermis is probably ferulic acid,[164] however due to the lack of specificity of the fluorescence microscopy, the compound responsible for the phloem fluorescence remains unknown. In this case, fluorescence was also diminished after the preparation for FTIR analysis (Figure 5.1B lower images). The images taken from plants grown with silicic acid supplementation showed similar patterns of autofluorescence.

5.2. Raman and IR spectra of sorghum leaves and band assignment

Raman spectra taken from sorghum leaf tissues are rich in bands (Figure 5.2A) but mostly dominated by the 1597 cm^{-1} band. The maxima of the most intense bands found in sorghum leaves tissues are summarised in Table 5.1 together with tentative assignments to molecular vibration and cell wall components according to the cited literature.

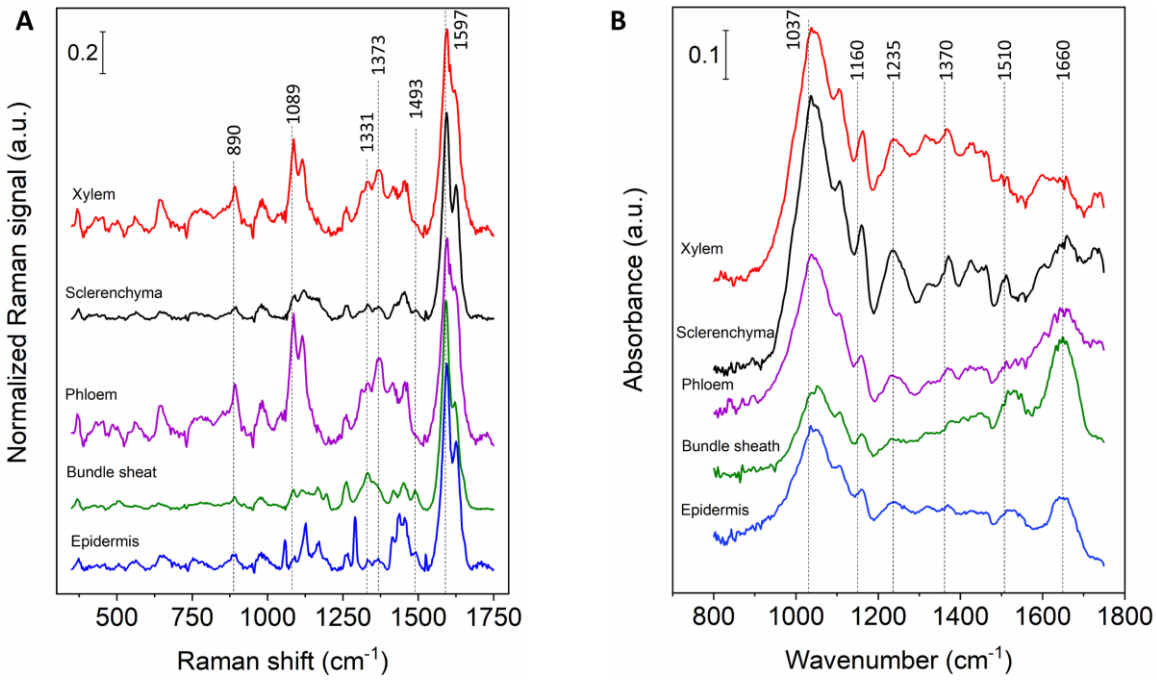

Figure 5.2: (A) Average Raman spectra of the epidermis, bundle sheath, phloem, sclerenchyma and xylem of sorghum leaves and (B) FTIR spectra of the epidermis, bundle sheath, phloem, sclerenchyma and xylem of sorghum leaves. For orientation, some vibrations are labelled.

The aromatic C=C and C=O stretching vibrations of lignin which appear between 1550 cm^{-1} and 1660 cm^{-1} are discussed in detail in section 5.5.3. Another visible band that can also be attributed to lignin regardless of the lignin type is visible at 1438 cm^{-1}, assigned to $\delta(O–CH_3)$. This band is not specific as it has a contribution from $\gamma(CH_2)$ that is present in many organic molecules.[173] Types of lignin, in the sense of monolignols (S, G and H units) that form the polymer, have shown to generate Raman spectra with characteristic bands.[174] The band 1331 cm^{-1} (aliphatic O-H bend) is especially prominent in spectra from the bundle sheath and arises from the presence of sinapyl units in lignin.[175, 176] The band at 1373 cm^{-1} was assigned to both, guayacil and sinapyl units and is more intense in xylem and phloem spectra than in the rest of the tissues. Lignin formed of G units can be identified by the presence of bands at 1277 cm^{-1} and 560 cm^{-1}, whereas the band 1177 cm^{-1} (assigned to C_6H_5-C) is characteristic of H lignin units and has been observed in grass lignin.[176] The second most prominent feature of the Raman spectra, clearly visible in the spectra taken from xylem and phloem, was the characteristic doublet of cellulose at 1089 cm^{-1} and 1115 cm^{-1} (Figure 5.2A). These bands are assigned to C-C and C-O stretches, which in sorghum appear at slightly lower frequencies than commonly reported.[110, 111, 113] The band at 890 cm^{-1} was assigned to skeletal deformation and side chains of cellulose and hemicelluloses.[176] Several bands at lower Raman shifts including 520 cm^{-1}, 498 cm^{-1}, 428 cm^{-1} and 370 cm^{-1} (γ(COC), δ(HCC), δ(HCO), δ(HOC) and δ(CCC) ring) originate from polysaccharide compounds such hemicelluloses.[175-177] These low frequency bands overlap the Si-O-Si bending vibration, which is expected as a wide and very low intensity band.[143] This resulted in the infeasible identification of silica in Raman spectra of sorghum leaves. The other expected characteristic silica bands did not confirm the presence of silica. The Si-O-Si symmetric stretching that should be present at around 800 cm^{-1} was not observed, and the ν(Si-OH), expected at 975 cm^{-1}, overlapped with the ν(CC), ν(CO), ν_{sym}(COC) and ω(CCH) of cellulose and hemicelluloses.[109] Most of the Raman spectra showed a band at 1524 cm^{-1}, assigned to the ν1 of carotenoids.[178] In the spectra taken from the epidermis, intense bands were detected at 1456 cm^{-1} CH_2 bend, 1418 cm^{-1} $\delta(CH_2)$, $\delta(CH_3)$ and 1260 cm^{-1} δ(CCH), presumably due to the presence of waxes and aliphatic compounds in the cuticle.[179] The bands at 1197 cm^{-1} and 1493 cm^{-1} observed in spectra taken from the bundle sheath and some spectra of sclerenchyma, appear together but are not mentioned in the plant spectroscopy literature known to the

author. The former could be assigned to C-H bending and the latter could be attributed to C-N stretching vibration coupled with the in-plane C-H bending of amino radical cations, or C=C skeletal of aromatic compounds.[89]

The FTIR spectra of fixed and deparaffinized tissues of sorghum leaves contained fewer bands than the Raman counterparts but were also rich in information. Representative spectra taken from different tissues are shown in Figure 5.2B. The maxima of the most intense bands are summarised in Table 5.2 together with tentative assignments to molecular vibration and cell wall components according to the cited literature. In contrast to the Raman spectra, the FTIR spectra showed the most intense band between 900-1200 cm^{-1}. This complex feature is commonly observed in plant samples and arises from the ν(C-O-C) of carbohydrates such as cellulose and hemicelluloses.[96, 180] The Si-O stretching is also expected around 1100 cm^{-1} in samples containing silica, nevertheless, in sorghum spectra, it gets masked by the other spectral features. Amide I, II and III were identified at 1660 cm^{-1}, 1510 cm^{-1}, 1315 cm^{-1} respectively,[181] although absorbances at these frequencies are not exclusive of amino acids and can have the contribution of other organic compounds such as lignin.[182] The band at 1370 cm^{-1} (assigned to the $\delta(CH_3)$ and $\delta(CH_2)$) was very intense in spectra from sclerenchyma and xylem. This band appeared together with the band at 1235 cm^{-1} which was assigned to ν(C-C), ν(C-O), ν(C-O), and ν(C=O) and is specific of lignin.[182] The complexity and variability of these spectra are such that it is difficult to extract the relevant information from them by visual inspection, especially considering that the maps contain several thousands of spectra. The vibrations observed in Raman and FTIR spectra of sorghum leaves that are mentioned here do not appear in all tissues, and multivariate analysis was needed to evaluate the big spectroscopic data sets.

Table 5.1: Raman bands, assignment to molecular vibration and tentative assignment to cell wall component according to the cited literature.

Raman shift/(cm^{-1})	Assignment	Compound	References
1651	Ring conjugated ν(C=C) and ν(C=O)	Coniferyl alcohol, p-coumaric and ferulic acid	[183],[169], [184], [177]
1631	Symmetric stretching phenyl ring	Lignin compound	[185], [186]
1624	Ring conjugated ν(C=C)	Lignin G, coniferyl aldehyde, coniferyl alcohol, coniferaldehyde/sinapaldehyde	[187], [169]
1613	Aromatic ring mode	Biphenyl in lignin	[146]
1597*	Symmetric stretching of the aromatic ring	Lignin compounds	[173]
1570*	Phenolic radicals	Lignin radicals	[187]
1524	ν(C=C)	Carotenoids	[178]
1493*	ν(C=C) skeletal and ν(C-N) δ(C-H) amino radical cations	Aromatic compounds and proteins	[89]
1462*	$\delta(CH_2)$, $\delta(CH_3)$ δ(HCH), δ(HOC), $\delta(O–CH_3)$, $\delta(CH_2)$ and guayacil ring (with C=O)	Oleanolic acid Callose, lignin and cellulose	[188], [165]
1456	$\delta(CH_2)$	Aliphatic compounds	[179]
1438	$\delta(O–CH_3)$, $\gamma(CH_2)$	Lignin	[189], [188]
1418	δ (CH_2), δ (CH_3)	Aliphatic compounds	[179]
1373	ν_s(C-O-C) of O-CH_3 groups and aryl–OH or aryl–O–CH_3	Cellulose and Lignin S and G units	[109], [174]
1360	Ring mode	Biphenyl	[146]
1331	δ(O-H)	Lignin S units	[175] [176]
1290	$\delta(CH_2)$, $\delta(CH_3)$	Aliphatic compounds	[179]
1277*	C–C-H, C-O–H, and $\delta(CH_2)$, aryl-O of aryl-OH and aryl-O-CH_3	Lignin G units	[175]
1260	δ(CCH)	Aliphatic compounds	[179]
1197	δ(CH)	Biphenyl in lignin	[89, 146]
1177*	C_6H_5—C	Lignin HG units and p-coumaric/ferulic acid	[176] [175]
1127	ν(CC)	Aliphatic compounds	[179]
1115*	ν(CC)	Cellulose	[110, 113, 176]
1089*	ν_s(COC), ν_{as}(COC), δ(HCC), and δ(HCO)	Cellulose	[110, 113, 176]
980	ν(CC), ν(CO), ν_s(COC) and ω(CCH)	Cellulose (xylem and endodermis)	[109]
~975†	ν(Si-OH)	Silica	[144]
890*	Skeletal deformation and side chains	Cellulose and hemicellulose	[176]
~808†	ν_s(Si-O-S)	Silica	[144]
640	Skeletal deformation	Lignin	[109]
560	Skeletal deformation	Lignin G units	[175] [109]
520	δ(COC) glycosidic, δ(HCC) and δ(HCO)	Cellulose, hemicellulose and S lignin	[175]
492	δ(HCC), δ(HCO) and δ(COC) glycosidic	Cellulose	[176]
~478†	δ(Si-O-Si)	Silica	[143]
428	γ(COC), δ(HCC), δ(HCO), δ(HOC)	Cellulose, pectin	[176],
370*	γ(COC), δ(HCC), δ(HCO), δ(HOC), δ(CCC) ring	Cellulose and lignin S units	[175], [176], [177]

Chemical images are shown of vibrations marked with * in Figures 5.3 and 5.4. Vibrations expected but not observed are marked with †. ν stretching, δ deformation, ω wagging.

Table 5.2: IR absorption bands, assignment to molecular vibration and tentative assignment to cell wall component according to the cited literature.

Wavenumber	Assignment	Compound	Ref.
1734	ν(C=O) unconjugated, ester carbonyl	Fatty acids, lignin and pectin	[182], [190]
1660	Amide I and ν(C=O) conjugated	Proteins and lignin	[182], [190], [181]
1510	Amide II and ν(C=C),	Proteins, lignins and aromatic compounds	[191], [181]
1460	$\delta_{as}(CH_3)$ and $\delta_{as}(CH_2)$	Proteins, lipids and lignin	[182]
1425	ν(COO–), aromatic skeletal vibrations	Pectins, lignin and polygalacturonic acids	[182], [190]
1370	$\delta(CH_3)$ and $\delta(CH_2)$	Lignin but also proteins, lipids	[182], [190]
1315	C-C C-O, ν(C-H) and δ(N-H) amide III	Proteins	[181]
1235	ν(C-C), ν(C-O) and ν(C=O)	Lignin	[182], [190]
1160	(C-O)	Polysaccharides and hemicelluloses	[180], [96]
900-1200	(Si-O) and (C-O)	Silica, polysaccharides and hemicelluloses	[192, 193]
1037	ν(C-O-C)	Polysaccharides and hemicelluloses	[180, 96]

Vibrations marked with * were mapped and the created chemical images are shown in Figures 5.5 and 5.6.

5.3. Chemical images of sorghum leaf cross-sections

The most straightforward method for spectral data analysis of an area is the mapping of specific functional group intensities and frequencies by peak heights and/or areas. The method is a univariate analysis and thus, only one specific band is considered at a time. It consists of producing chemical maps by plotting the intensity of a band or integrating over a band and plotting the area of the band for each pixel of the area analysed. It is simple, yet it can provide useful information regarding the spatial distribution of targeted compounds if the following considerations are taken. Changes in the baseline are expected even in areas of close proximity due to the presence of fluorescence compounds, electronic noise, etc. therefore baseline must be corrected before a meaningful chemical image is created. The alternative to univariate mapping is producing chemical images based on multivariate approaches. In the next section examples of chemical images created using Principal Component Analysis (PCA), Vertex Component Analysis (VCA) and Hierarchical Cluster Analysis (HCA) multivariate approaches are presented, and the results compared.

5.3.1. Raman band imaging

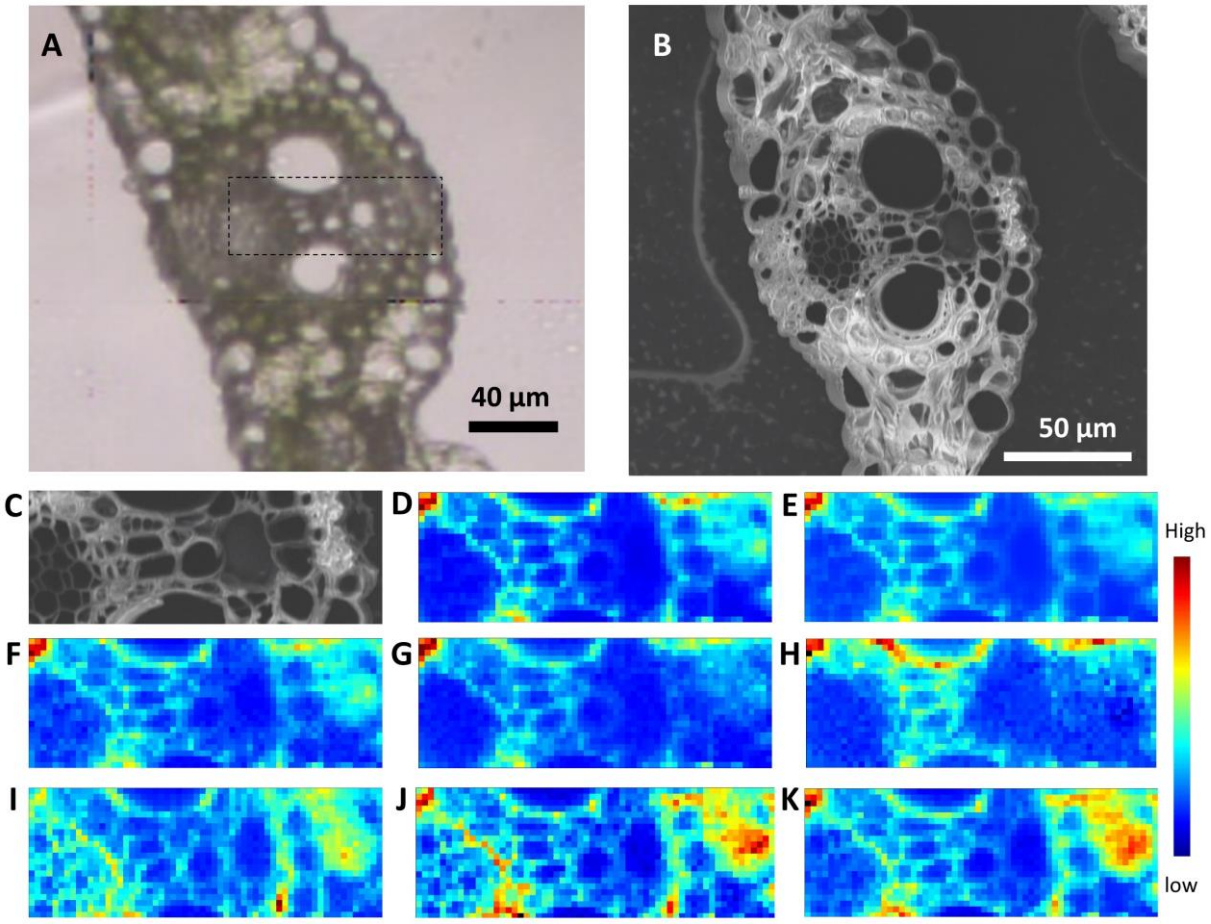

Figure 5.3: Multimodal imaging of a sorghum leaf cross-section grown in absence of silicic acid. (A) Bright-field microscopy image; (B) SEM micrograph of the same area; (C) SEM magnification of the area mapped by Raman. Raman chemical images of the area marked in (A) created by plotting: (D) the band in the region 1550–1700 cm^{-1} characteristic of lignin; (E) the band 1570 cm^{-1} corresponding to lignin radicals; (F) the band 1462 cm^{-1} corresponding to $\delta(CH_2)$ and $\delta(CH_3)$; (G) the band at 1277 cm^{-1} specific of G lignin; (H) the band at 1160-1195 cm^{-1} specific of lignin HG; (I) the band at 1060-1135 cm^{-1} assigned to cellulose; (J) the band at 890 cm^{-1} assigned to cellulose and hemicellulose and (K) the band between 360-400 cm^{-1} corresponding mostly cellulose and hemicellulose. The step size of the chemical images is 1 µm.

The SEM image provided additional detail of the plant structures (Figure 5.3B) and the magnified view (Figure 5.3C) of the area analysed by Raman spectroscopy helped to understand the chemical images created using characteristics Raman bands

(Figure 5.3D-K). The distribution of lignin and lignin radicals was visualized by plotting the bands at 1600 cm^{-1} and 1570 cm^{-1} (Figure 5.3D, E). Lignin was almost absent in the phloem but very high in the xylem. In contrast, cellulose and hemicelluloses were particularly high in the phloem and sclerenchyma (Figure 5.3 I-K). Plotting the ratio 380/1092 bands has been used before to evaluate the crystalline cellulose fraction.[112] In this occasion, it did not provide any contrast in the images (not shown), suggesting a homogeneous distribution.

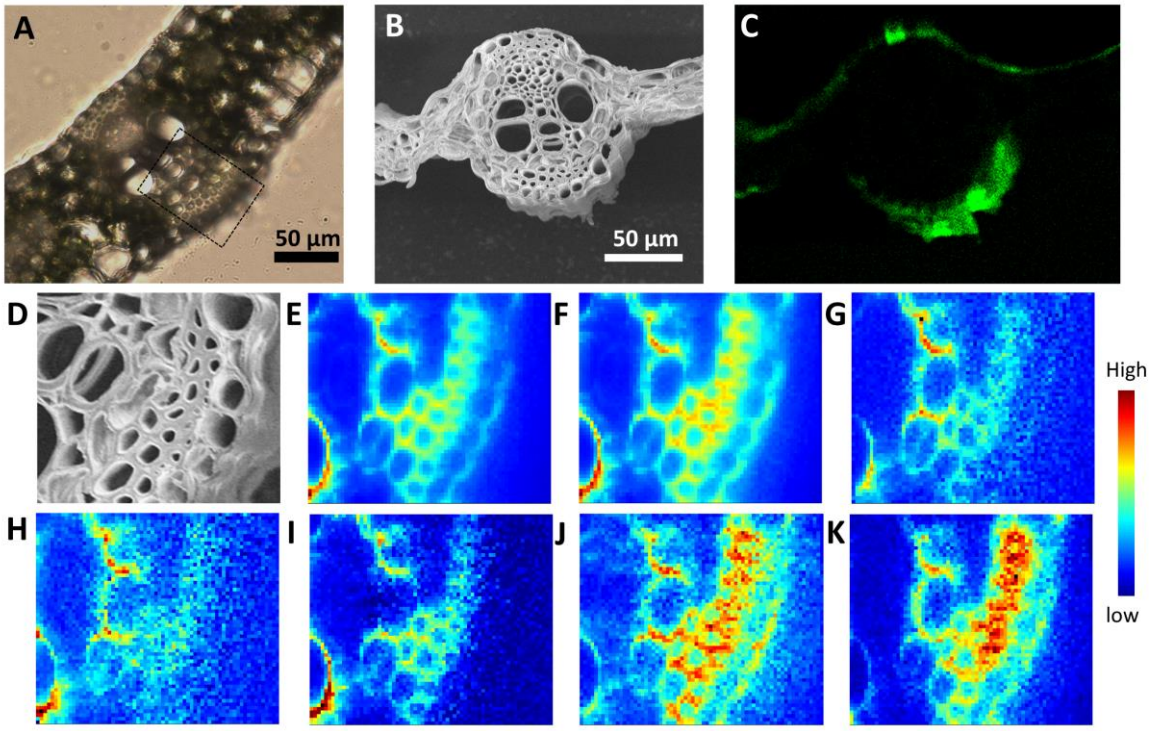

Figure 5.4: Multimodal imaging of a sorghum leaf cross-section grown in with silicic acid supplementation. (A) Bright-field image; (B) SEM micrograph of the same area; (C) EDX image showing the silicon distribution. (D) SEM magnification of the same area analysed by Raman. Raman chemical images created by plotting: (E) the bands 1550-1700 cm^{-1} characteristic of lignin; (F) 1570 cm^{-1} corresponding to lignin radicals; (G) the band at 1493 cm^{-1} corresponding to C=C skeletal and C-N stretching vibrations; (H) the band 1160-1195 cm^{-1} assigned to lignin HG; (I) the band 1277 cm^{-1} specific of G lignin; (J) the band at 1060-1135 cm^{-1} assigned to cellulose and (K) the band between 360-400 cm^{-1} corresponding mostly to cellulose and hemicellulose. The step size of the chemical images is 1 µm.

The images taken from plants grown with silicic acid supplementation showed patterns of chemical distribution similar to plants starved for silicic acid (Figure 5.4). In these cases, the SEM images not only provided additional detail to see the plant structures but also the distribution of silicon was obtained by EDX (Figure 5.4C). Nevertheless, some bundle sheath cells collapsed during the SEM imaging (Figure 5.4D). Chemical maps obtained by plotting the expected silica bands did not provide contrast consistent with the silica distribution obtained by EDX. This could be explained by the relative low silica amounts deposited in sorghum leaves combined with the very weak Raman scattering character of silica and the presence of hemicellulose bands at similar Raman shifts that act as interferents probably masking the silica Raman signals. High intensity of the band 1490 cm^{-1} that can be assigned to C=C skeletal and C-N stretching vibration of aromatic compound or proteins was observed in the cell walls of bundle sheet cells (Figure 5.4G).

5.3.2. FTIR band imaging

The FTIR chemical maps (Figure 5.5E-L) have a lower spatial resolution than the Raman counterparts, especially considering that pixel resolution was improved through oversampling with an aperture of 12 μm and a step size of 3 μm. This resulted in a single cell resolution of the FTIR images in comparison with the subcellular resolution of the Raman maps. The advantage here is the possibility of mapping bigger areas as the whole middle veins instead of just a part of it. Therefore, the chemical images show here the distribution of specific compounds in the whole vein. Plotting the band at 1700-1760 cm^{-1} provided a visualization of the lignin (Figure 5.5D). The images created plotting the bands 1600-1700 cm^{-1} (Figure 5.5E) assigned to Amide I and 1480-1550 cm^{-1} (Figure 5.5F) assigned to Amide II showed protein distribution. The high intensity of these bands in chlorenchyma and bundle sheet indicated a high protein content and correlates with the high red fluorescence observed in the images of the untreated samples (Figure 5.1A). The 1200-1270 cm^{-1} band corresponding to lignin had high intensity mostly in xylem tissues (Figure 5.5H). Whereas the sclerenchyma areas showed the highest intensity of the bands assigned to polysaccharides and hemicelluloses, 970-1140 cm^{-1} and 900-1180 cm^{-1} (Figure 5.5I, J).

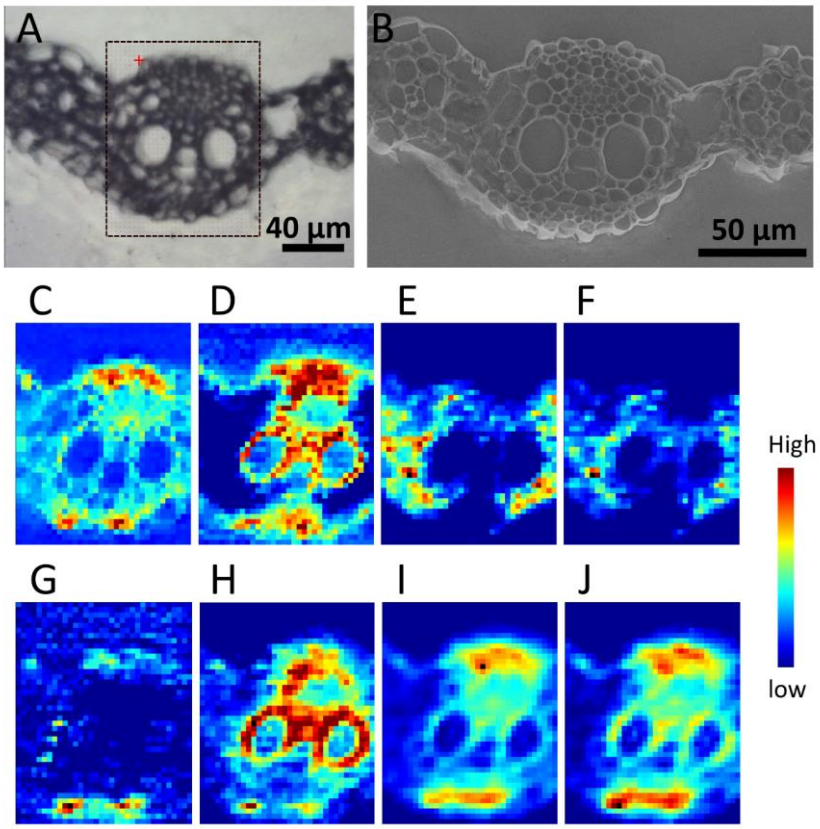

Figure 5.5: Multimodal imaging of a sorghum leaf cross-section grown in absence of silicic acid. (A) Bright-field microscopy image of a cross-section with the area analysed by FTIR spectroscopy marked. (B) SEM micrograph of the same area. Chemical images created with IR spectroscopy integrating the bands: (C) 2810-3000 cm^{-1} (CH_2) and (CH_3) stretches, unspecific to all organic matter; (D) 1700-1760 cm^{-1} assigned to lignin; (E) 1600-1700 cm^{-1} assigned to Amide I and showing protein distribution; (F) 1480-1550 cm^{-1} assigned to Amide II and ν(C=C); (G) 1280-1330 cm^{-1} (C-C), (C-O) and ν(C-H) and δ(N-H) and amide III, (H) 1200-1270 cm^{-1} characteristic of lignin, (I) 970-1140 cm^{-1} corresponding to polysaccharides and hemicelluloses, (J) 900-1180 cm^{-1} corresponding to structural carbohydrates and starch. The step size of the chemical images is 3 µm.

The same patterns were observed in the FTIR images of samples prepared from silicon supplemented and not supplemented plants (Figures 5.5 and 5.6). Chemical images showing the distribution of carbohydrates, phenolics and proteins were equivalent. In the FTIR spectra, the most prominent feature is a broad band between 950 to 1200 cm^{-1} this band is associated with carbohydrates but also contains the Si-O stretching. The

SEM-EDX silicon maps allowed to unambiguously locate the silica (Figure 5.6C). Surprisingly it was not possible to distinguish the presence of silica using FTIR regardless of the high IR absorbance of silica. Correlation of silica location with other compounds was attempted but no clear pattern could be identified. Spectra were extracted from areas containing silica confirmed by SEM-EDX, but the region 900 to 1300 cm^{-1} did not differ from the spectra taken from cell walls where silica was not present. First and second derivatives did not show differences either. This was attributed to the fact that each of the FTIR spectra was taken from a relatively big area (12 x 12 μm) while the silica deposited in very confined areas. This, together with the low silica concentration of sorghum leaves may have resulted in averaging out the characteristic silica signals. Some chemical images overlapped silica distribution, including lignin, band at 1700-1760 cm^{-1} (Figure 5.6E) and 1280-1330 cm^{-1} (Figure 5.6H), polysaccharides and hemicelluloses, bands at 970-1140 cm^{-1} (Figure 5.6J), and polysaccharides and hemicelluloses, band at 900-1180 cm^{-1} (Figure 5.6K). However, the high intensity was not limited to areas containing silica. But was also in areas absent of silica like the xylem in the case 2810-3000 cm^{-1} CH_2 and CH_3 (Figure 5.6D) and 900-1180 cm^{-1} polysaccharides and hemicelluloses (Figure 5.6K). The best correlation was achieved between the distribution of lignin at 1700-1760 cm^{-1} and silica. This image captures the silica cells and the epidermis that contain high concentrations of silica. Nonetheless, the xylem vessels are also visualized. This may suggest that the silica deposits together with lignin in the epidermis but not in the xylem.

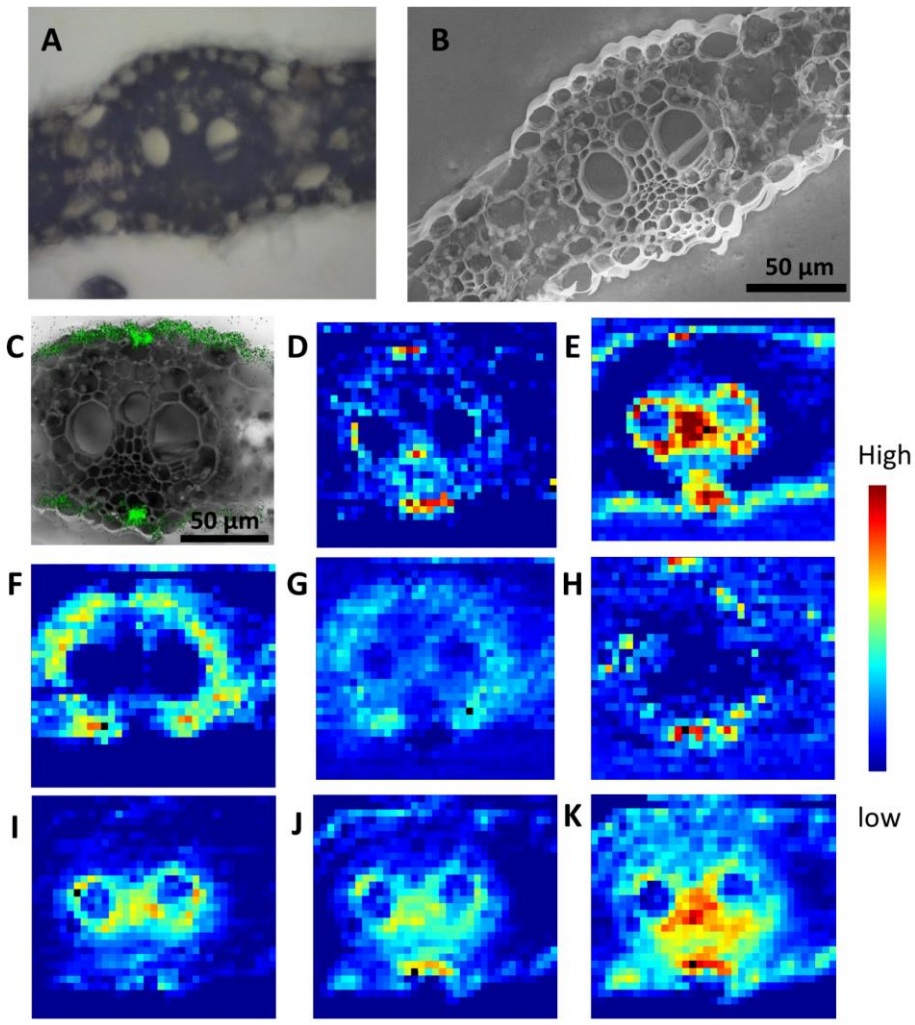

Figure 5.6: Multimodal imaging of a sorghum leaf cross-section grown with silicon supplementation. (A) Brightfield microscopy image of a cross-section with the area analysed by IR spectroscopy. (B) SEM micrograph of the same area. (C) Overlay of the Si EDX map and SEM micrograph of the area analysed by IR spectroscopy. Chemical images created with FTIR spectroscopy integrating the bands: (D) between 2810-3000 cm^{-1} (CH_2) and (CH_3) stretches, unspecific to all organic matter; (E) 1700-1760 cm^{-1} corresponding to lignin; (F) 1600-1700 cm^{-1} assigned to Amide I and showing protein distribution, (G) 1480-1550 cm^{-1} assigned to Amide II and ν(C=C); (H) 1280-1330 cm^{-1} assigned to (C-C), (C-O) and ν(C-H) and δ(N-H) and Amide III; (I) 1200-1270 cm^{-1} corresponding to (C-C), (C-O) and ν(C-H) and δ(N-H) Amide III; (J) 970 1140 cm^{-1} corresponding to polysaccharides and hemicelluloses; (K) 900-1180 cm^{-1} corresponding to structural carbohydrates and starch. The step size of the chemical images is 4 µm.

5.4. Multivariate imaging of Raman data of sorghum leaves

Chemical images obtained by multivariate methods are shown and discussed in this section. The same region shown in Figure 5.3 is shown to facilitate comparison and discussion.

PCA is a linear transformation of the data into a new coordinate system. In this new coordinate system, the largest data variance points to the direction of the first coordinate, which is also called the first principal component (PC1), the second largest variance on the second PC, and so forth. PCA can be thus considered a transformation that re-arranges the data according to the data's intrinsic variance: most of the variance is contained in the lower-order principal components while higher-order PC's are supposed to contain mainly noise. To create images using PCA, the relative contribution of each loading is plotted for each pixel. The loadings can be understood as weighting functions that correlate the original values of the variables to the new values in the reduced data set, the scores. It is possible to visualize the data after a PCA transformation in the form of an image. Instead of reconstructing images based on individual peaks and their intensity values, the images are created based on the PCs of the spectra for every pixel. In PCA images the loading contribution is plotted and allows to see the different structures. The images provide a visual representation of the information extracted. The chemical composition can be estimated by direct comparison of the loadings with the Raman spectra. The results of the PCA imaging of the same sample shown in Figure 5.3 are displayed in Figure 5.7. PC1 and PC2 showed mostly contributions of lignin. PC4 and PC5 were consistent with variations on the amount of cellulose and hemicellulose. The third PC showed features characteristic to both lignin and cellulose. The information that can be obtained by direct PCA imaging is limited as the score plot cannot be interpreted in order to differentiate between types of tissues.

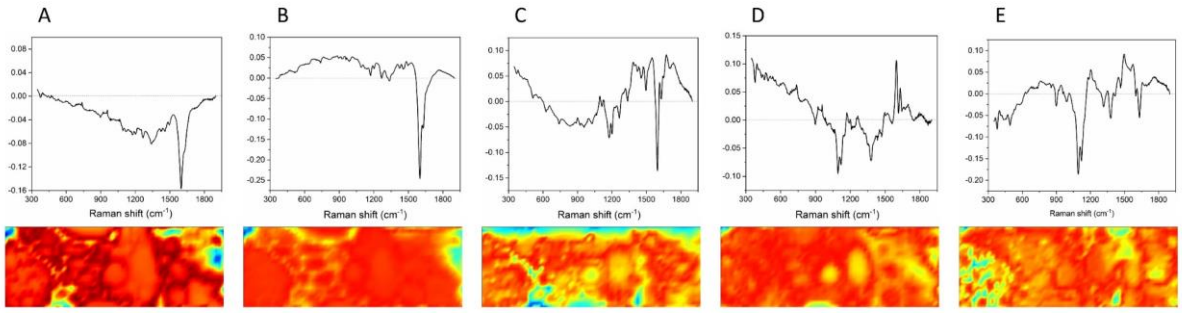

Figure 5.7: Results of the PCA of the Raman data shown in Figure 5.3. Loadings and false-coloured reconstructed images based on the score values for the PC1 (A), PC2 (B), PC3 (C), PC4 (D) and PC5 (E). High values are in red, low values in blue. PCA was carried out on baseline corrected using AsLS and vector normalized spectra in the range 360-1800 cm^{-1}.

Vertex component analysis (VCA) is a multivariate unsupervised method used to analyse hyperspectral data. The algorithm is simple, and it aims to estimate endmembers (EM's), spectral signatures of supposedly reference substances. The algorithm iteratively projects data onto a direction orthogonal to the subspace spanned by the endmembers already determined. The new endmember signature corresponds to the extreme of the projection.[194] VCA like PCA imaging allows visualizing substructures by plotting the contribution of each EM for each pixel. The endmembers are related to the spectra of the chemical components and can be directly compared. Figure 5.8A shows EMs calculated for the Raman data set shown in Figure 5.3. The EMs had recognizable features. EM1 mostly corresponded to the Raman spectra of lignin, and thus it allowed the visualization of lignin. EM3 was also consistent with a lignin-like spectrum but showed a different pattern. EM2 shows characteristic features of the cellulose spectrum (doublet at 1089 cm^{-1} and 1115 cm^{-1} and a band at 890 cm^{-1}) and high intensity in the phloem regions, consistent with the results of the chemical maps created by individual bands (compare with Figure 5.3I-K). The EM4 was background contributions.

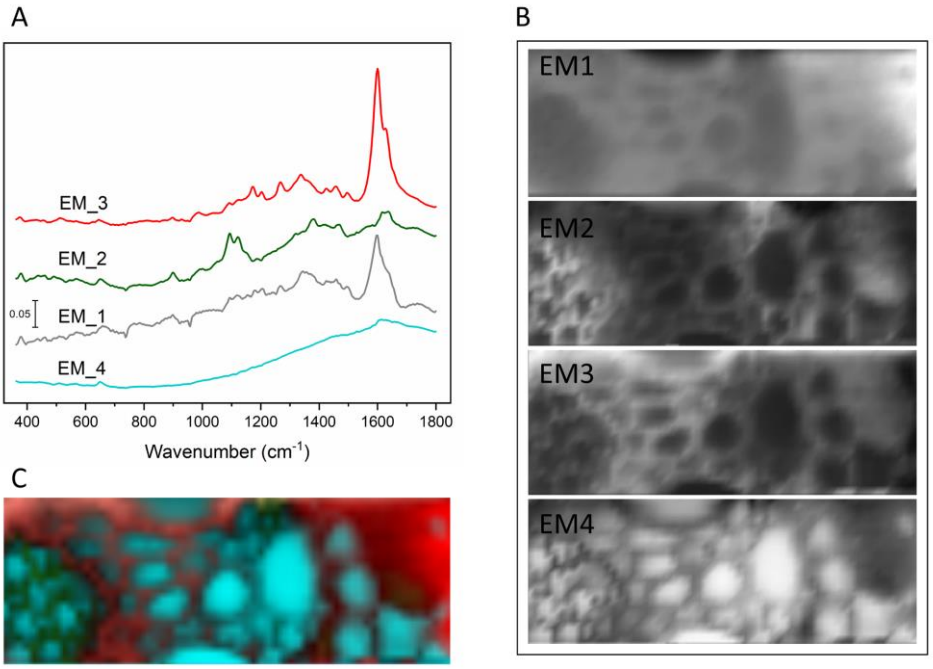

Figure 5.8: Results of the VCA of the Raman data shown in Figure 5.3. (A) Spectral signatures of the End Members (EMs). VCA was carried out on baseline corrected using AsLS and vector normalized spectra in the range 360-1800 cm^{-1}. (B) VCA imaging of the abundance fraction of each EM, white means high intensity and black lowest, and (C) Composite image created using abundance fractions of all EMs, colours of the image correspond to the colours of the spectra.

5.5. Tissue classification and chemical differences between tissue types

Hierarchical cluster analysis (HCA) of hyperspectral data is used to find similarity or dissimilarity between objects (in this case spectra) in the data set. The spectra are grouped into a hierarchical cluster tree according to the distance between them. Once the tree is created, it can be cut into the number of clusters desired and the spectra bellow each branch are assigned to a single cluster. This approach allows creating images by encoding the spectra of the same cluster using the same colour and reconstructing the hyperspectral map. HCA in combination with microspectroscopy data can discriminate and classify functional group differences existing in different plant structures.[195] HCA was used here to classify the spectra according to the types of plant tissues and then visualize the substructures. Different processing of the same data set can be used for the classification into the clustering algorithm. Namely, chemical differences are evaluated when pre-treated spectra (interpolated,

background corrected, smoothed and vector normalized spectra) are analysed using HCA. But other approaches can be used to obtain different information, for example, non-normalize spectra will be classified according to the amount of material in the sample volume, and raw spectra will be classified according to differences in the baseline, which is related to photochemical properties of the sample.

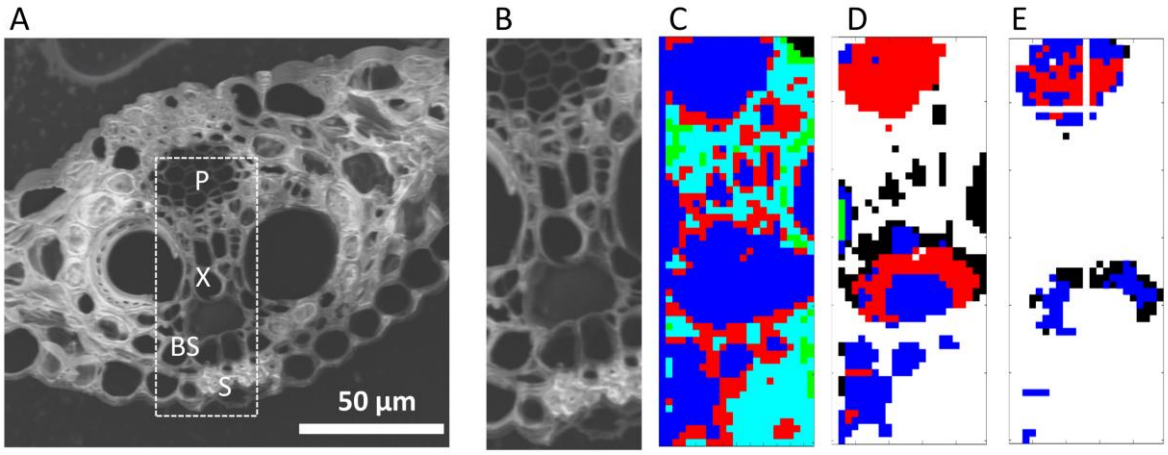

Figure 5.9: Hierarchical cluster analysis of the Raman data shown in Figure 5.3. The area contains phloem (P), xylem (X), sclerenchyma (S) and bundle sheath (BS) Raman spectra. Example of cluster-based images obtained by successive cluster analysis to select spectra from areas of interest. (A) SEM micrograph of the whole vein, the tissue types are labelled. (B) SEM magnification of the area mapped by Raman spectroscopy. (C) The first classification included all spectra. Further clustering classification was performed within these clusters, aiming to separate the spectra of a single cluster to different tissues. In (D), Phloem and xylem are still classified in the same cluster (red colour) which is an indication of the great similarities in cell wall composition between these regions. (E) Further clustering classification was needed to extract phloem spectra (red area). HCA was carried out on raw spectra, baseline corrected using AsLS or baseline corrected using AsLS and vector normalized spectra depending on the tissue selected, but all in the spectral range 360-1800 cm^{-1}.

By combining high-resolution SEM micrographs with HCA of Raman hyperspectral it was possible to cluster the spectra according to the histological structures and organs in the plant leaf (cuticle, epidermis, phloem, xylem, protoxylem and sclerenchyma tissues). When the spectra were meaningfully classified according to the tissue type, a much more powerful approach was implemented, by taking advantage of the ability of HCA to classify spectra and then using these defined classes in combination with

Principal component analysis (PCA). Classification between epidermis, vascular tissue and ground tissue was easy as there are pronounced chemical variations between these tissues. However, the classification between types of vascular tissues became challenging due to their similar composition. Implementation of sequential clustering and sub clustering proved to be a more successful approach than increasing the number of clusters in a single analysis. Figure 5.9 shows an example of a sequential clustering. In the first classification, all spectra were included (Figure 5.9C). In Figure 5.9C-E spectra from a specific cluster were classified again into several clusters.

5.6. Evaluation of the chemical differences between tissue systems by multivariate analysis

The scores plot of PCA after the classes were defined, allowed to discriminate these classes. Spectra were then interpreted by their direct comparison to the loadings. A very important advantage of this approach was that it allowed to analyse several data sets. Several examples are shown in this section. After an iterative classification of pre-processed spectra, it was possible to extract spectra from specific regions and apply multivariate analysis (in this case PCA) to evaluate the chemical differences between these tissues.

5.6.1. Chemical differences between the epidermis and sclerenchyma

Clear discrimination between plant tissue systems, epidermis and sclerenchyma, was achieved. The epidermis showed a clearly different composition that included ligno-cellulosic materials with also great influence of aliphatic compounds. Figure 5.10 shows the results of the PCA analysis of spectra taken from sclerenchyma and cuticle (outer part of the epidermis). The PCA scores plot showed a clear separation between these tissues (Figure 5.10A). PC1 showed that the separation was based on the amount of aliphatic compounds or lipids, bands at 1058 cm^{-1}, 1127 cm^{-1}, 1290 cm^{-1} and 1438 cm^{-1} and carotenoids, the band at 1525 cm^{-1} (Figure 5.10B). Both chemical groups were more abundant in the cuticle than in the sclerenchyma. In addition, variation in lignin composition contributed to the separation (1335 cm^{-1} and 1591 cm^{-1}). PC2 did not contribute to the separation but rather shows a dispersion of the data between the

classes strongly influenced by the types of lignin (1332 cm^{-1}, 1598 cm^{-1}, 1610 cm^{-1} and 1626 cm^{-1}).

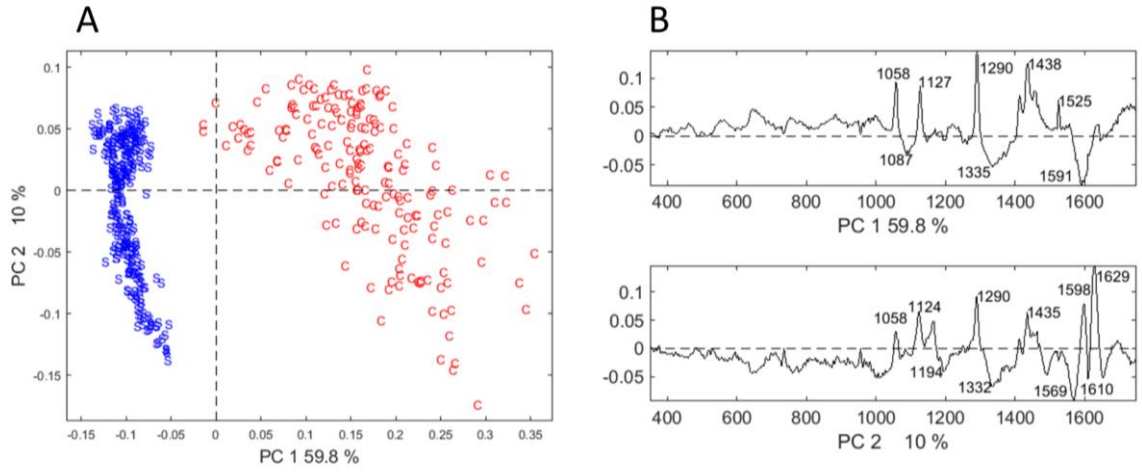

Figure 5.10: Results of the PCA of selected spectra from epidermis and sclerenchyma tissues. A clear separation was achieved in the score plot along PC1 (A) which contains 58,9 % of the variance. The chemical differences between these tissues can be further understood by examination of the loadings (B) and direct comparison with spectra.

5.6.2. A high concentration of waxes is found in the epidermis and cork cells

The epidermis spectra were dominated by features corresponding to the presence of lipids. A special type of epidermal cells with very high lipid content were cork cells. The cork cells have a tight connection with bilobate silica cells.[56] The number and distribution of the silica-cork cells pairs are diagnostic for Gramineae.[196] Both cells, which are located along the veins, originate from a common mother cell, and later are differentiated.[196, 197] During the elongation of leaves, the bilobate silica cells acquire their characteristic shape and then accumulate silica,[163] while the cork cells accumulate waxes. In longitudinal sections of mature stages of development, they are very easy to distinguish. However, in the early stages of development they are very similar and in transverse cross-sections can hardly be differentiated.[163] The role of the cork cells in relation to silica cells remains yet unclear. In general, they present pit connections and their cytoplasm cells are tightly connected.[56] It has been suggested than cork cells may be associated to the metabolism of silica cells and that the silica cells may be involved in the cuticular wax deposition by providing localized cooling of waxes after extrusion

on the surface.[196] However, the results presented by Jenks and co-workers[197] contradict this hypothesis as cork cells were still able to produce normal wax filaments when they were spatially isolated from silica cells. In sorghum leaf cross-sections, it was very difficult to distinguish between them by visual observation. However, in the Raman maps, the silica cells showed a signature indistinguishable from the rest of the epidermis (silica was undetectable using vibrational spectroscopy and only could be visualized by SEM EDX, see Figure 5.4), while the cork cells had a very specific Raman signature and could be very easily identified (Figure 5.11). The cork cells formed a defined cluster after HCA, and the average spectra of the cluster confirmed the almost exclusive composition of lipids (Figure 5.11B, C) such as cutin and suberin which are abundant in sorghum.[99, 198]

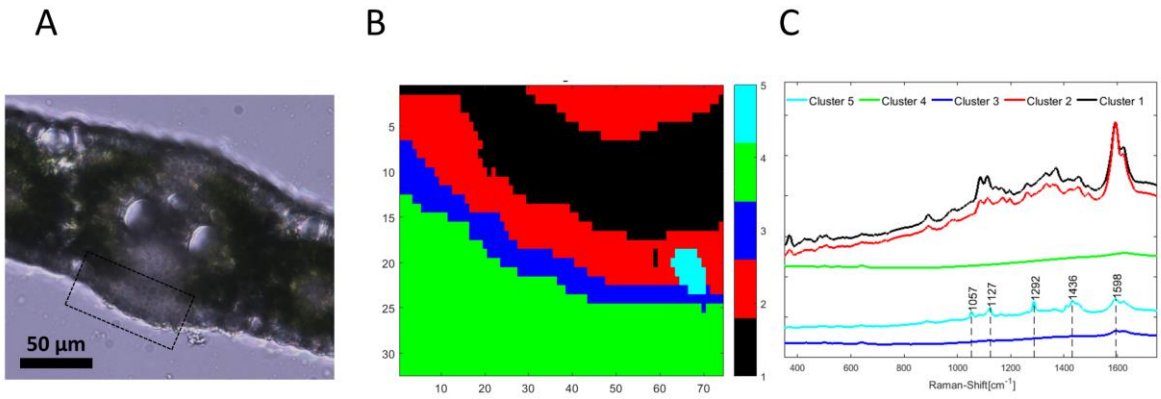

Figure 5.11: HCA of a Raman map containing sclerenchyma, epidermis and a cork cell. (A) Brightfield microscopy image. (B) HCA of the region marked in panel A, scales in x and y are different. (C) Average spectra of the clusters shown in B. Cluster 5 in light blue showed lipids as major components and most probably indicates the presence of a cork cell.

5.6.3. Chemical differences between xylem, phloem, and bundle sheath

Vascular tissues are complex conducting tissues whose main components are xylem and phloem. These tissues transport fluids that carry water, minerals and nutrients, and are surrounded by bundle sheath cells. Xylem transports to stems and leaves water and nutrients extracted from the soil solution by roots. Phloem transports the soluble organic compounds synthesized by photosynthesis, like the sugar sucrose, to the plant parts not capable of photosynthesis. Spectra from xylem, phloem and bundle sheath were selected by HCA and then analysed using PCA. During classification, phloem

and some cells of xylem showed great similarity and made their complete separation impossible in the PCA scores plot (Figure 5.9C, D). In the PCA score plot, it was possible to discriminate between spectra from the vascular tissues: phloem (P) xylem (X) and the bundle sheath (B) (Figure 5.12). Spectra assigned to the xylem (X in Figure 5.12) showed the highest variability. This can be a consequence of the existence of metaxylem and protoxylem, which were considered together for the analysis, but probably have slightly different chemical composition. Phloem and bundle sheath spectra were better discriminated.

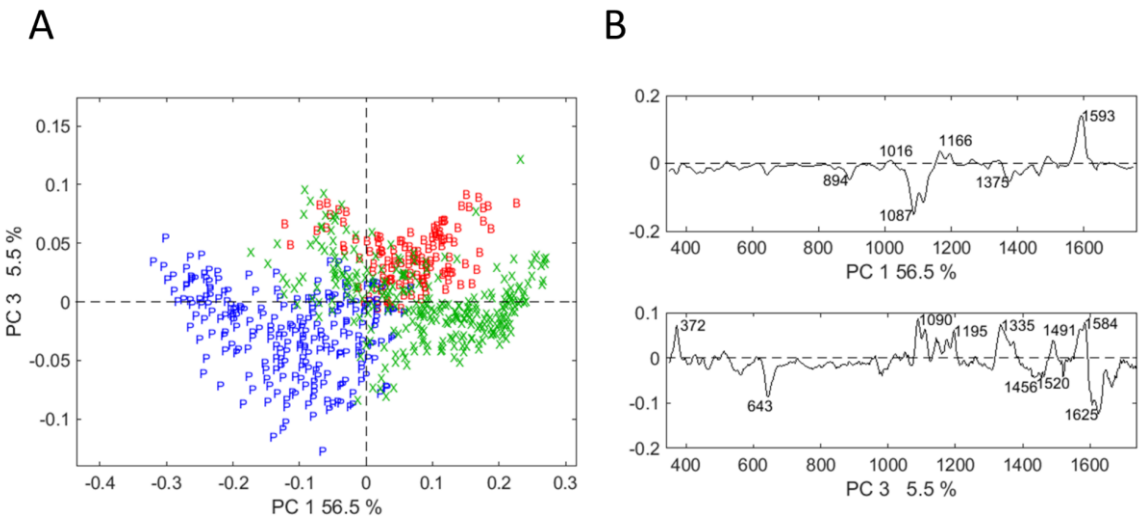

Figure 5.12: PCA results of the vascular tissue comparison after the cluster selection. (A) Scores plot in which separation according to the tissue (xylem- X, phloem- P and bundle sheath- B) was achieved. (B) PC1 and PC3 loadings indicating bands responsible for the separation.

The chemical differences between tissues can be further understood by looking at the PCA loadings. PC1 showed a higher amount of cellulose in phloem cells in comparison with the other tissues. PC1 also shows a high influence of the band at 1593 cm^{-1} assigned to lignin. This can be interpreted as a different lignin composition between the tissues. PC3 that separates bundle sheath from phloem and xylem was influenced by the band at 1335 cm^{-1} associated with sinapyl units and the 1625 cm^{-1} band, confirming differences in the type of lignin. The band at 1490 cm^{-1} also contributed to the separation, being more intense in the bundle sheath than in the other tissues. The bands 372 cm^{-1} and 643 cm^{-1} also influenced the separation along PC3. The former showed high intensity for bundle sheath and it is also associated with sinapyl units,

supporting also a higher proportion of S lignin units in the bundle sheath than in phloem and xylem. The latter is also a lignin band absent in Bundle sheath but intense in xylem and phloem. These findings could also be inferred by analysis of the average spectra (Figure 5.2A) nevertheless PCA provides a more reliable, easier and clear visualization.

5.6.4. Tissue comparison by silicon treatments

The main objective of this thesis was to understand silicification in sorghum, this comprises not only the mechanisms of silica deposition but also the effects that silicon can have on the different tissues at the cellular level as well as their specific function. With this purpose, Raman maps of samples supplemented (+Si) and non-supplemented (-Si) with silicon were obtained and compared. As have been shown in the previous section, the plant tissues differ greatly in morphology and chemical composition. Therefore, it makes sense to compare specific tissues in +Si and -Si samples.

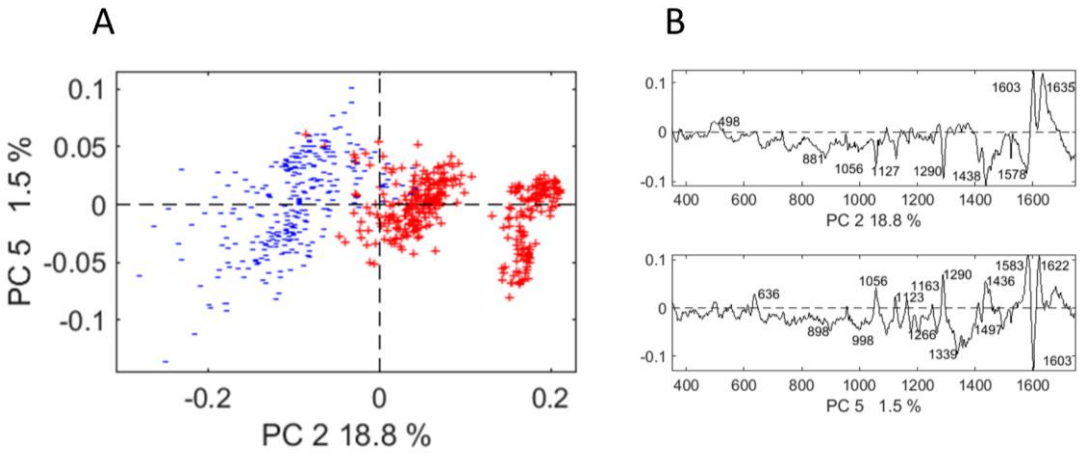

Figure 5.13: Results of the PCA of epidermis spectra selected from four maps, 2 maps for +Si and 2 maps for –Si samples. (A) Discrimination between treatments was obtained in PC2 shown in the scores plot. (B) PC2 and PC5 loadings indicating bands responsible for the separation. The PC2 loadings indicate a different lignin composition and higher amount of lipids (bands at 1127 cm^{-1}, 1290 cm^{-1} and 1438 cm^{-1}) in -Si samples than in samples supplemented with silicon.

When analysing the cell walls of sclerenchyma tissues from + Si and -Si samples, it was observed that the variability within treatments was greater than the variability

between treatments (+/- Si). Similar results were observed in xylem and phloem tissues. Therefore, it can be concluded that silicon supplementation or deprivation does not have a clear effect on the chemical composition of these tissues.

Raman spectra of the epidermis showed separation in the PCA scores plot according to the silicon treatments (Figure 5.13). The silicon supplemented samples appeared at positive values, which correlates with high intensity of the bands at 1603 cm^{-1} and 1635 cm^{-1}, indicating differences in the lignin composition. Silicon supplemented samples also showed the high intensity of the band at 498 cm^{-1}. In principle, one could think that this last band is the contribution of the silica, as it appears at more intense in the + Si treatments and silica is mainly deposited in the epidermis. Nevertheless, it appears at a higher frequency than the bending Si-O band is expected (498 cm^{-1} rather than 478 cm^{-1}) and it cuts abruptly at lower frequencies instead of the characteristic wide shape expected for the silica signal. Therefore, it seems more appropriate to assign this band to differences in hemicelluloses instead of silica itself.

The information obtained by FTIR was more limited. The spatial resolution of the IR spectral maps was lower in comparison with the Raman spectral maps. The big areas sampled averaged many cells in comparison with the Raman in which much smaller spot sizes were measured. This implies that many of the single spectra contain more than a single tissue, and thus the potential to classify and compare tissues was lower. Additionally, FTIR spectra suffered from scattering effects (Mie scattering) due to the similar size of the tissue features and the IR wavelength. This effect was especially noticeable for the spectra taken from the epidermis. This results in many distorted spectra that acted as outliers. Mathematical treatments were applied in order to correct this scattering effect, namely EMSC. But the process is time consuming and requires vast computational resources for the optimization. It was possible to discriminate between silicon treatments using IR spectra taken from sclerenchyma. The separation was based on the bands between 1500 to 1700 cm^{-1} assigned to lignin and proteins. This was not observed in the Raman spectra analysis.

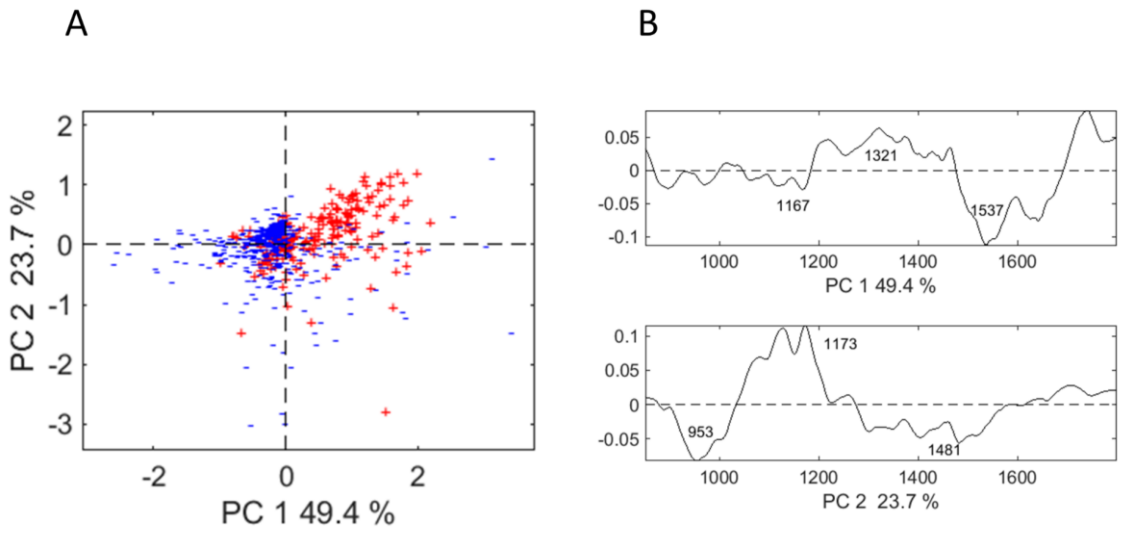

Figure 5.14: Results of the PCA analysis of spectra classified as sclerenchyma after EMSC correction. (A) Scores plot shows the separation between silicon treatments. 5 maps of +Si treatment and 5 maps of -Si were included in the analysis. (B) PC1 and PC2 loadings indicating bands responsible for the separation. The PC1 loading indicates differences in the bands between 1500 to 1700 cm^{-1}, assigned to lignin and proteins.

5.7. Evaluation of the laser-induced fluorescence

As mentioned before, the versatility and potential of HCA classification does not need to be limited to the preprocessed spectra and can be directly applied to other data such as raw, or partially pre-processed spectra. If so, the classification includes information on the sample in addition to pure chemical variations. HCA of the raw spectra leads to classification based on the overall intensity of the Raman signal. The baseline in a Raman spectrum is the consequence of the optical intensity generated by the sample, usually unwanted and eliminated through pre-processing of the spectra. The most important optical intensities generated by the sample are fluorescence and blackbody radiation. Which can vary from zero to several orders of magnitude greater than the analyte signal.[199]

Raman spectra obtained from sclerenchyma tissue were selected by the HCA approach described before. After the first classification, the interpolated spectra without any

further pre-processing were further classified using HCA. This resulted in a second classification of the spectra from a specific tissue (sclerenchyma), based mainly on changes in the baseline, that here are attributed to the sample fluorescence. Three clusters were created, showing high, medium and low-to-non-fluorescence, of which the two extremes, high and low, were analysed using PCA. As the classes of spectra were defined by the HCA (high and no fluorescence), applying PCA allowed to evaluate spectral differences between correlated with fluorescence.

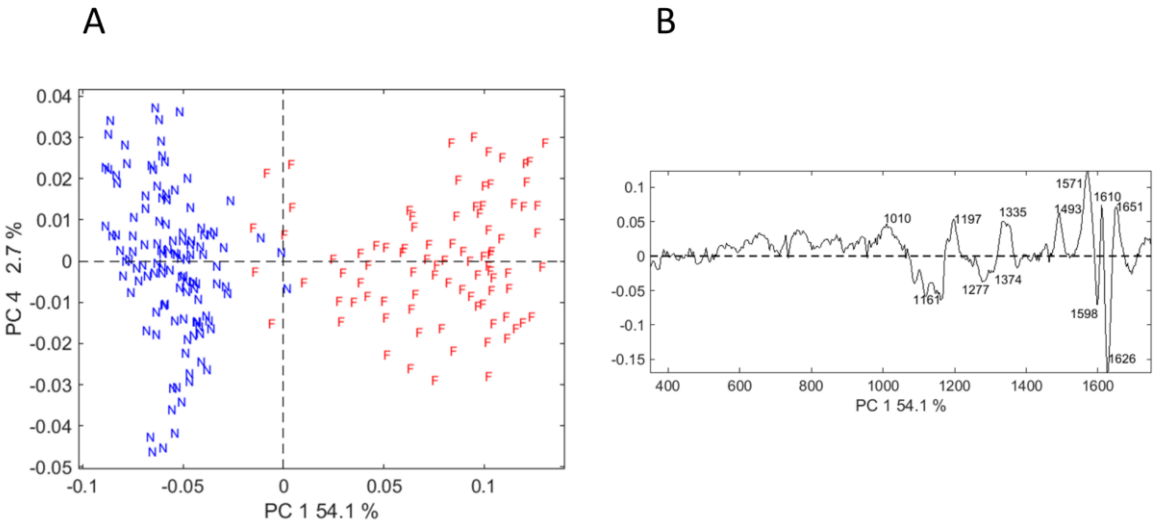

Figure 5.15: PCA results of the of the sclerenchyma spectra classified as high fluorescence (F) and low to non-fluorescence (N). (A) PCA scores plot achieved clear separation. (B) PCA1 loading, the bands 1010 cm^{-1}, 1197 cm^{-1} (CH bending), 1335 cm^{-1} (Lignin S units), 1360 cm^{-1} (ring mode in biphenyl), 1493 cm^{-1}, 1571 cm^{-1} (lignin radicals), 1610 cm^{-1} (out of phase ring more in biphenyl), 1651 cm^{-1} (ferulic acid), 1090 cm^{-1} (cellulose), 1161 cm^{-1}, 1277 cm^{-1} (lignin, G units), 1374 cm^{-1} (lignin, G units), 1598 cm^{-1}, 1626 cm^{-1} (aldehydes in lignin) and 1694 cm^{-1} influenced the separation.

An effective separation was achieved in the scores plot between spectra with high fluorescence (F) and low-to-non-fluorescence (N), with 54.1 % of the variance explained in PC1 (Figure 5.15A, B). The loading vector can be directly used to evaluate chemical differences. Spectra with high influence of fluorescence showed higher intensity of the bands (or positive values in the loadings of the variables): 1010 cm^{-1}, 1197 cm^{-1} (CH bending in dibenzodioxocin lignin), 1335 cm^{-1} (S units), 1360 cm^{-1} (ring mode in biphenyl), 1493 cm^{-1}, 1571 cm^{-1} (lignin radicals), 1610 cm^{-1} (out of phase ring mode in biphenyl), and 1651 cm^{-1} (ferulic acid) whereas the spectra with no

fluorescence showed high intensity (or negative values in the loadings of the variables) 1090 cm^{-1} (cellulose), 1161 cm^{-1}, 1277 cm^{-1} (lignin, G units), 1374 cm^{-1} (lignin, G units), 1598 cm^{-1}, 1626 cm^{-1} (aldehydes in lignin) and 1694 cm^{-1} (carbonyl and ester bonds). The band at 1493 cm^{-1} could be assigned to either C=C skeletal vibrations of aromatic compounds, possibly in lignin, or C-N stretching vibration in proteins. This band appeared in sclerenchyma spectra but was also very intense in the spectra of cell walls of bundle sheath cells (Figures 5.2A and 5.4G). The contribution of some unidentified cell wall protein to the fluorescence observed cannot be excluded.

5.7.1. Lignin autofluorescence and structure

The average spectra of the groups defined as high and low-to-non-fluorescence are displayed in Figure 5.16A. The 1550-1750 cm^{-1} region (Figure 5.16B) is the most characteristic and informative region of the Raman spectrum of lignin contributions as aromatic rings, ethylenic C=C, α- and γ- C=O are detected here.[173] With the maximum around 1600 cm^{-1}, that is not a single band but combined several scattering bands representing a variety of molecular species. This can be accounted for the loadings in Figure 5.15B. The spectra are not offset, and the influence of the baseline is visible. The slope of the baseline was clearly more pronounced in the top spectra as it was the overall absolute Raman signal.

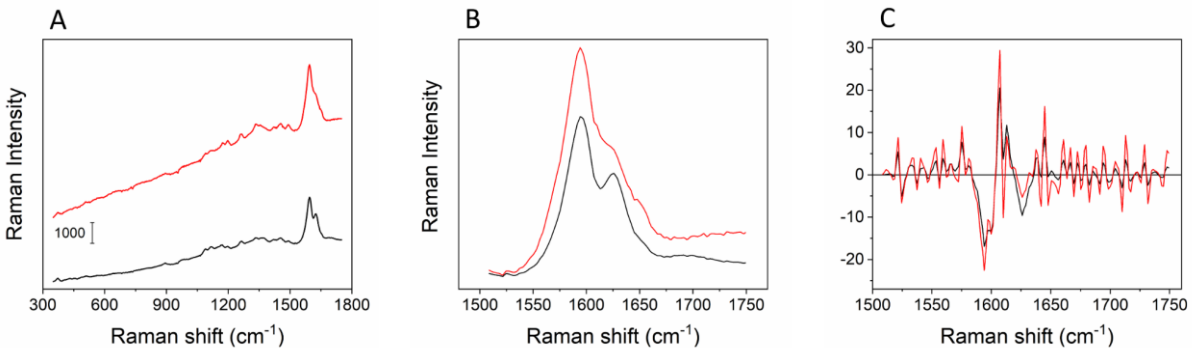

Figure 5.16: Average spectra and the second derivative of spectra classified as high fluorescence and non-fluorescence. (A) Average spectra of clustering analysis of interpolated spectra from sclerenchyma of sorghum leaves without further pre-processing. The classification obtained is based on baseline differences. (B) Magnification of the region 1500-1750 cm^{-1}. (C) The second derivative of the spectra in the region 1500-1750 cm^{-1}.

Figure 5.16C shows the second derivative of average spectra the range 1500-1750 cm^{-1} after HCA of non preprocessed Raman spectra taken from sclerenchyma. Calculation of the second derivative of Raman spectra is the most straightforward and robust background suppression method.[200] The minima detected at 1594, 1610, 1624 and 1648 cm^{-1} corresponded to inflection points and could be used to identify hidden bands. The minima of the second derivative showed also to be consistent with positive and negative maxima in the PCA loadings (Figure 5.15B).

5.7.2. Deconvolution of the lignin bands

Deconvolution analysis of the bands between 1500 to 1750 cm^{-1} was attempted. The initial positions of the bands used for fitting were determined from the minima in the second derivative spectra and the most influencing bands on the PC1 loading, whose Raman shift positions were consistent. Nevertheless, band positions were optimized by the fitting algorithm (Table 5.3). Interestingly, the fitting of the high fluorescence spectrum converged only when a band at 1613 cm^{-1} was considered. In contrast, in the low fluorescence spectra, this band had to be excluded for the model to converge (Figure 5.17). The best fittings were obtained by using gaussian shape bands.

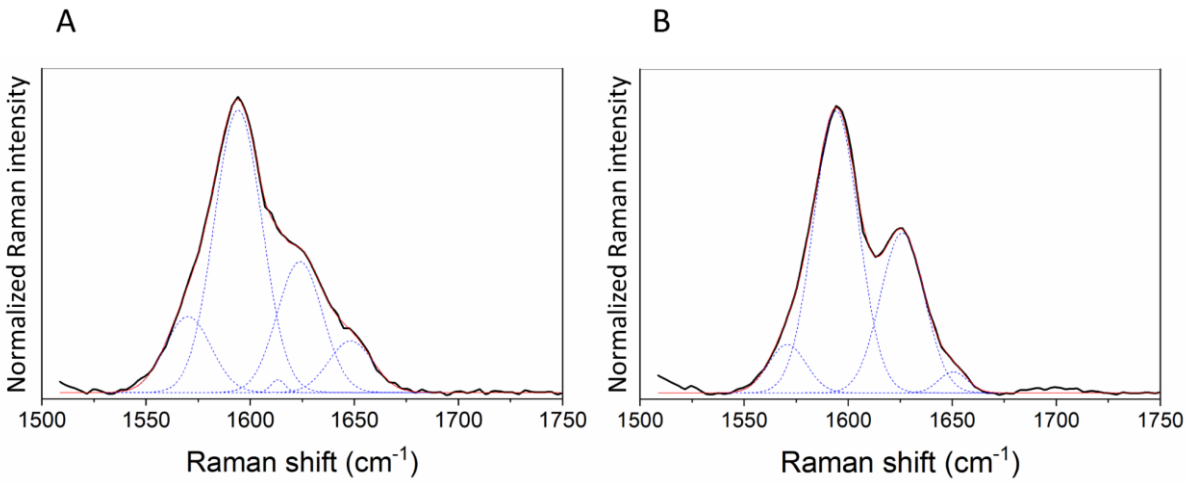

Figure 5.17: Deconvolution analysis of the lignin band. The best deconvolution fitting was obtained for 1500 to 1750 cm^{-1} range for the fluorescence (A) and non-fluorescence (B) average spectra.

Table 5.3: Summary results of the best deconvolution fitting obtained for 1500 to 1750 cm^{-1} range for the fluorescence and non-fluorescence average spectra.

High fluorescence			No fluorescence		
Raman shift/cm^{-1}	**Area /%**	**Fitting**	**Raman shift/cm^{-1}**	**Area/%**	**Fitting**
1570	13.8	Gaussian	1570	8.2	Gaussian
1594	53.2	Gaussian	1594	57.3	Gaussian
1613	0.7	Gaussian	1613	Absent	
1624	23.4	Gaussian	1624	31.7	Gaussian
1648	8.9	Gaussian	1648	2.7	Gaussian

5.7.3. Relationship between the laser induced fluorescence and the Raman spectra due to lignin bond types and structure

In an attempt to correlate specific chemical composition of the lignin with the exhibited fluorescence, detail analysis of the aromatic stretch bands was performed. The fluorescence properties of lignins are related not only to chemical composition but also to the diverse molecular structures of lignin. An increase on the fluorescence intensity was reported upon removal of carbonyl groups by reduction with borohydride.[201] The presence of specific structures such as phenylcoumarone and stilbenes has also reported being responsible for a strong fluorescence.[201] The autofluorescence properties of lignocellulosic materials are described in the literature.[202, 203] Autofluorescence of cell walls has been observed at various wavelengths, but laser-induced autofluorescence of lignin is especially intense when using Raman spectroscopy at the excitation wavelength of 532 nm.[204] Early Raman spectroscopy studies of plant cell walls already reported laser-induced fluorescence as problematic and responsible for masking the Raman signals.[104] Despite the fluorescence observed when using excitation wavelength at 532 nm, it is interesting to use this wavelength over lasers at 633 nm and 785 nm when the autofluorescence does not mask the Raman signals. This is due to three main reasons: (I) an improved lateral resolution, (II) the higher scattering at shorter wavelengths, and (III) the possibility of using resonance effects increasing drastically the intensity of some bands.

Clear differences in the lignin band in the range 1500 cm^{-1} to 1750 cm^{-1} were found between the average spectra of the high fluorescence and low-to-non-fluorescence

spectral groups. The resonance or pre-resonance effects of the lignin bands in this region correspond to the C=O and C=C stretching vibrations. Resonance makes any type of quantification unattainable and even more complicated in the lignin system. The conjugation of C=O double bonds to aromatic rings increases their Raman scattering intensity. This increase is the consequence of delocalized molecular orbitals caused by overlapping of adjacent atomic orbitals. Pre-resonance and resonance Raman scattering, that occurs when a sample compound has an absorption band close to the excitation wavelength also increases drastically the Raman intensity. This enhancing effect can increase the Raman scattering intensity by as much as a million times.[89] Nevertheless, the π-electron conjugation between the phenyl ring and its substituents is the main factor affecting the intensity of the aromatic band at 1600 cm ^{1}. The presence of conjugated structures and pre-resonance effects in lignin has implications on quantitative work because specific conjugated structures contribute disproportionately to band intensity. Apart from the close connection of the lignin components and the lignin composition and structure, the spectra allow quantitative discussion. The band's areas in the region 1550 cm^{-1} to 1750 cm^{-1} showed different proportions. Especially the band at 1613 cm^{-1} absent in the spectra with low-to-non fluorescence. This band has been reported to arise from biphenyl out-of-phase ring vibrations in dibenzodioxocin.[146] Bands at 1197 cm^{-1} and 1360 cm^{-1} are also assigned to biphenolic structures.[146] Planar biphenyl rings result from 5-5′ coupling of monolignols, instead of the most abundant ß-O-4 or ß-ß bonds (Figure 5.18). Indeed, Lähdetie and coworkers attempted to clarify correlations between the laser-induced fluorescence and the lignin structure performed by Raman spectroscopy.[204] They concluded that the presence of free phenolic structures was not a prerequisite for the induced fluorescence. Instead, the bond types seem to have a strong influence in the intensity of the fluorescence in lignin model compounds and specially the 5-5′ structures via the conjugation system over the two aromatic rings.

Due to the inherent complexity of the lignin polymer, the interpretation of the bands needs to be taken carefully. Despite the particular lignin structure and composition, the maximum appears always at around 1600 cm^{-1}. A study of 40 molecular models of lignin showed that the intensity of this band is very sensitive to the selected model and

substituents on the aromatic ring. However, in the majority of the models, the vibrational frequency was confined between 1594 to 1603 cm^{-1}.[170]

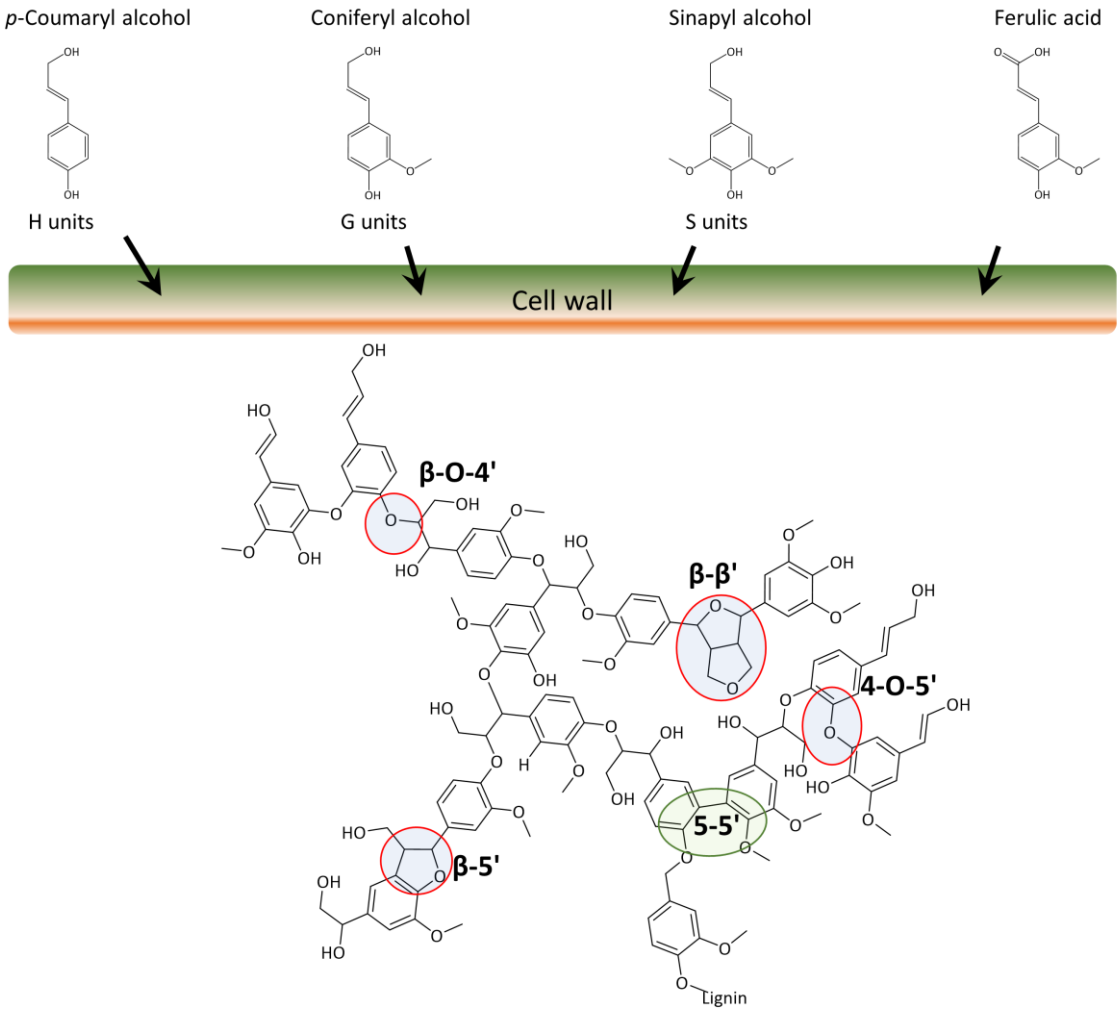

Figure 5.18: Scheme of lignin formation. Canonical monolignols are incorporated into the polymer through different types of bonds marked in the lignin structure by circles. The 5′-5′ bond-forming biphenyl structure is surrounded by a green circle. This structure leads to laser-induced fluorescence.

The shoulder at 1570 cm^{-1} is assigned to lignin radicals[187] that are intermediates during lignin biosynthesis. This shoulder is not present in all lignins but is characteristic to dry wood,[187] and DHPs (also see Figure 7.1). The second most intense band of the

Raman spectra appears at 1624 cm^{-1} and is commonly associated in the literature with C=C stretch of coniferaldehyde.[169] Apart from the strong vibration, the band contains several more vibrations.

Laser induced fluorescence (LIF) of lignin is also greatly influenced by the conformation of the aromatic rings in the lignin structure. Flexible conformations have shown higher intensities of fluorescence than structurally rigid models.[204] Therefore the hemicelluloses matrix that surrounds and crosslinks the lignin polymer may also influence the fluorescence of native lignin as it provides stiffness and limits the mobility. Synthetic lignins or DHPs, which are not embedded in a polysaccharide matrix can be highly fluorescence,[114] but also, it is appropriate here to keep in mind that DHPs have less β-O-4 and more β-β′, β-5′, and 5-5′ linkages than native lignins. A scheme of lignin formation, showing the different conformations and bond types is displayed in Figure 5.18. The data suggest that the lignin conformation, specifically, the 5-5′ linkages that produce biphenyl structures are the most influencing factor of the lignin fluorescence properties. This is also supported in the literature.[204]

5.8. Conclusions

In this chapter, a multimodal approach, comprising brightfield microscopy, fluorescence microscopy, SEM-EDX and chemical maps created from Raman and FTIR data, was used to visualize and study the composition of the different tissues in sorghum leaves grown with or without silicic acid supplementation. The microspectroscopy data were also combined with multivariate methods to produce images and to assess chemical variations between the plant tissues and structures.

All the approaches evaluated here are useful to visualize the plant structures and can help to understand plant tissue complexity. The microspectroscopic approaches, Raman and FTIR, allowed to visualize the structures and their organic components but were not sensitive to silica. Detecting and locating silica was possible by SEM EDX. Comparing these three microscopies, the best image resolution and therefore greater details were obtained by SEM, while the chemical composition and distribution was obtained by Raman and FTIR. Raman microscopy provided an easier approach in

terms of sample preparation and achieved higher lateral resolution. Combining these three analytical techniques that are complementary to each other allowed to obtain more accurate and more complete structural information.

The Raman hyperspectral maps presented here were taken from cross-sections of sorghum leaves grown with and without silicic acid supplementation. Data were analysed by several multivariate methods and imaging methods, which were compared. Among the tissues analysed, the cuticle showed the highest influence by silicon supplementation in its chemical composition. All analytical approaches provided interesting insights. However, combination (HCA+PCA) resulted in the classification of spectra and provided a unique way to compare the chemical composition of the different tissues. In sorghum roots substantial variation in cell wall autofluorescence between silica deposition sites and rest of cell walls was reported. [205] The autofluorescence was dependant on silicon supplementation/deprivation.[205] This suggests a relationship between the lignin structure and molecular composition with the silica deposition, further explored in Chapter 7. A similar observation in sorghum leaves could not be detected. These contrasting findings suggest that the relationship between silica and cell walls needs to be further explored.

The distinction between plant cell wall components is challenging. Linear spectroscopy detects everything in the beam path and the differences between cellulose and other cell wall polymers is subtle as matrix polymers have the same interatomic bonds as cellulose: C–H, C–C, C–O, and O–H. Nevertheless, by plotting specific bands it is possible to see the spatial distribution of compounds when a proper and reliable assignment of the bands is considered. It is important to notice that the wavenumbers presented here should be taken as a broad band area or range rather than a single wavenumber. This is due to the expected shifts in reference to those of isolated compounds due to the different kinds of environments and, on some occasions to the wide unresolved bands reflecting the complicated polymeric structures. It is important to keep in mind that the cell walls are made of very complex polymers.

The structural information that can be obtained from Raman spectra is more limited than other techniques such as nuclear magnetic resonance (NMR) or mass

spectrometry (MS). Nevertheless, these analytical methods require the isolation of lignin, during which the naturally existing chemical bonds in lignin and between lignin and the cell-wall polysaccharides can be affected or destroyed. In that sense, Raman spectroscopy presents a fundamental advantage as it provides a characterization of the materials in the native state with relevant spatial resolution. Raman spectroscopy provides information on specific lignin bonds and composition, and their spatial distribution in the micrometre scale. Detailed qualitative analysis of the lignin bands on the Raman spectra enabled a correlation of the molecular structure of lignin and its fluorescence properties.

Chapter 6

Nano FTIR applied to plant tissues

This chapter is partially based on the publication *Anal. Chem* **2020**, *92* (20), 13694-13701.

The plant cell wall is an interesting system to discuss in the context of plant silicification. The cell wall components can influence silica deposition. The cell wall is a complex composite structure made of polysaccharide, polyphenols, proteins, and minerals whose composition and arrangement at the nanoscale level is crucial to the tissue function.[110, 206, 207] As it has been discussed in previous chapters, the high sensitivity and the details on molecular composition and structure that vibrational spectroscopic methods provide, are useful for studies of plant materials. The infrared (IR) spectra provide detailed information on organic cell wall constituents including cellulose, phenolic compounds, and proteins.[96, 98, 208-212] Nevertheless, it is challenging to find a compromise between the high content of information of the IR spectrum and the limited spatial resolution due to the use of mid-infrared light, in particular, considering a high structural heterogeneity of both the organic and the inorganic plant tissue components at the nanoscale. In many cases, the resolution achieved by IR microspectroscopy does not go beyond a few μm whereas the plant cell structures comprise only a few nm such as crystalline cellulose fibrils with specific orientation and varying cellulose density,[213] and the layered structure of the secondary cell wall.[214] Furthermore, obtaining a vibrational spectrum of the grass silica in situ has remained a challenge to vibrational microspectroscopy due to the low intensity of the Raman silica bands and the similar vibrational frequencies of hemicellulose and arabinoxylan,[215] and usually the silica needs to be extracted before Raman analysis.[135, 155]

IR-nanospectroscopy based on a scattering-type near-field optical microscope (s-SNOM), although relatively new, has already been used successfully for a vast range

of organic synthetic and natural samples. It can be used for the elucidation of sub-molecular structure in bioorganic molecules, including proteins,[216-220] the characterization of cell wall composition of fungi, and biominerals in dentin and mussel shells.[221, 222] It has also been used in plant science to chemically characterize the intricate structure of the nano-sized pores in pit membranes in *Populus nigra* wood. The s-SNOM spectra showed characteristic peaks of cellulose, phenolic compounds, proteins and pectin.[223]

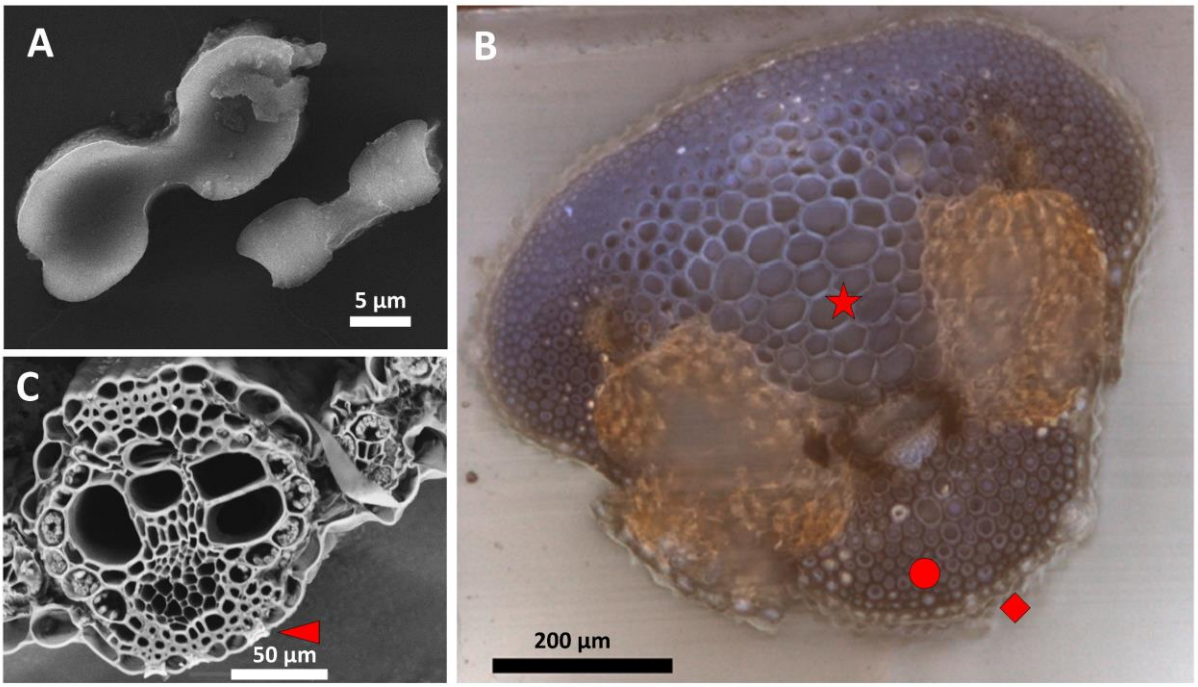

Figure 6.1. Images of samples analysed by nano IR. (A) SEM micrograph of extracted silica phytolith from sorghum (*Sorghum bicolor*). (B) Bright-field micrograph of durum wheat (*Triticum turgidum*) awn with silicified papillae (diamond) and cell walls areas analysed (circle: silicified, starlet: non-silicified) are marked. (C) SEM micrograph of a sorghum leaf cross-section, a silicified bilobate cell is marked with an arrow. Figure adapted with permission from Zancajo, V. M. R. *et al. Anal. Chem.* 2020, 92, 20, 13694–13701.

In this chapter, IR spectra obtained in different plant tissue types, at nanometre resolution, using an s-SNOM are presented. Focusing on the inorganic-organic hybrid character of plant materials, the abilities of the nano-IR spectroscopic approach are discussed. In particular, the possibility to use native, unembedded tissues as samples was investigated. The tissues analysed originate from different grass species, wheat

and sorghum, and comprise both epoxy embedded and unembedded, native leaf samples, as well as purified silica phytoliths. Three types of plant samples were evaluated by Fourier transformed infrared (FTIR) nanospectroscopy: i) extracted silica phytoliths, ii) epoxy resin embedded awns of wheat and iii) fresh untreated cross-sections of *Sorghum bicolor* leaves (Figure 6.1). Nano-IR spectroscopy provides information on the cell wall composition and on the distribution of silica in the organic structure, therefore it can be used to understand the complex process of silica deposition[5] and plant silicified structures, and the structural heterogeneity of plant cell walls.

6.1. FTIR nanospectra of isolated phytoliths

FTIR nanospectroscopy was used to study microscopic biosilica particles and the phytoliths that were extracted from plant tissue. The difference of the s-SNOM approach used here to analyse the isolated silica particles with conventional FTIR spectroscopy is that in the s-SNOM approach, the scattered light is measured, therefore both an amplitude (Figure 6.2A) and a phase spectrum (Figure 6.2B) are obtained. The maximum on the amplitude spectrum is shown at 1080 cm^{-1}, whereas the phase spectrum shows two maxima at 1127 cm^{-1} and 1260 cm^{-1} that were assigned to the Si-O asymmetric stretching mode, based on previously reported nano IR spectrum of SiO_2[125] and typical IR absorbance spectra of amorphous silica, where this vibration usually appears at 1000-1250 cm^{-1} as a very intense band.[224] By taking the imaginary part of the phase after normalization against a background signal, the nano-FTIR absorption spectrum is obtained (Figure 6.2C). The background signal is collected at a nearby clean position on the same silicon wafer where the sample is placed.

The nano-FTIR absorption spectrum of the phytoliths extracted with microwave digestion and phytoliths extracted with wet digestion were similar and showed an intense, slightly asymmetric band at 1100 cm^{-1} and a shoulder at 1260 cm^{-1} (Figure 2C). This narrow sharp signal was attributed to the strong phonon resonance of amorphous silica, SiO_2.[225] The nano-FTIR spectrum is analogous to a normal FTIR spectrum and the absorption bands can directly be compared as it has been demonstrated that the nano-FTIR spectra of a thick organic film correlate well with the bulk IR absorbance

spectrum regarding the peak positions, peak shapes and relative peak heights.[127] However, the near-field spectral response of a phonon resonance, such as the amorphous silica, can be very different from the far-field response. A spectral narrowing and sharpness have been described previously[225] and the result is a sharp resonance within the phonon band that can be singled out.[226] For crystalline quartz two near-field resonances in the close neighbourhood instead of a single one would be evident.[227] Therefore the single band was consistent with amorphous silica and again confirmed the amorphous character of the plant biosilica. The characteristic position and shape of this band can be used to identify the presence of silica *in situ* in the plant tissues.

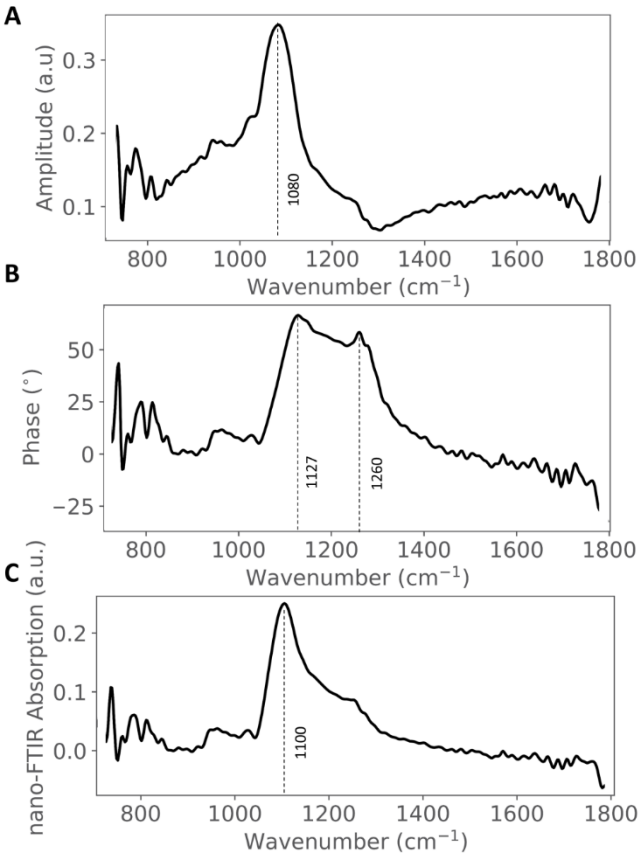

Figure 6.2: Nano-IR spectra of an extracted phytolith (sorghum biosilica). A) Amplitude spectrum. B) Phase spectrum. C) Calculated nano-FTIR absorption spectrum. Figure adapted with permission from Zancajo, V. M. R. *et al. Anal. Chem.* 2020, 92, 20, 13694–13701.

6.2. Reproducibility

Spectra from microwave extracted phytoliths from different points showed consistency regarding the position of the silica phonon resonance (Figure 6.3A). This demonstrated the reproducibility of the silica signals. To evaluate the reproducibility for weak oscillators such as organic compounds, spectra were recorded at random spots from the epoxy resin and compared. The bands' position showed to be consistent (Figure 6.3B).

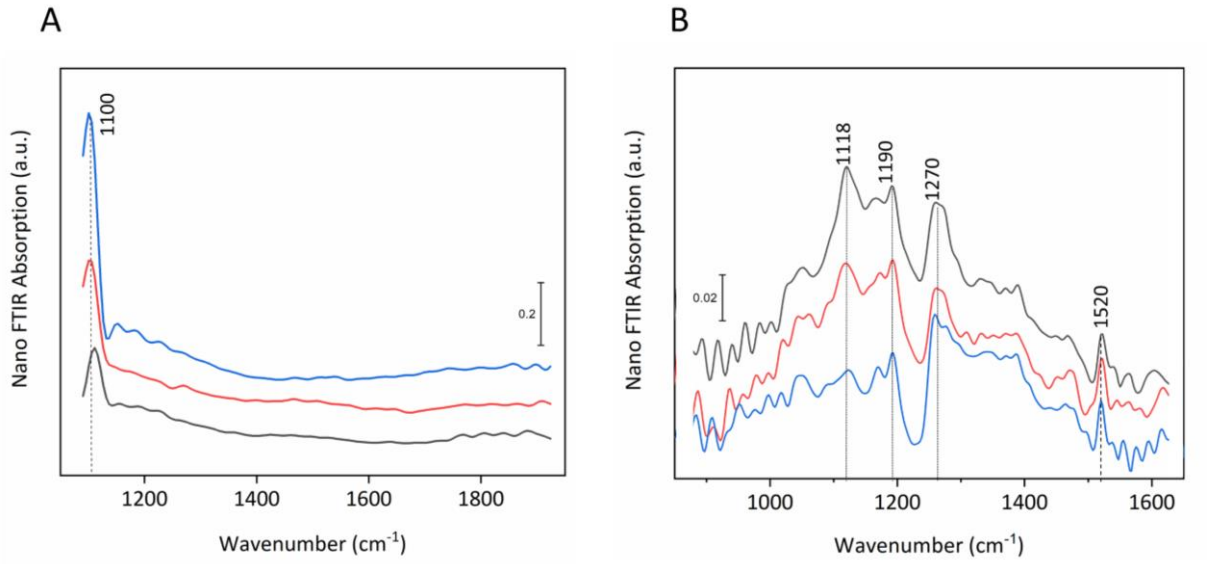

Figure 6.3: (A) Spectra from microwave extracted phytoliths from different points of the same phytolith showing the strong silica phonon resonance. Spectra are offset for clarity. (B) Spectra recorded at random spots from the epoxy resin (outside sample) used to embed the samples also are consistent in the band position this demonstrates reproducibility also for weak oscillators such organic compounds. Spectra are offset for clarity. Figure adapted with permission from Zancajo, V. M. R. *et al. Anal. Chem.* 2020, 92, 20, 13694–13701.

6.3. Silica structure of extracted phytoliths

The 3D topography images obtained by the AFM prior to the collection of the IR spectra showed the nanostructure of the extracted phytoliths and confirmed the observations described in previous reports[151] and Chapter 4 of smaller spherical particles forming the MAD extracted phytoliths of 50 to 100 nm of diameter

(Figure 6.4A, B), in comparison with the silica that was extracted by SONE formed of slightly bigger individual particles (Figure 6.4C, D).

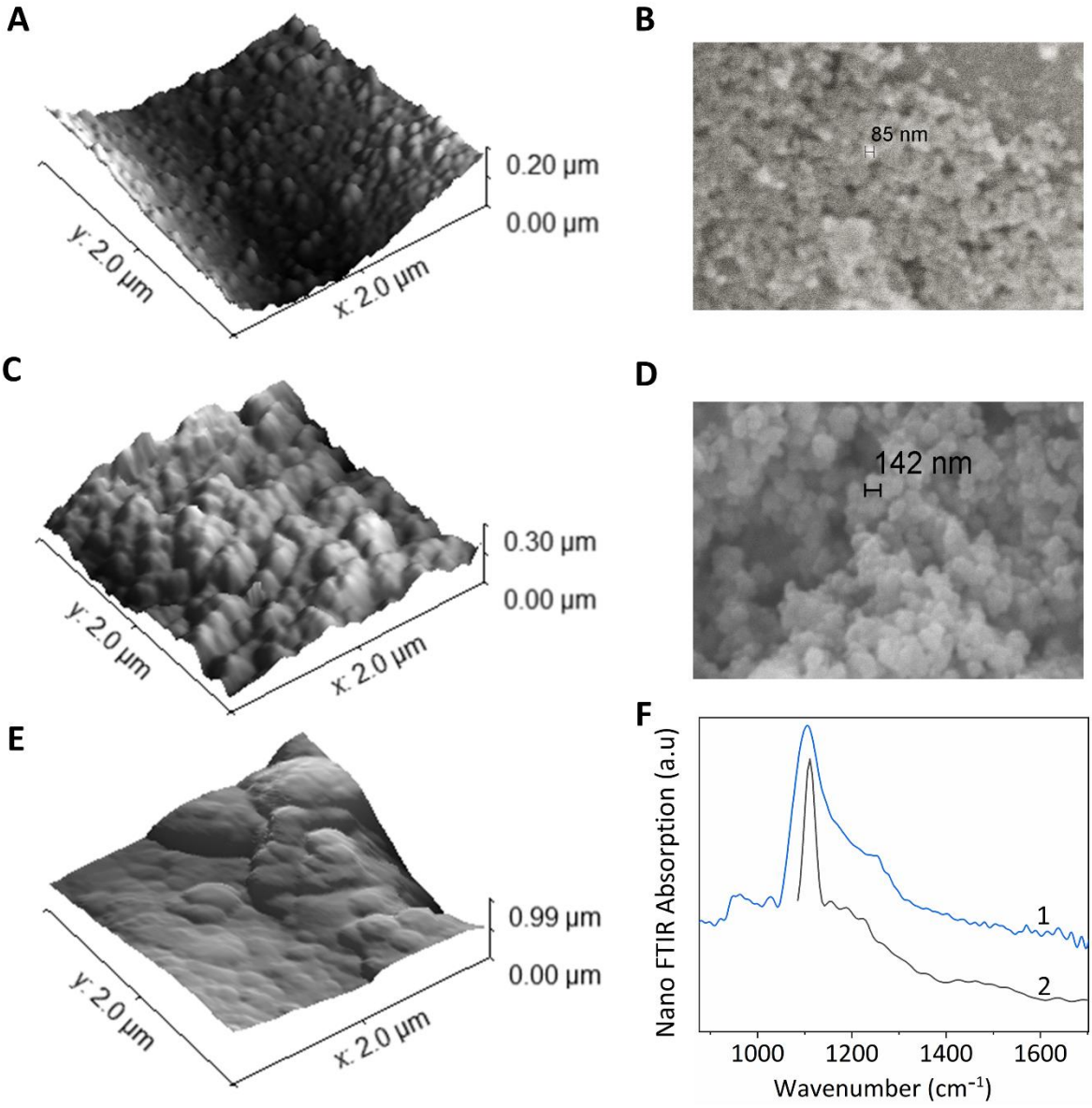

Figure 6.4: Silica structures in phytoliths of sorghum leaves. A) 3D topographic images of silica extracted by MAD showing small spherical particles. B) SEM micrograph of extracted silica by MAD digestion. C) 3D topographic images of silica extracted by wet digestion showing slightly bigger particles. D) SEM micrograph of extracted silica by wet digestion. E) Unextracted silica detected in situ in a leaf cross-section showing a "cloudy" irregular structure. F) Nano-FTIR absorption spectra taken from silica phytoliths extracted by SONE (1) and MAD (2). Figure adapted with permission from Zancajo, V. M. R. *et al. Anal. Chem.* 2020, 92, 20, 13694–13701.

Regardless of the variations on the molecular structure of the silica, depending on the method used to extract the phytoliths from the plant tissue shown by Raman microspectroscopy and Nuclear magnetic resonance (NMR) spectra in Chapter 4, in the nano-IR spectra here, the position of the silica band is consistent for phytoliths purified by both extraction methods (compare spectra in Figure 6.4F). The consistency in the phonon position (Figure 6.4F) implies that the Si-O-Si vibration representing the bulk of the silica particles is less affected by the extraction method, in agreement with the Raman data previously presented in Chapter 4, that revealed differences mainly in the surface Si-OH groups and organic matter occluded in the phytoliths. These spectra were collected at a very high lateral resolution, a few nm, and from very localized spots on the phytoliths. This can make molecular differences caused by different chemical modification due to the extraction method, as previously observed, such as different hydroxylation levels to go unnoticed. Also, in heterogeneous materials at the nanometre scale like the cell walls, the nano FTIR spectra will reflect the specific chemical composition of the small volumes probed, showing differences in spectra recorded in close proximity, in contrast with conventional FTIR in which much bigger volumes are sampled and averaged. Nevertheless, the nano FTIR spectra recorded from plant samples showed consistency with the general patterns expected for cell wall components (Figure 6.5).

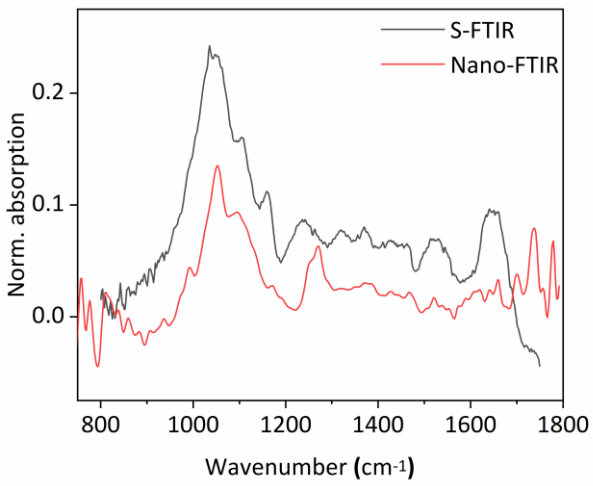

Figure 6.5. Comparison of FTIR spectra (synchrotron FTIR in black and Nano FTIR in red) taken from the cell wall of sorghum leaves.

6.4. Structure and distribution of biosilica in the cell walls of wheat awns

Organic constituents such as amino acids, lipids and carbohydrates were observed in extracted silica phytoliths by different approaches,[133, 161] including conventional micro-FTIR and Raman spectroscopies.[133] Nevertheless, the knowledge that can be obtained on the native state of the silica in the plant and the organic matrix in which the silica is formed is limited by the extraction procedures as they alter the nanostructure and condensation of the silica itself. The harsh conditions used to extract plant biosilica can, likely, change the organic matter and modify organic compounds. Therefore, investigating the silica deposits by vibrational spectroscopy *in situ* in the plant tissues without extraction is desirable. In Figure 6.6, scanning probe images of different areas in sections of a wheat awn (cf. Figure 6.1B) are shown. The sample was embedded in resin which allowed to obtain a flat cut, which is very convenient for the scanning probe measurements. Figure 6.6 shows the scanning near field optical image obtained using the mid-IR spectral range of a papilla. The infrared amplitude image showed great differences between the areas of the plant tissues and the embedding resin.

The IR amplitude image of the cell wall structure of xylem vascular tissue is shown in Figure 6.6B in great detail. Middle lamella, primary and secondary cell wall can be recognized. In this area of the wheat awn, silica deposition occurs to a much lower extent than in bilobate cells, papillae or sclerenchyma[228] (cf. Figure 6.1B for localization in the sample, starlet). The IR spectroscopic data obtained at nanoscale resolution allowed to get information on the different substructures of the plant cell walls *in situ*, such as the middle lamella in xylem tissues or the cell wall layers of the secondary cell wall in sclerenchyma cells. Figure 6.7 shows examples of nano-FTIR absorption spectra from positions in the images in Figure 6.6A, B, C. Although the typical vibrations of organic molecules would be found in the investigated spectral range, the spectra recorded from the papilla (Figure 6.6A, point 1) only showed strong silica signals (Figure 6.7, spectrum 1). This is consistent with the known heavy silicification of the domesticated wheat papillae,[228] and confirmed that it is strongly silicified.

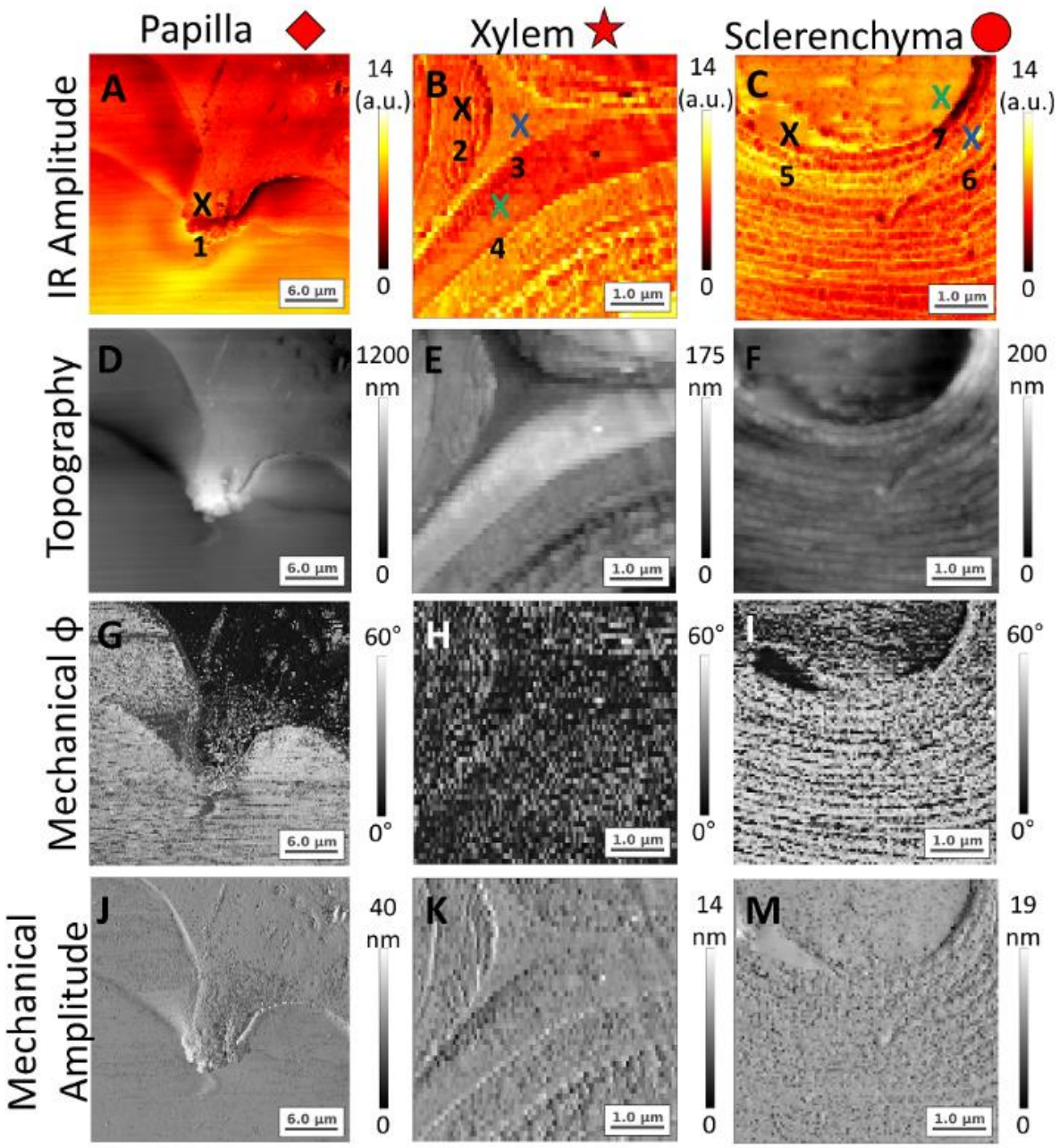

Figure 6.6: Images obtained from a resin-embedded wheat awn. Corresponding areas are marked in Figure 6.1 with a diamond (papillae), a star (cell wall structure of xylem plant vascular tissue, an area of the wheat awn that is low in silica) and silicified sclerenchyma cell (circle). (A-C) Broadband spectrally integrated infrared SNOM images, positions marked correspond to the nano-FTIR absorption spectra shown in Figure 6.7 (D-F) Topography images of the same area. (G-I) AFM mechanical phase images. (J-M) AFM mechanical amplitude images. Figure adapted with permission from Zancajo, V. M. R. *et al. Anal. Chem.* 2020, 92, 20, 13694–13701.

In contrast, contributions from organic molecules dominate the spectra from the xylem tissue (Figure 6.7, point 2, 3, 4). In this case, the signal around 1100 cm^{-1} was assigned to C-C stretching instead of the silica phonon. This signal was in the same region with the silica signal, but it had a much wider bandwidth and a lower intensity than the silica phonon. This broad band appeared together with a higher intensity signal between 1030-1060 cm^{-1} associated with the presence of structural carbohydrates, starch or homogalacturonan.[180] All these characteristics made the silica phonon easily distinguishable from organic counterpart. For plant cell wall analysis, the wavenumber range from 800-1200 cm^{-1} in the IR spectra is of particular interest. It provides information on structure and composition of common cell wall components, in particular of polysaccharides such as cellulose, hemicelluloses and starch. The absorption maxima in the IR spectra of polysaccharides forming plant cell walls are distinctive regarding the degree of substitution and the nature of the arabinose residues.[180] The 800-1200 cm^{-1} region of the xylem spectra presented here (Figure 6.7, spectra 2, 3, 4), was dominated by ring vibrations overlapped with stretching vibrations of (C-OH) side groups and the (C-O-C) glycosidic bond vibration.[229] Bands between 1030-1060 cm^{-1} arose probably from the presence of mannose, arabinose and rhamnose, structural units of the plant structural cell wall polysaccharides.[96]

Silica was identified in the completely silicified structures such as the papillae (Figure 6.6A), but also in inclusions within the cell wall of sclerenchyma cells (Figure 6.6C). The silica phonon band was clearly visible in spectra obtained from the cell wall layers of these cells (Figure 6.7). Nevertheless, some spectra taken from sclerenchyma cell wall layers showed signals consistent with polysaccharides but also a very intense band at 1100 cm^{-1} that is not expected for the polysaccharides (Figure 6.7, spectrum 5). This can be interpreted as an indication that the silica here was intermixed with structural polysaccharides, suggesting that in contrast to the heavily silicified papillae, in the less silicified cell walls, the biosilica was deposited together with the cell wall components.

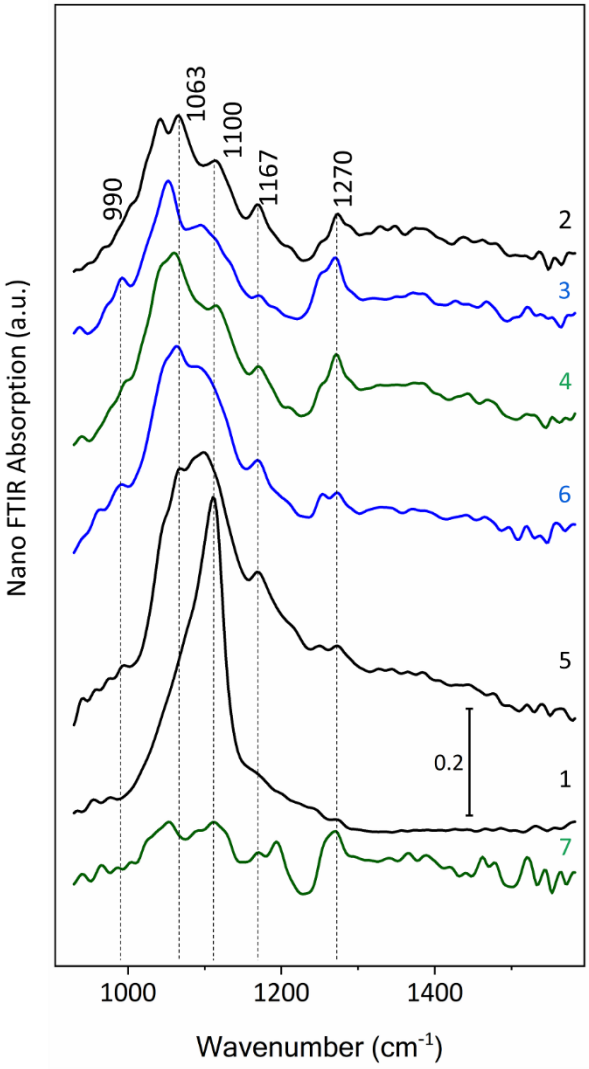

Figure 6.7: Nano-FTIR absorption spectra taken at positions marked in Figure 6.6. Spectrum 1 show intense silica signal from a heavily silicified papilla. The spectra 2-4 were taken from the cell wall structure of xylem plant vascular tissue, low in silica, and show mainly signals of polysaccharides and lack the sharp signal assigned to silica. The spectra 5 and 6 were taken at cell wall layers of sclerenchyma cells containing silica inclusions. Spectrum 7 was measured in the lumen of sclerenchyma cell and shows features consistent with epoxy resin (cf. Figure 6.3 for reference spectra). Figure adapted with permission from Zancajo, V. M. R. *et al. Anal. Chem.* 2020, 92, 20, 13694–13701.

The nano FTIR absorption spectra were obtained from probed small volumes, on the order of tens of zeptoliters. Therefore, inorganic silica and organic cell wall components showed heterogeneity at the nanometre scale. Silica and polysaccharides were presumably intermixed in the secondary cell wall of the sclerenchyma cell in wheat awns at a molecular level. Most probably, these polysaccharide components

played a role in the silica deposition in these locations. Similarly, as callose, a cell wall polysaccharide produced in response to stress or damage, has been suggested to induce silica deposition in *Arabidopsis* and horsetail (*Equisetum arvense*).[154, 156]

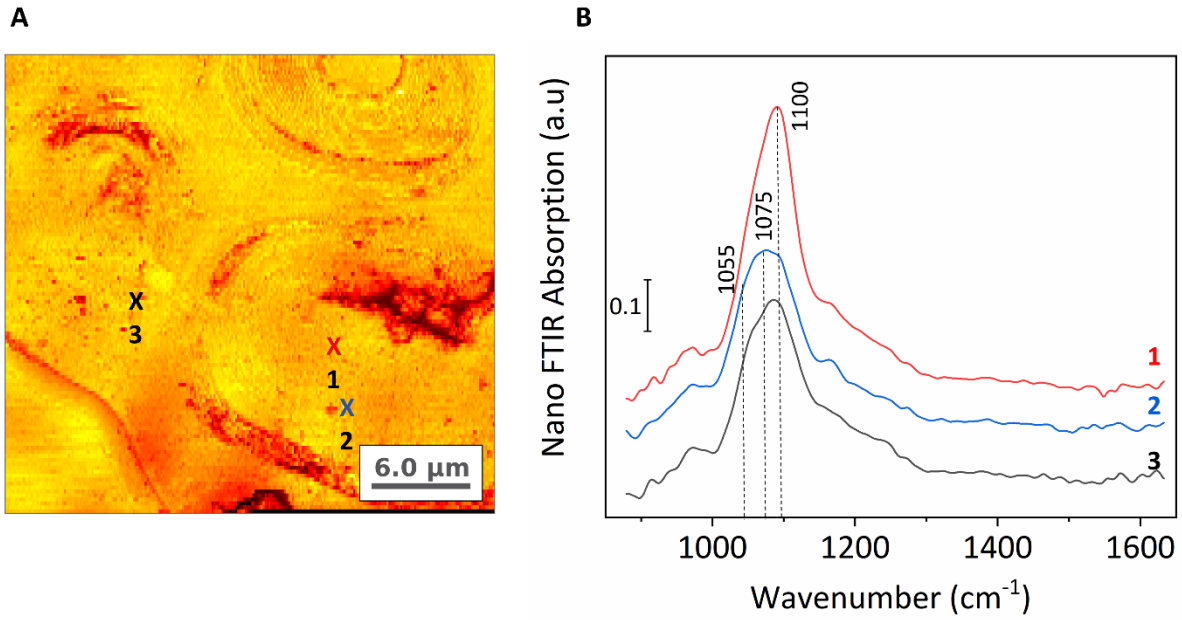

Figure 6.8: (A) Broadband spectrally integrated infrared SNOM image of silicified sclerenchyma, the positions marked correspond to the spectra shown in B. (B) Nano-FTIR absorption spectra showing the silica phonon resonance. Figure adapted with permission from Zancajo, V. M. R. *et al. Anal. Chem.* 2020, 92, 20, 13694–13701.

The spectra that were taken from the lumen of the sclerenchyma cell only showed epoxy resin signals (Figure 6.6C, point 7 and Figure 6.7, spectrum 7), no remains of cellular content could be identified.

The high-resolution AFM images together with mechanical information obtained from the sections of the embedded tissue complement the chemical information provided by the IR spectra. The resin embedding procedure followed by the cutting with a diamond knife produced a very flat sample surface, confirmed by the AFM topography images (Figure 6.6D, 6.6E, and 6.6F), making the samples especially suitable for IR nanospectroscopic analysis. At the same time, the smaller differences in height detected by the cantilever were enough to reveal the cellular substructures. The chemical composition that is revealed by the IR spectra can be directly connected with

the surface structure and material domains by comparing the topography images and the mechanical phase images. The mechanical phase images exhibited a strong phase contrast of about 60° (figures 6.6 G-M), which indicates the presence of materials with different mechanical properties,[230] such as the surface stiffness, softness and adhesion forces between the tip and the surface sample. The border of the area delimiting the epoxy resin within the silicified papilla is clearly visible in Figure 6.6G, as the different chemical composition caused very different mechanical properties of the two. The xylem tissue (Figure 6.6H and Figure 6.6K) did not show strong differences, suggesting very uniform mechanical properties. The multiple layers of the thick secondary cell wall of sclerenchyma cells were clearly visible in the IR images (Figure 6.6C) and also in the mechanical phase image (Figure 6.6I). Different optical properties were inferred by the contrast in the IR image, which can be a consequence of chemical differences or different organization of the cellulose fibrils. Typically, these cells organize in a plywood structure with different stiffness in the different layers that enable the awn to react to changes in humidity by a directed movement.[231] These layers showed a contrast of ~ 0.6 rad and are approximately 100 nm thick (Figure 6.9 B). The mechanical phase image in Figure 6.9A also showed a high contrast between the layers. The scanning-probe IR images and the mechanical phase image indicated that the plywood structure of the cell wall is the result of different chemical composition and structure between layers. The layers with high IR reflectance correlated with low mechanical phase and showed IR spectra with high intensity of the 1100 cm^{-1} silica band. This could indicate silica deposition in the cell wall layers providing different mechanical properties to the cell wall in comparison with the other components. IR nanospectroscopic localized probing of the cell wall layers can give information on the contribution of the chemical composition to the specific mechanical properties of the cell wall in addition to the varying directionality of the cellulose. This is particularly interesting, as silica has been suggested to play a role changing the mechanical properties of the cell wall, silica and lignin may both increase cell wall stiffness.[155, 232, 233]

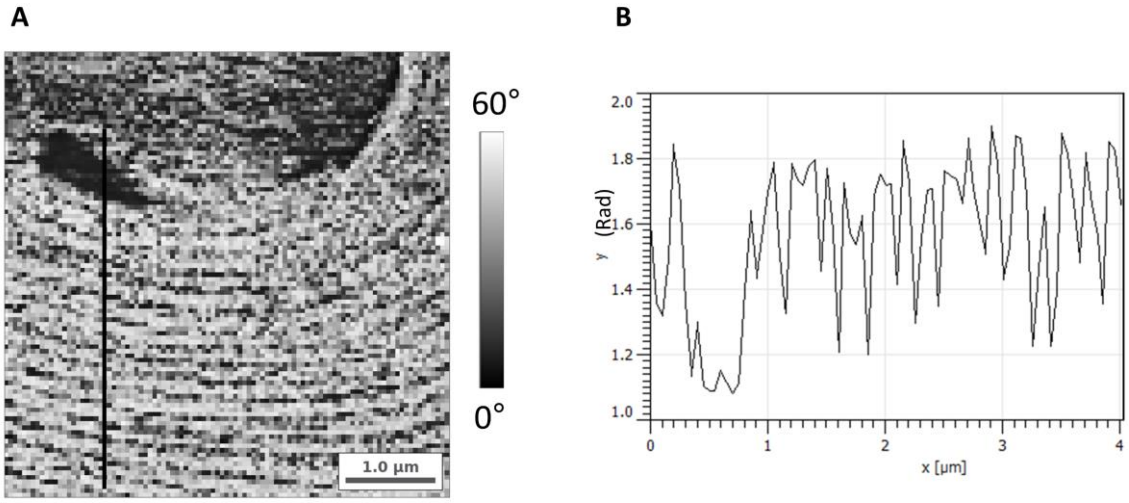

Figure 6.9: (A) Mechanical phase image of the sclerenchyma sample shown in Figure 6.8. (B) mechanical phase profile of the line marked in A, showing differences of ~ 0.6 rad between cell wall layers, the thickness of the layers is approximately 100 nm. Figure adapted with permission from Zancajo, V. M. R. *et al. Anal. Chem.* 2020, 92, 20, 13694–13701.

6.5. FTIR nanospectra of unfixed leaf tissues

Epoxy resin embedding allows a smooth and flat sample surface that enabled the acquisition of high-quality scanning probe images and spectra. The contribution of the epoxy resin to the vibrational spectra of the sample was reasonable and did not impair the rich chemical information that was obtained. Nevertheless, to study non-embedded plant materials is of great interest, since it provides greater versatility, simple sample preparation, and the acquisition of IR nanospectra from chemically unaltered samples. To test the feasibility of analysing native samples, a region near the epidermis of a freshly cut sorghum leaf, including a transversal cut of a bilobate silica cell was selected from a leaf cross-section. The broadband spectrally integrated infrared SNOM image of a silicified bilobate cell from the fresh sample is displayed in Figure 6.10. The mechanical amplitude image (Figure 6.10B) provided better resolution than the topography image (Figure 6.10C) and allowed a clear distinction of the substructure of the phytolith *in situ* in the tissue. The silica nanoparticles in the

phytolith could be observed in detail (see also Figure 6.4). They showed remarkable differences in size and arrangement compared to the extracted silica (compare Figure 6.4A and 6.6B, Chapter 4 and e.g., refs.[87, 151]).

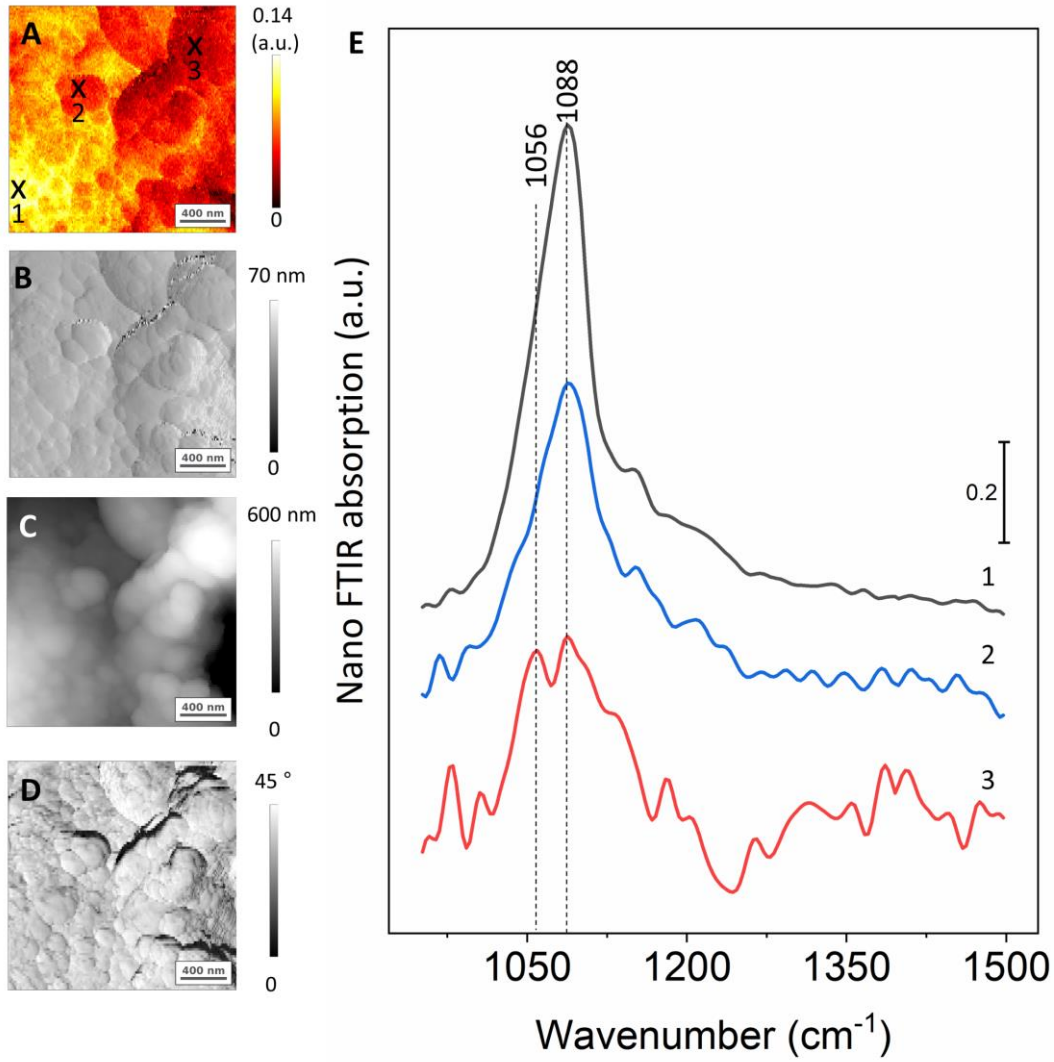

Figure 6.10: Nano FTIR images and spectra taken from unembedded samples. A) Broadband spectrally integrated infrared SNOM image of heavy silicified bilobate silica cell from a sorghum leaf. (cf. Figure 1C). B) mechanical AFM amplitude image of the same area. C) Topography image. D) Mechanical phase image of the same area E) Nano-FTIR absorption spectra taken at positions marked in A. Figure adapted with permission from Zancajo, V. M. R. *et al. Anal. Chem.* 2020, 92, 20, 13694–13701.

In this untreated sample, a less monodisperse, and more 'cloudy' silica structure (Figure 6.10B, Figure 6.4) instead of the typical granular silica can be observed. Only smaller areas were analysed due to the cutting procedure of the sample that produced much bigger differences in height in the sample topography, therefore making the scanning of areas of a few micrometres not possible. The IR nanospectra showed different extent of contributions of silica signals regardless of the location in the bilobate cell (Figure 6.10). The silica band appeared here at 1088 cm^{-1}, slightly shifted to a lower frequency. Interestingly, the variations in the silica band intensity did not correlate with variation in the mechanical amplitude or the mechanical phase (Figure 6.10 B, D).

6.6. Conclusions

In this chapter, IR spectroscopy at nanoscale lateral resolution has been used to study three different types of plant samples. FTIR nanospectra were obtained for all preparation procedures and plant tissue types. The plant samples present a variation in the content of inorganic and organic material, relevant to assess the ability of the nanospectroscopic approach to characterize hybrid plant materials including silicified tissues. Nano IR allowed probing both, the organic matter and the silica. IR nanospectra were obtained from both sample preparations, epoxy embedded sections and native tissues and cells. The spectra obtained from fresh samples demonstrate that it is possible to analyse native samples with no need for embedding or ultrathin cutting to enhance the signals. The results presented here show the great potential of nano-IR to study silicification *in situ*. However, more research will be needed to elucidate the mechanisms and physiological context, including potential molecules that induce silica deposition.

The obtained nano IR spectra showed different contributions of the organic cell wall and the very small and scattered inorganic silica inclusions. While no silicification was observed in the cell walls of the xylem tissue, the strong silica phonon resonance was identified in spectra that were measured from highly silicified papilla in wheat awns with no organic contribution. In contrast, the spectra from the smaller silica deposits in the sclerenchyma cells showed both organic and silica contributions, suggesting that

they are embedded in or contain a large fraction of the organic cell wall matrix. The sclerenchyma layers showed high contrast in the IR and mechanical phase images. This, together with the spectra collected from the small probed volumes, lead to conclude that there is chemical heterogeneity at the nanometre scale. The chemical heterogeneity of the silica bodies can be studied also *in situ* together with the nanoscopic substructure of the phytoliths. Bilobate cells, in contrast to other silicified cells, seem to accumulate silica through an active, physiologically regulated and protein-linked process.[5, 56, 62] However, protein signatures were not detected.

The high lateral resolution of the s-SNOM IR nanospectroscopy provides a main advantage for studies of other inorganic-organic hybrid materials, not only in the context of biomineralization. In plant science, nano FTIR offers the possibility to study the composition and molecular structure and interaction in substructures of the cell walls. Thereby, for example, a better understanding may be gained on the mechanical properties and movement of plant cells and tissues, which is of great importance in a variety of fields, such as bionics and materials research.

Chapter 7

In vitro silica precipitation assays

Parts of the results presented in this chapter are published on *J. Exp. Bot.* 2017, 71, 21, 6807–6817.

Many studies indicate correlation and dependence between the silica deposition and lignin/phenolic compounds.[233-240] Furthermore, silica deposits are frequently associated with lignified tissues.[205, 238, 241] When plant cell walls are lignified, multiple phenolic compounds couple in radical reactions and incorporate into the growing lignin polymer. The fundamental subunits to form lignin are coniferyl alcohol (CA), p-coumaryl alcohol and sinapyl alcohol, producing the G-, H- and S-subunits of the lignin polymer, respectively. Although their proportions vary between species, G-lignin is found as the most abundant subunit in grasses.[242] Ferulic acid (FA) is not one of the three canonical monolignols. Nonetheless, ferulates are a natural component of lignins in grasses and should be considered a monolignol as well.[243] In addition, ferulic acid cross-links the non-lignified cell walls via ferulic acid–arabinoxylan complexes (FA-AX).

In the roots of sorghum, silica aggregates are associated with the thickened cell walls, which appear only after the lignification of the inner tangential cell wall initiates and contain traces of the FA-AX complexes.[155] These observations indicate a possible interconnection between the deposition of silica and phenolic compounds.

The involvement of proteins in plant silicification has been proposed on several occasions. Kauss and co-workers proposed the involvement of a protein-rich in lysine amnio acids in the silica deposition in cucumber.[59] Amino acids have been recovered after extraction with hydrofluoric acid of silicified hairs from the lemma of the grass Phalaris canariensis[60] and the N/C ratio measured using Nanoscale Secondary Ion

Mass Spectrometry (NANO SIMS) in wheat phytoliths is in agreement with the presence of amino acids.[61] The Raman spectra that were taken from extracted phytoliths from sorghum leaves shown in Chapter 4 show also signals consistent with the presence of proteins. A protein (Siliplant1) have been proposed as responsible for the silica deposition silica in sorghum silica cells very recently.[62] This protein has seven peptide repeat units rich in lysine, similar to diatoms silaffins[63] and several proline residues as in a proline-rich protein (PRP1) from cucumber.[59] The peptide sequence HKKPVPPKPKPEPK is repeating several times in the domains.

This chapter presents the results on in vitro synthesis of lignin like polymer formed using coniferyl alcohol and ferulic acid as precursors, and the co-deposition of silica with the lignin like polymer from an oversaturated solution of silicic acid. Precipitation assays were performed *in vitro* using the mentioned peptide fragment (Peptide-1) and another peptide where the lysine residues were replaced by alanine (HAAPVPPAPAPEPA; Peptide-3) from a solution containing silicic acid at oversaturated concentration. Thus, this study aimed to identify processes and components crucial for silica formation and to elucidate the relationship between silica formation and lignification and silica formation induced by peptides. Characterization using vibrational spectroscopy, Raman and Fourier-transform infrared (FTIR), of the precipitation products of lignin polymers and peptides are presented and the feasibility of this process occurring naturally in the plant is discussed.

7.1. Coniferyl alcohol and ferulic acid polymers establish nucleation sites for silica deposition in vitro

To assess the potential relationship between silica and lignin deposition, *in vitro* lignin-like production was established. The system is based on the dehydrogenation of coniferyl alcohol (CA) alone, or in mixtures together with ferulic acid (FA) and arabinoxylan (AX), using peroxidase and H_2O_2 and further studied by vibrational spectroscopy, both Raman and FTIR. Conditions are described in detail in section 3.14.

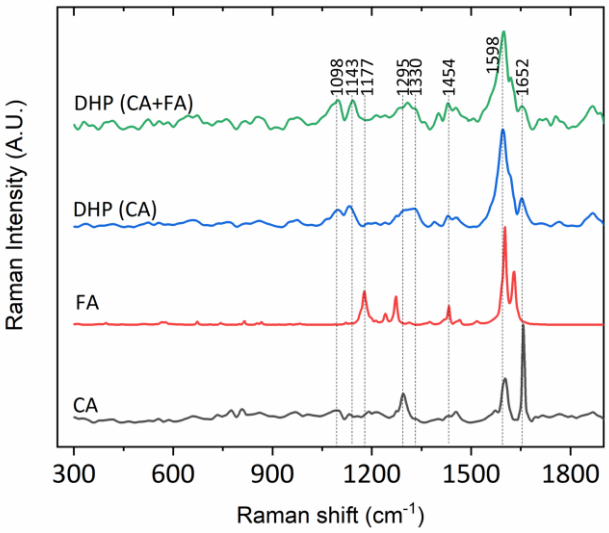

Figure 7.1: Raman spectra of Coniferyl alcohol (CA), Ferulic acid (FA) and synthetic lignin (dehydrogenated polymer) synthesized from CA, and a mixture of CA and FA. The band at ~1598 cm^{-1} appeared in all compounds with, the rest of the bands are not consistent between the precursors and the final products.

Figure 7.1 shows the Raman spectra of CA, FA and the lignin like polymers formed by oxidative coupling from CA alone or a mixture of CA and FA. Figure 7.2 shows the FTIR spectra of the precursors used for the reactions CA, FA, and AX. The bands observed in the polymers differ substantially from the ones observed in the Raman spectra of the precursors. This indicates the limitation to use the precursor spectra to elucidate the structure of the formed polymers and ultimately of the plant lignin. Potential assignments of Raman bands of lignin and dehydrogenation polymers (DHPs) have been discussed in Chapter 5.

No solid product was collected in the absence of CA, peroxidase, or H_2O_2. When the reaction was performed using CA alone, a dehydrogenated polymer was obtained with a reaction yield of 68% (Table 7.1). The presence of AX in the reaction strongly reduced the yield, while 10% FA reduced the polymerization yield only slightly. The low yield of lignin synthesis in the presence of AX did not allow for further analysis. Surprisingly, the 1:1 mixture of FA/CA failed to produce any polymer (Table 7.3). However, conducting the reaction with a CA/FA ratio of 9:1 produced a lignin polymer modified by ferulic acid (Figure 7.3). The FTIR spectrum of the CA polymerisation product showed bands at 1031, 1139, 1214, 1267, 1350 and 1598 cm^{-1} (band assignment

to vibrations is shown in Table 7.2) was characteristic and consistent with the IR spectrum of lignin.[173] The signal at 1750 cm^{-1}, assigned to the ester bond carbonyl stretching vibration, appears as a consequence of the incorporation of FA into the polymer. Other spectral variations attributed to aromatic ring stretching, C-H stretching, and deformation vibrations were also found in the bands at 1598, 1346, 1214 and 1139 cm^{-1}.

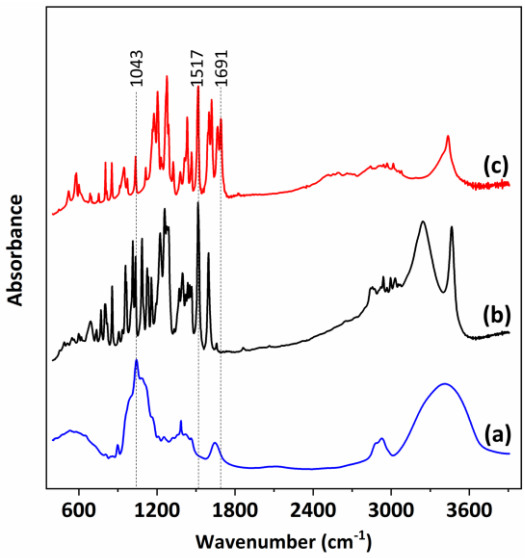

Figure 7.2: FTIR spectra of arabinoxylan (a), coniferyl alcohol (b) and ferulic acid (c). The FTIR spectra of coniferyl alcohol and ferulic acid are very rich in bands, however, they not consistent with the ones exhibited by the products (Figure 7.3). FTIR spectrum of arabinoxylan showed the characteristic pattern described in Chapter 5 of cell wall carbohydrates with a maximum at 1043 cm^{-1}.

When silicic acid was added to the oxidative coupling reaction of either pure CA or CA+FA at 20 mM final concentration, infrared absorptions typical to silica appeared in the spectra (Figure 7.3B). Addition of silicic acid to the reaction solution resulted in increased yield (Figure 7.4). The increased yield relative to the CA precursors started only above 10 mM silicic acid, growing linearly with the addition of silicic acid (Figure 7.4A). The higher the silicic acid concentrations in the reaction, the higher was the fraction that precipitated (Figure 7.4B).

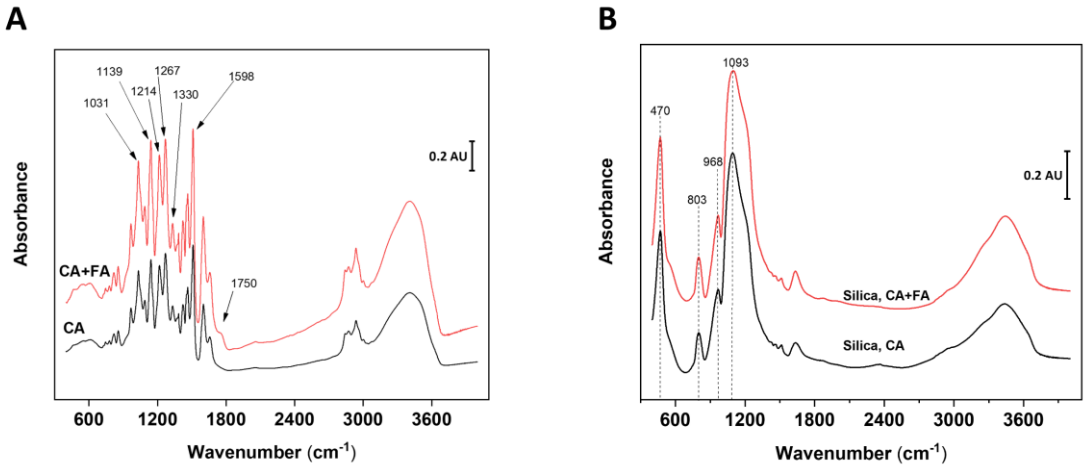

Figure 7.3: Infrared spectra of synthetic lignin, silica gel, and silica formed with the synthetic lignin. (a) Comparison of spectra of synthetic lignin formed using CA alone (in black) and CA + FA (in red) as precursors in the polymerization reaction. The main difference in the spectra is the presence of a band at 1750 cm^{-1} that corresponds to stretching vibration of the carbonyl (C=O) bond. This distinctive band indicates the presence of an ester bond and confirms the incorporation of FA to the polymer. (b) Infrared spectra of silica formed with the synthetic lignin produced using CA alone (in black) and CA + FA (in red) show typical silica bands. No differences were found between the spectra. Figure adapted with permission from *J. Exp. Bot.* 2020, 71, 21, 6807–6817.

The concentration of silicic acid used is in the range of silicic acid measured in sorghum sap in Chapter 4 and probably reflects the Si concentration at its deposition sites.[244] These results indicate a catalytic deposition, enhanced by silicic acid availability, and not a stoichiometric reaction with the polymerized lignin. When the silicic acid concentration was lower than 15 mM, the infrared spectra of the product showed only typical lignin bands (Figure 7.4C). When using concentrations of 15 and 20 mM silicic acid, both silica and lignin bands could be identified. When using higher silicic acid concentrations, silica bands dominated the spectra and masked the lignin polymer signals (Figure 7.4C). For the concentrations below 15 mM of silicic acid, the solution probably contains dimers and small oligomeric chains of silica as the silica solubility is estimated to be 2 mM.[30] But probably the reaction time was not long enough to allow the formation of detectable silica particles.

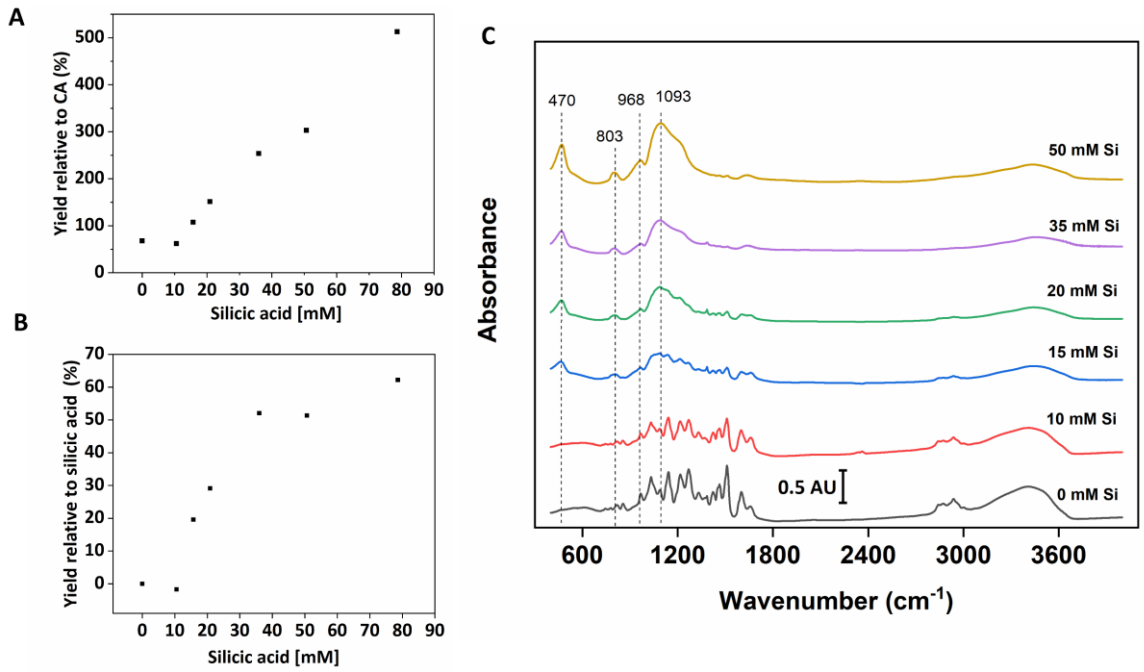

Figure 7.4: Reaction yields of the *in vitro* lignin and silica formation. (A) Total yield calculated relatively to the CA precursors added to the reaction (B) Silica yield calculated by estimating a yield of the synthetic lignin of 68% (mean yield reaction with no addition of silicic acid). (C) Infrared spectra of the reaction product. In the products formed with concentrations of silicic acid higher than 20 mM only the silica signals are visible and mask the lignin bands completely. Figure adapted with permission from *J. Exp. Bot.* 2020, 71, 21, 6807–6817.

7.2. Silica gel and coprecipitated silica-lignin showed spectroscopic differences

Silicic acid auto-polymerized from oversaturated solutions in reaction mixes missing the lignin polymerization precursors (product denoted as SiO_2-Auto). This was expected from the well-known ability of silicic acid to auto-polymerize. Nevertheless, the silica obtained together with CA polymer (denoted as SiO_2-CAp) exhibited spectral and morphological differences from SiO_2-Auto (Figure 7.5). A band that is assigned to the stretching vibration of non-bridging -SiOH,[245] appeared in the spectra of SiO_2-CAp at 968 cm^{-1} and in the SiO_2-Auto spectra at 983 cm^{-1}. SiO_2-Auto formed a soft transparent gel, similar to gelatine, which was still very soft after 4 hours of drying at 40°C. The gel hardened only after several days, presumably due to water loss, preserving its transparent appearance. In contrast, SiO_2-CAp had a whitish appearance

with a sandy texture, developing a solid and hard consistency already after a 4-hour drying (Figure 7.5 inset).

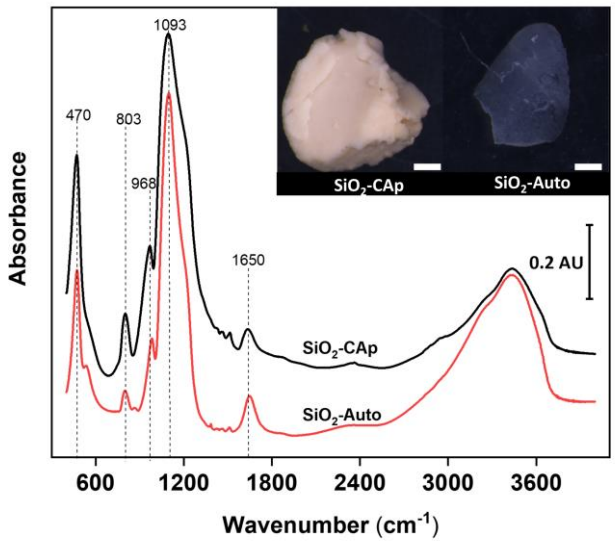

Figure 7.5: Comparison of silica obtained by silicic acid autopolymerization (SiO_2-Auto) and silica precipitated together with the lignin like polymer (SiO_2-CAp). Infrared spectra of SiO_2-Auto (in red) and SiO_2-CAp (in black) show differences in the position of the band corresponding to the -SiOH stretching (shifted from 968 cm^{-1} in SiO_2-CAp to 983 cm^{-1} in SiO_2-Auto), the shoulder of the band at 1093 cm^{-1} (asymmetric stretching Si-O-Si) and the relative intensity of the band at 803 cm^{-1} (Si-O-Si symmetrical stretching mode). Such spectral variations indicate differences in the molecular order between the two materials. The SiO_2-Auto was formed at 20 mM concentration. The SiO_2-Cap was formed at 80 mM silicic acid, to minimize signals of lignin. Insets: photographs of the SiO_2-Auto (right) and SiO_2-CAp (left) suggest that these are two different minerals. Scale bars 500 μm. Figure adapted with permission from *J. Exp. Bot.* 2020, 71, 21, 6807–6817.

7.3. Silica is deposited after lignin formation

Visual inspection suggested that the lignin-like polymer started to form immediately; however, it seems that silica formation is delayed (Figure 7.6B). After 3 hours of CA polymerisation in the presence of silicic acid only the synthetic lignin and no silica was detected (Fig 7.6). SiO_2-CAp formed when the synthetic lignin (product of the 3-h

experiment), was centrifuged, rinsed, re-dissolved in phosphate buffer with 20 mM silicic acid, and stirred for 15 additional hours. This was shown by the presence of prominent silica bands in the IR spectrum (Figure 7.6, spectrum c), consistent with the SiO_2-CAp IR spectra (Figure 7.5). This result indicates that the SiO_2-CAp formed at a later stage, catalysed by the CA polymer. This result is in agreement with the studies by Fang et al.[246] and Fang and Ma[236], who observed that silica precipitation can be induced in vitro by synthetic or natural lignin, but not lignin monomers.

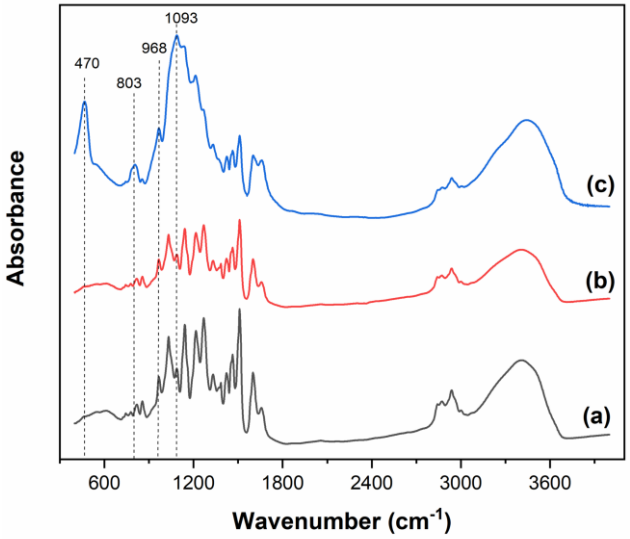

Figure 7.6: Infrared spectra of synthetic lignin and SiO_2-CAp at 3 and 18 hours. (a) CA polymerization product in absence of silicic acid after reaction of 18 hours. Synthetic lignin was detected. (b) CA polymerization product in the presence of silicic acid after 3 hours reaction. Synthetic lignin with no silica bands was observed. (c) After a 3-h reaction CA polymerization product was redissolved in a 20 mM silicic acid solution and left to react for another 15 hours. Silica and lignin bands are visible. Figure adapted with permission from *J. Exp. Bot.* 2020, 71, 21, 6807–6817.

7.4. Peptide-silica precipitation

To test the ability of peptides containing lysine amino acids to precipitate silica, and especially the possibility of Siliplant1 protein[62] to precipitate silica in sorghum, *in vitro* precipitation assays were performed. Siliplant1 was described in section 2.6. The results presented here are based on precipitation experiments that were performed as

part of the study published by Kumar et.al..[62] Peptide-1 (HKKPVPPKPKPEPK), a sequence that appears five times in the Slp1 primary sequence and Peptide-3 (HAAPVPPAPAPEPA), where all lysine groups in Peptide-1 were replaced by alanine were used in silica precipitation assays, as described in Chapter 3.

The silica precipitation using peptides was extremely fast. After a few minutes, silica formation was observed in contrast with the several hours requires for the formation co-deposition of silica and lignin polymer. This indicates a much stronger affinity between the silica and the peptides than between silica and lignin. Nevertheless, the different peptides tested interacted differently with the silica. Whitish powder sediment was recovered from the reaction using peptide 1 whereas peptide 3 formed a gel-like material. These products were analysed by Raman spectroscopy (Figure 7.7). No laser-induced fluorescence was observed on the peptide-silica samples, allowing the acquisition of Raman spectra. In contrast to the silica obtained using lignin, this suggests that the silica does not fluoresce by itself, but all the fluorescence observed must be a consequence of the lignin polymers. The Raman spectra of the peptides showed a wide band with a maximum at 1650 cm^{-1}, assigned to Amide I.[247] Another band at 1450 cm^{-1}, arising from CH deformations,[247] was observed in both peptides (Figure 7.7 spectra Pep1 and Pep3) and the silica precipitates for both peptides (Figure 7.7 spectra Pep 1 + Si I, Pep1 +Si II and Pep3 +Si). Interestingly, this band was observed at a lower Raman shift (1437 cm^{-1}) in the Raman spectra of peptide 1 but at 1450 cm^{-1} in the silica precipitate (Figure 7.7 spectrum Pep1). Some unassigned bands appeared as well in the Raman spectra of the silica precipitate formed by peptide 1. This suggests strong interactions of peptide-1 with the silica. The precipitates for both peptides showed the characteristic Si-O deformation of silica at 488 cm^{-1}. The precipitate obtained with peptide 1 showed heterogeneity at the micrometre scale, as deduced by the different Raman spectra obtained across the sample (Figure 7.7 spectra Pep 1 + Si I, Pep1 +Si II). Some of the Raman spectra showed strong signals consistent with the presence of agglomerations of the peptide while the others peptide bands were diminished (Figure 7.7 spectrum Pep 1 + Si I) or even showed only silica signals. Probably the peptide induces the nucleation of silica and the silicic acid is subsequently reacting, leading to the growth of silica particles. The Raman spectra of the supernatant

only showed Raman signals assigned to phosphate. This could be an indication of the high affinity of the silicic acid towards the peptide.

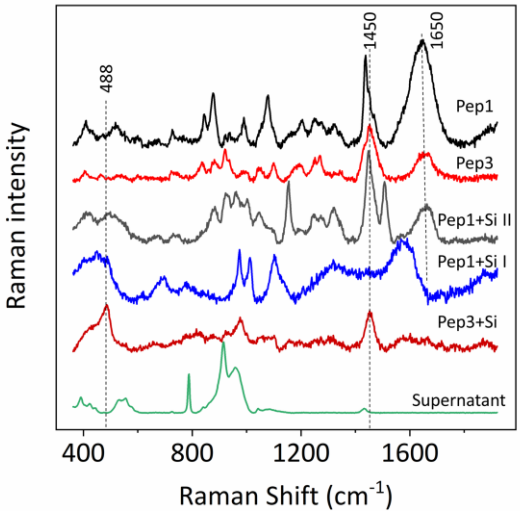

Figure 7.7: Representative Raman spectra of peptide-1 (Pep1), peptide-3 (Pep3), silica precipitates using peptide 1 (Pep1+Si I and Pep1+Si II), silica precipitate using peptide 3 (Pep3+Si) and supernatant recovered from precipitation with peptide I.

Due to the limited amount of peptides available, no FTIR spectra of the peptides were recorded. The FTIR spectra of the products obtained from the precipitation of peptides with silicic acid were consistent with FTIR spectra of silica (Figure 7.8) and very similar to the ones obtained from the silica co-deposited with lignin, compare with Figure 7.5. Interestingly, the FTIR spectra of silica obtained by peptide 1 showed the -SiOH stretching band at 968 cm^{-1} whereas in the case of the silica obtained by peptide 3 this band was shifted to 976 cm^{-1}. This was similar to the differences observed between the co-precipitated silica-lignin and the silica gel (compare Figures 7.5 and 7.8). This band is strongly affected by hydrogen bridges bonding and probably the changes in trapped water within the silica structure influence its position causing the shifts observed in the silica gels and the precipitated silica.

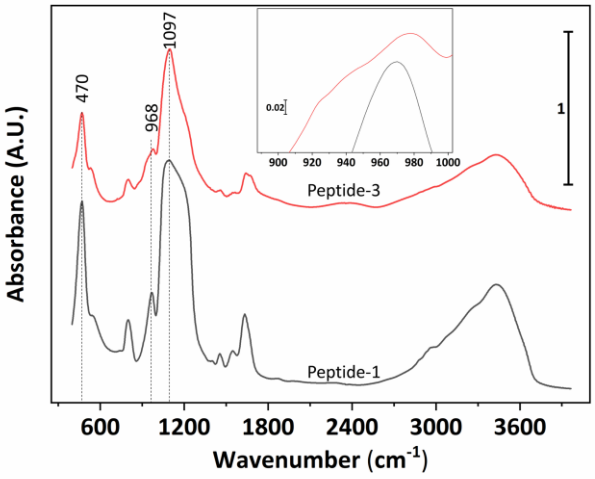

Figure 7.8: FTIR spectra of the silica obtained after precipitation with peptide 1 and peptide 3. Characteristic silica signals are observed in both; however, the spectra show differences in the position of the band corresponding to the -SiOH stretching shifted from 968 cm^{-1} in silica obtained by Peptide-1 to 976 cm^{-1} in silica obtained by peptide-3 (inset).

7.5. Conclusions

In vitro experiments to precipitate silica were performed aiming to test the chemical feasibility of lignin and the protein to provide the environment for *in vivo* silicification. Silica was co-deposited with lignin like polymers and using a lysine-rich peptide. The *in vitro* experiments simulating the polymerization of coniferyl alcohol in the cell wall suggested a chemical interaction between the deposited silica and the biopolymer matrix. This interaction is probably facilitated by hydrogen bonds formed between the lignin and -SiOH or H_2O trapped in silica pores. The biopolymers could act as templates catalysing silicic acid polymerization to silica. Interestingly, the silica was not formed during the CA polymerization, but only after most of the CA polymerized.

Silica precipitates were obtained in a few minutes with a peptide sequence of siliplant1. As observed here, peptide 1 actively precipitates silica in vitro. This suggests that Siliplant1 is causing the silica deposition in bilobate silica cells in sorghum as proposed by Kumar et. al.[62] Specifically the Raman spectra showed in Figure 7.7 confirm the

previous findings and the IR data reported here (Figure 7.8) provide additional support from such interpretation.

Supersaturated solutions of silicic acid are not thermodynamically stable. In a short time, condensation polymerization takes place through dehydration.[30] Nevertheless, according to the control experiments performed here, this process takes several hours and results in soft silica gel, probably highly hydrated and not fully condensed. In contrast, the silica obtained by co-precipitation with lignin and peptide-1 has the appearance of solid powder and forms quickly, especially in the case of the peptide in which just a few minutes are needed. Nevertheless, the results presented here confirm the feasibility of these processes *in vitro* and therefore suggest that these interactions may also occur *in vivo*. However, more research is needed to confirm that silica is deposited in the plant through interactions of lignin and proteins.

Chapter 8

Summary and outlook

The main scope of this thesis was to gain a better understanding of the processes that govern silica deposition in plants using the example of sorghum leaves. The samples were investigated using methods that assess different length scales, ranging from the nanoscale in x-ray analysis and scattering-type near-field optical microscopy (s−SNOM) over the microscopic level, and to the observation of macroscopic parameters. Three major objectives were addressed. (I) The characterization of extracted sorghum phytoliths was presented in Chapter 4. (II) The characterization of the organic matrix where silica is deposited was undertaken in Chapters 5 and 6. (III) The evaluation of the ability of model compounds to induce silica deposition *in vitro* was explored in Chapter 7.

The consequence of plant silicification is the formation of phytoliths, microscopic structures of silica within the plant cells and tissues. The phytoliths are very diverse and fulfil many roles. Despite the evident morphological differences, phytolith chemistry has mostly been analysed in bulk samples, neglecting differences between the varied types formed in the same species. As shown in Chapter 4 different phytoliths showed different deposition patterns. As has been demonstrated by this work, different phytolith morphotypes show different chemical composition, as reflected in their vibrational spectroscopic signatures. The combination of Raman and IR microspectroscopy allowed to observe the tissue structures and their chemical composition. The use of Scanning Electron Microscopy with Energy Dispersive X-Ray Analysis (SEM-EDX) provided the unambiguous location of the silica deposits. Extracted phytoliths were discriminated using Raman and Fourier-transform infrared (FTIR) in combination with principal component analysis (PCA) according to their morphotypes. The found differences include the organic matter trapped within the silica but also the silica structure and condensation. This, in combination with the

heterogeneity in the plant silica, suggests several strategies used by the plant for the silica deposition and a diversity of its functions and origins. Therefore, the silicification mechanisms in higher plants cannot be considered as a whole but they need to be addressed independently for each type of phytolith, and preferentially *in situ*. The question of how plants can control silicification remains still open. In this context, the results presented in Chapter 4 are in line with observations that silicification in grasses exhibiting three general patterns.[5] Silica is either deposited at epidermal surfaces, cell walls of internal tissues, or intercellular spaces. The first type of silicification forms the long cells and seems to be driven mainly by water evaporation, therefore it can be considered as passive, though probably influenced by the cell wall composition. The formation of silica aggregates in sorghum root endodermis takes place exclusively in the cell walls of living cells and is dependent on the metabolic activity at the wall, and specifically deposition of matrix polymers.[155, 215, 248] The silica deposition in the internal locations is more puzzling and seems controlled actively.[56, 62]

The results presented in Chapter 5 provide a characterization of the materials in the native state with relevant spatial resolution. Brightfield, fluorescence and scanning electron microscopies were used to visualize the tissues and evaluate the silicification patterns at the cellular level. Vibrational spectroscopy, Raman and mid-IR spectroscopies in conventional microscopic- and near field setups were combined with multivariate analysis to obtain a complete molecular characterization of the tissues and of the different silica deposits. The obtained information can be used to elucidate specific lignin bonds and structure which appears to have a relevant role in plant silicification. Chapter 6 explored the use of spectroscopy techniques based on s-SNOM which offers new possibilities to study plant silica at nanometre and molecular scales and that will help to understand the molecular interactions of the cell wall components with the silica using this high resolution. The nano FTIR spectra shown in Chapter 6 of this dissertation suggest a heterogeneity of polysaccharides and silica at the nanometre scale in sclerenchyma cell walls, as studied here in the example of wheat awns. Hemicelluloses like callose (a β-1,3-glucan) have shown to be able to induce silica deposition *in vitro*,[154] they have been found in high concentrations, collocated with silica in horsetail (*Equisetum)* cell walls[153] and have been used as templates for industrial silica deposition.[159] The amorphous structure of polysaccharides with

multiple hydroxyl groups provides suitable microenvironments to initiate the condensation of silicic acid into silica.[157] Furthermore, some evidence suggests that silicon may bind covalently to hemicelluloses in rice cells.[42-44]

The performed *in vitro* experiments were focused on lignin and peptides. The amorphous structure of lignin seems also very suitable to initiate the condensation of silica. Many studies point to an obvious, yet not completely understood, relation between silica and lignin or phenolic compounds.[205, 238, 241, 246, 249-251] The data of the *in vitro* experiments in Chapter 7 of this thesis also demonstrated interactions between lignin like polymers formed from coniferyl alcohol and ferulic acid and silica, catalysing silica formation. Nevertheless, lignin structure and composition are very variable and complex, and different lignin types showed different degrees of affinity with silica and the ability to form it.[252] Therefore, more research is needed to understand the degree and ability of the lignin types to deposit silica. The Raman spectra taken from extracted phytoliths from sorghum leaves shown in Chapter 4 of this dissertation show signals consistent with the presence of proteins. Lysine and proline-rich proteins deposit silica in diatoms[63] and sponges, and have been proposed as silicification agents in cucumber[59] and sorghum silica cells.[62] Peptide-1 strongly interacts with silicic acid to form silica.

Research on plant silicification needs to continue, as the Si-induced benefits for plants offer great potential advantages to increase crop yields and quality, once they are understood and applied to a variety of crops. To understand plant silicification, future studies should focus on the cell-specific, temporal and spatial control over the process and to evaluate the interactions of silicic acid with plant proteins and other cell wall components. In particular, vibrational analysis at high resolution in native tissues, together with silica precipitation experiments with model compounds will bring a better understanding of the processes that govern silica deposition in plants.

Bibliography

(1) Cruger, H. Westindische Fragmente. El Cauto. *Botanische Zeitung,* **1857,** *9* (15), 281-292, 297-308.

(2) Von Mohl, H. Uber das Kieselskelett lebender pflanzenzellen. *Botanische Zeitung,* **1861,** *19*, 209-215.

(3) Coskun, D.; Deshmukh, R.; Sonah, H.; Menzies, J. G.; Reynolds, O.; Ma, J. F.; Kronzucker, H. J.; Bélanger, R. R. The controversies of silicon's role in plant biology. *New Phytologist,* **2019,** *221* (1), 67-85.

(4) Otzen, D. The role of proteins in biosilicification. *Scientifica (Cairo),* **2012,** *2012*, 867562.

(5) Kumar, S.; Soukup, M.; Elbaum, R. Silicification in Grasses: Variation between Different Cell Types. *Frontiers in Plant Science,* **2017,** *8*, 438.

(6) Piperno, D. In *Phytoliths: A Comprehensive Guide for Archaeologists and Paleoecologists*, 2006.

(7) Prychid, C. J.; Rudall, P. J.; Gregory, M. Systematics and Biology of Silica Bodies in Monocotyledons. *The Botanical Review,* **2003,** *69* (4), 377-440.

(8) Kelly, E. F.; Amundson, R. G.; Marino, B. D.; Deniro, M. J. Stable isotope ratios of carbon in phytoliths as a quantitative method of monitoring vegetation and climate change. *Quaternary Research,* **1991,** *35* (2), 222-233.

(9) Shahack-Gross, R.; Shemesh, A.; Yakir, D.; Weiner, S. Oxygen isotopic composition of opaline phytoliths: Potential for terrestrial climatic reconstruction. *Geochimica et Cosmochimica Acta,* **1996,** *60* (20), 3949-3953.

(10) Elbaum, R.; Weiner, S.; Albert, R. M.; Elbaum, M. Detection of Burning of Plant Materials in the Archaeological Record by Changes in the Refractive Indices of Siliceous Phytoliths. *Journal of Archaeological Science,* **2003,** *30* (2), 217-226.

(11) Hodson, M. Phytoliths in Archaeology: Chemical Aspects. In *Encyclopedia of Global Archaeology*, Smith, C., Ed. Springer International Publishing: **2018**; pp 1-8.

(12) Hodson, M. J. The development of phytoliths in plants and its influence on their chemistry and isotopic composition. Implications for palaeoecology and archaeology. *Journal of Archaeological Science,* **2016,** *68*, 62-69.

(13) Hodson, M. J.; Parker, A. G.; Leng, M. J.; Sloane, H. J. Silicon, oxygen and carbon isotope composition of wheat (Triticum aestivum L.) phytoliths: implications for palaeoecology and archaeology. *Journal of Quaternary Science,* **2008,** *23* (4), 331-339.

(14) Ball, T.; Chandler-Ezell, K.; Dickau, R.; Duncan, N.; Hart, T. C.; Iriarte, J.; Lentfer, C.; Logan, A.; Lu, H.; Madella, M.; Pearsall, D. M.; Piperno, D. R.; Rosen, A. M.; Vrydaghs, L.; Weisskopf, A.; Zhang, J. Phytoliths as a tool for investigations of agricultural origins and dispersals around the world. *Journal of Archaeological Science,* **2016,** *68*, 32-45.

(15) Yongchao L; Miroslav N; Richard B; Haijun G; Alin S, Silicon in Agriculture. From Theory to Practice, Springer: Netherlands, **2015**.

(16) Mukherjee, S.; Mishra, A.; Trenberth, K. E. Climate Change and Drought: a Perspective on Drought Indices. *Current Climate Change Reports,* **2018,** *4* (2), 145-163.

(17) Neethirajan, S.; Gordon, R.; Wang, L. Potential of silica bodies (phytoliths) for nanotechnology. *Trends in Biotechnology,* **2009,** *27* (8), 461-467.

(18) Van Tuan, N.; Ye, G.; van Breugel, K.; Fraaij, A. L. A.; Bui, D. D. The study of using rice husk ash to produce ultra high performance concrete. *Construction and Building Materials,* **2011,** *25* (4), 2030-2035.

(19) Delalat, B.; Sheppard, V. C.; Rasi Ghaemi, S.; Rao, S.; Prestidge, C. A.; McPhee, G.; Rogers, M.-L.; Donoghue, J. F.; Pillay, V.; Johns, T. G.; Kröger, N.; Voelcker, N. H. Targeted drug delivery using genetically engineered diatom biosilica. *Nature Communications,* **2015,** *6*, 8791.

(20) Exley, C. A possible mechanism of biological silicification in plants. *Frontiers in Plant Science,* **2015,** *6*, 853.

(21) Mann, S.; Perry, C. C.; Williams, R. J. P.; Fyfe, C. A.; Gobbi, G. C.; Kennedy, G. J. The characterisation of the nature of silica in biological systems. *Journal of the Chemical Society, Chemical Communications,* **1983,** (4), 168-170.

(22) Washington Le, M. E. C. Preparation and Characterization of Nano Silica from Equisetum arvenses. *Journal of Bioprocessing & Biotechniques,* **2015,** *05* (02).

(23) Jones, J. B.; Segnit, E. R. The nature of opal I. nomenclature and constituent phases. *Journal of the Geological Society of Australia,* **1971,** *18* (1), 57-68.

(24) Jones, L. H. P.; Milne, A. A. Studies of silica in the oat plant. *Plant and Soil,* **1963,** *18* (2), 207-220.

(25) Jones, L. H. P.; Milne, A. A.; Wadham, S. M. Studies of silica in the oat plant: II. Distribution of silica in the plant. *Plant and Soil,* **1963,** *18* (3), 358-371.

(26) Lanning, F. C.; Ponnaiya, B. W. X.; Crumpton, C. F. The Chemical Nature of Silica in Plants. *Plant Physiology,* **1958,** *33* (5), 339-343.

(27) Deshmukh, P.; Bhatt, J.; Peshwe, D.; Pathak, S. Determination of Silica Activity Index and XRD, SEM and EDS Studies of Amorphous SiO_2 Extracted from Rice Husk Ash. *Transactions of the Indian Institute of Metals,* **2012,** *65* (1), 63-70.

(28) Dietrich, D.; Hinke, S.; Baumann, W.; Fehlhaber, R.; Baucker, E.; Ruhle, G.; Wienhaus, O.; Marx, G. Silica accumulation in Triticum aestivum L. and Dactylis glomerata L. *Analytical and Bioanalytical Chemistry,* **2003,** *376* (3), 399-404.

(29) Rüdiger, B.; Reinhold, T. Solid-State 29Si VACP/MAS NMR Studies of Silicon-Accumulating Plants: Structural Characterization of Biosilica Deposits. *A Journal of Chemical Sciences,* **2000**.

(30) Iler, R. K., The chemistry of silica, Solubility, Polymerization, Colloid and Surface Properties, and Biochemistry, John Wiley and Sons: Chichester, **1979**.

(31) Jones, L. H. P.; Handreck, K. A. Silica In Soils, Plants, and Animals. In *Advances in Agronomy*, Norman, A. G., Ed. Academic Press: **1967**; Vol. Volume 19, pp 107-149.

(32) Belton, D. J.; Deschaume, O.; Perry, C. C. An overview of the fundamentals of the chemistry of silica with relevance to biosilicification and technological advances. *The FEBS Journal,* **2012,** *279* (10), 1710-20.

(33) Perry, C. C.; Keeling-Tucker, T. Biosilicification: the role of the organic matrix in structure control. *J Biol Inorg Chem,* **2000,** *5* (5), 537-50.

(34) Gierlinger, N.; Sapei, L.; Paris, O. Insights into the chemical composition of Equisetum hyemale by high resolution Raman imaging. *Planta,* **2008,** *227* (5), 969-80.

(35) Epstein, E. The anomaly of silicon in plant biology. *Proc Natl Acad Sci U S A,* **1994,** *91* (1), 11-7.

(36) Ma, J. F.; Yamaji, N. Silicon uptake and accumulation in higher plants. *Trends in Plant Science,* **2006,** *11* (8), 392-397.

(37) Takahashi, E.; Ma, J. F.; Miyake, Y. The possibility of silicon as an essential element for higher plants. *Comments on Agricultural and Food Chemistry,* **1990,** *2* (2), 99-102.

(38) Raven, J. A. Cycling silicon – the role of accumulation in plants. *New Phytologist,* **2003,** *158* (3), 419-421.

(39) Atkin, J. M.; Berweger, S.; Jones, A. C.; Raschke, M. B. Nano-optical imaging and spectroscopy of order, phases, and domains in complex solids. *Advances in Physics,* **2012,** *61* (6), 745-842.

(40) Blackman, E. Observations on the development of the silica cells of the leaf sheath of wheat (Triticum aestivum). *Canadian Journal of Botany,* **1969,** *47* (6), 827-838.

(41) Blackman, E.; Parry, D. W. Opaline Silica Deposition in Rye (Secale cereale L.). *Annals of Botany,* **1968,** *32* (1), 199-206.

(42) He, C.; Wang, L.; Liu, J.; Liu, X.; Li, X.; Ma, J.; Lin, Y.; Xu, F. Evidence for 'silicon' within the cell walls of suspension-cultured rice cells. *New Phytologist,* **2013,** *200* (3), 700-709.

(43) Ma, J.; Cai, H.; He, C.; Zhang, W.; Wang, L. A hemicellulose-bound form of silicon inhibits cadmium ion uptake in rice (Oryza sativa) cells. *New Phytologist,* **2015,** *206* (3), 1063-1074.

(44) He, C.; Ma, J.; Wang, L. A hemicellulose-bound form of silicon with potential to improve the mechanical properties and regeneration of the cell wall of rice. *New Phytologist,* **2015,** *206* (3), 1051-62.

(45) Currie, H. A.; Perry, C. C. Silica in Plants: Biological, Biochemical and Chemical Studies. *Annals of Botany,* **2007,** *100* (7), 1383-1389.

(46) Yamanaka, S.; Sato, K.; Ito, F.; Komatsubara, S.; Ohata, H.; Yoshino, K. Roles of silica and lignin in horsetail (Equisetum hyemale), with special reference to mechanical properties. *Journal of Applied Physics,* **2012,** *111* (4), 044703.

(47) Parry, D. W.; Hodson, M. J.; Sangster, A. G.; Jones, W. C.; O'Neill, C. H. Some Recent Advances in Studies of Silicon in Higher Plants [and Discussion]. *Philosophical Transactions of the Royal Society of London. Series B, Biological Sciences,* **1984,** *304* (1121), 537-549.

(48) Blaich, R.; Grundhöfer, H. Silicate incrusts induced by powdery mildew in cell walls of different plant species / Echter Mehltau induziert Silikateinlagerungen in Zellwänden unterschiedlichster Pflanzenarten. *Zeitschrift für Pflanzenkrankheiten und Pflanzenschutz / Journal of Plant Diseases and Protection,* **1998,** *105* (2), 114-120.

(49) Coskun, D.; Deshmukh, R.; Sonah, H.; Menzies, J. G.; Reynolds, O.; Ma, J. F.; Kronzucker, H. J.; Belanger, R. R. The controversies of silicon's role in plant biology. *New Phytol,* **2018**.

(50) Pierantoni, M.; Tenne, R.; Brumfeld, V.; Kiss, V.; Oron, D.; Addadi, L.; Weiner, S. Plants and Light Manipulation: The Integrated Mineral System in Okra Leaves. *Advanced Science (Weinh),* **2017,** *4* (5), 1600416.

(51) Sato, K.; Yamauchi, A.; Ozaki, N.; Ishigure, T.; Oaki, Y.; Imai, H. Optical properties of biosilicas in rice plants. *RSC Advances,* **2016,** *6* (110), 109168-109173.

(52) Hartley, S. E.; DeGabriel, J. L. The ecology of herbivore-induced silicon defences in grasses. *Functional Ecology,* **2016,** *30* (8), 1311-1322.

(53) Hartley, S. E.; Fitt, R. N.; McLarnon, E. L.; Wade, R. N. Defending the leaf surface: intra- and inter-specific differences in silicon deposition in grasses in response to damage and silicon supply. *Frontiers in Plant Science,* **2015,** *6* (35).

(54) Motomura, H.; Mita, N.; Suzuki, M. Silica Accumulation in Long-lived Leaves of Sasa veitchii (Carrière) Rehder (Poaceae–Bambusoideae). *Annals of Botany,* **2002,** *90* (1), 149-152.

(55) Belton, D.; Paine, G.; Patwardhan, S. V.; Perry, C. C. Towards an understanding of (bio)silicification: the role of amino acids and lysine oligomers in silicification. *Journal of Materials Chemistry,* **2004,** *14* (14), 2231-2241.

(56) Kumar, S.; Milstein, Y.; Brami, Y.; Elbaum, M.; Elbaum, R. Mechanism of silica deposition in sorghum silica cells. *New Phytologist,* **2016**.

(57) Markovich, O.; Kumar, S.; Cohen, D.; Addadi, S.; Fridman, E.; Elbaum, R. Silicification in Leaves of Sorghum Mutant with Low Silicon Accumulation. *Silicon,* **2015**, 1-7.

(58) Sangster, A. G.; Parry, D. W. Silica Deposition in the Grass Leaf in Relation to Transpiration and the Effect of Dinitrophenol. *Annals of Botany,* **1971,** *35* (3), 667-677.

(59) Kauss, H.; Seehaus, K.; Franke, R.; Gilbert, S.; Dietrich, R. A.; Kroger, N. Silica deposition by a strongly cationic proline-rich protein from systemically resistant cucumber plants. *The Plant Journal,* **2003,** *33* (1), 87-95.

(60) Harrison, C. C. Evidence for intramineral macromolecules containing protein from plant silicas. *Phytochemistry,* **1996,** *41*.

(61) Alexandre, A.; Basile-Doelsch, I.; Delhaye, T.; Borshneck, D.; Mazur, J. C.; Reyerson, P.; Santos, G. M. New highlights of phytolith structure and occluded carbon location: 3-D X-ray microscopy and NanoSIMS results. *Biogeosciences,* **2015,** *12* (3), 863-873.

(62) Kumar, S.; Adiram-Filiba, N.; Blum, S.; Sanchez-Lopez, J. A.; Tzfadia, O.; Omid, A.; Volpin, H.; Heifetz, Y.; Goobes, G.; Elbaum, R. Siliplant1 protein precipitates silica in sorghum silica cells. *Journal of Experimental Botany,* **2020**.

(63) Kröger, N.; Deutzmann, R.; Sumper, M. Polycationic Peptides from Diatom Biosilica That Direct Silica Nanosphere Formation. *Science,* **1999,** *286* (5442), 1129-1132.

(64) Kröger, N.; Lehmann, G.; Rachel, R.; Sumper, M. Characterization of a 200-kDa Diatom Protein that is Specifically Associated with a Silica-Based Substructure of the Cell Wall. *European Journal of Biochemistry,* **1997,** *250* (1), 99-105.

(65) Kröger, N.; Deutzmann, R.; Bergsdorf, C.; Sumper, M. Species-specific polyamines from diatoms control silica morphology. *Proceedings of the National Academy of Sciences,* **2000,** *97* (26), 14133-14138.

(66) Kröger, N.; Deutzmann, R.; Sumper, M. Silica-precipitating Peptides from Diatoms: THE CHEMICAL STRUCTURE OF SILAFFIN-1A FROM CYLINDROTHECA FUSIFORMIS. *Journal of Biological Chemistry,* **2001,** *276* (28), 26066-26070.

(67) Sumper, M.; Kroger, N. Silica formation in diatoms: the function of long-chain polyamines and silaffins. *Journal of Materials Chemistry,* **2004,** *14* (14), 2059-2065.

(68) Infrared and Raman Spectroscopy, Elsevier: **2018;** p 261-263.

(69) Mitani, N.; Ma, J. F.; Iwashita, T. Identification of the silicon form in xylem sap of rice (Oryza sativa L.). *Plant Cell Physiol,* **2005,** *46* (2), 279-83.

(70) Ma, J. F. Silicon transporters in higher plants. *Adv Exp Med Biol,* **2010,** *679*, 99-109.

(71) Ma, J. F.; Tamai, K.; Ichii, M.; Wu, G. F. A Rice Mutant Defective in Si Uptake. *Plant Physiology,* **2002,** *130* (4), 2111-2117.

(72) Ma, J. F.; Tamai, K.; Yamaji, N.; Mitani, N.; Konishi, S.; Katsuhara, M.; Ishiguro, M.; Murata, Y.; Yano, M. A silicon transporter in rice. *Nature,* **2006,** *440* (7084), 688-691.

(73) Perry, C. C.; Keeling-Tucker, T. Model studies of colloidal silica precipitation using biosilica extracts from Equisetum telmateia. *Colloid and Polymer Science,* **2003,** *281* (7), 652-664.

(74) Sapei, L.; Gierlinger, N.; Hartmann, J.; Noske, R.; Strauch, P.; Paris, O. Structural and analytical studies of silica accumulations in Equisetum hyemale. *Anal Bioanal Chem,* **2007,** *389* (4), 1249-57.

(75) Sapei, L.; Nöske, R.; Strauch, P.; Paris, O. Isolation of Mesoporous Biogenic Silica from the Perennial Plant Equisetum hyemale. *Chemistry of Materials,* **2008,** *20* (5), 2020-2025.

(76) Paterson, A. H.; Bowers, J. E.; Bruggmann, R.; Dubchak, I.; Grimwood, J.; Gundlach, H.; Haberer, G.; Hellsten, U.; Mitros, T.; Poliakov, A.; Schmutz, J.; Spannagl, M.; Tang, H.; Wang, X.; Wicker, T.; Bharti, A. K.; Chapman, J.; Feltus, F.

A.; Gowik, U.; Grigoriev, I. V.; Lyons, E.; Maher, C. A.; Martis, M.; Narechania, A.; Otillar, R. P.; Penning, B. W.; Salamov, A. A.; Wang, Y.; Zhang, L.; Carpita, N. C.; Freeling, M.; Gingle, A. R.; Hash, C. T.; Keller, B.; Klein, P.; Kresovich, S.; McCann, M. C.; Ming, R.; Peterson, D. G.; Mehboob ur, R.; Ware, D.; Westhoff, P.; Mayer, K. F. X.; Messing, J.; Rokhsar, D. S. The Sorghum bicolor genome and the diversification of grasses. *Nature,* **2009,** *457* (7229), 551-556.

(77) Reddy, B.; Are, A.; Reddy, S. Recent advances in sorghum improvement research at ICRISAT. *Kasetsart Journal (Natural Science),* **2010,** *44*, 499-506.

(78) Parr, J. F. A comparison of heavy liquid floatation and microwave digestion techniques for the extraction of fossil phytoliths from sediments. *Review of Palaeobotany and Palynology,* **2002,** *120* (3–4), 315-336.

(79) Parr, J. F.; Dolic, V.; Lancaster, G.; Boyd, W. E. A microwave digestion method for the extraction of phytoliths from herbarium specimens. *Review of Palaeobotany and Palynology,* **2001,** *116* (3–4), 203-212.

(80) Parr, J. F.; Sullivan, L. A. Comparison of two methods for the isolation of phytolith occluded carbon from plant material. *Plant and Soil,* **2014,** *374* (1), 45-53.

(81) Corbineau, R.; Reyerson, P. E.; Alexandre, A.; Santos, G. M. Towards producing pure phytolith concentrates from plants that are suitable for carbon isotopic analysis. *Review of Palaeobotany and Palynology,* **2013,** *197*, 179-185.

(82) Ravera, E.; Martelli, T.; Geiger, Y.; Fragai, M.; Goobes, G.; Luchinat, C. Biosilica and bioinspired silica studied by solid-state NMR. *Coordination Chemistry Reviews,* **2016,** *327-328*, 110-122.

(83) Bertermann, R.; Kröger, N.; Tacke, R. Solid-state 29Si MAS NMR studies of diatoms: structural characterization of biosilica deposits. *Analytical and Bioanalytical Chemistry,* **2003,** *375* (5), 630-634.

(84) Aguiar, H.; Serra, J.; González, P.; León, B. Structural study of sol–gel silicate glasses by IR and Raman spectroscopies. *Journal of Non-Crystalline Solids,* **2009,** *355* (8), 475-480.

(85) Dayanandan, P.; Kaufman, P. B.; Franklin, C. I. Detection of Silica in Plants. *American Journal of Botany,* **1983,** *70* (7), 1079-1084.

(86) Soukup, M.; Martinka, M.; Cigáň, M.; Ravaszová, F.; Lux, A. New method for visualization of silica phytoliths in Sorghum bicolor roots by fluorescence microscopy revealed silicate concentration-dependent phytolith formation. *Planta,* **2014,** *240* (6), 1365-1372.

(87) Perry, C. C.; Williams, R. J. P.; Fry, S. C. Cell Wall Biosynthesis during Silicification of Grass Hairs. *Journal of Plant Physiology,* **1987,** *126* (4), 437-448.

(88) Perry, C. C.; Mann, S.; Williams, R. J. P. Structural and analytical studies of the silicified macrohairs from the lemma of the grass *Phalaris canariensis. Proceedings of the Royal Society of London. Series B. Biological Sciences,* **1984,** *222* (1229), 427-438.

(89) Parker, F. S., Applications of infrared, Raman and Resonance Raman spectroscopy in biochemistry, Plenum Press: New York, **1984;** Vol. 128.

(90) Reddy, R. K.; Walsh, M. J.; Schulmerich, M. V.; Carney, P. S.; Bhargava, R. High-definition infrared spectroscopic imaging. *Applied spectroscopy,* **2013,** *67* (1), 93-105.

(91) Lasch, P. Spectral pre-processing for biomedical vibrational spectroscopy and microspectroscopic imaging. *Chemometrics and Intelligent Laboratory Systems,* **2012,** *117*, 100-114.

(92) Eilers, P.; Boelens, H. Baseline Correction with Asymmetric Least Squares Smoothing. *Unpublished Manuscript,* **2005**.

(93) Bonnier, F.; Byrne, H. Understanding the molecular information contained in principal component analysis of vibrational spectra of biological systems. *Analyst,* **2011,** *137*, 322-32.

(94) Reisner, L. A.; Cao, A.; Pandya, A. K. An integrated software system for processing, analyzing, and classifying Raman spectra. *Chemometrics and Intelligent Laboratory Systems,* **2011,** *105* (1), 83-90.

(95) Fröhlich, F. Deep-sea biogenic silica: new structural and analytical data from infrared analysis - geological implications. *Terra Nova,* **1989,** *1* (3), 267-273.

(96) Kačuráková, M.; Capek, P.; Sasinková, V.; Wellner, N.; Ebringerová, A. FT-IR study of plant cell wall model compounds: pectic polysaccharides and hemicelluloses. *Carbohydrate Polymers,* **2000,** *43* (2), 195-203.

(97) Gendron-Badou, A.; Coradin, T.; Maquet, J.; Fröhlich, F.; Livage, J. Spectroscopic characterization of biogenic silica. *Journal of Non-Crystalline Solids,* **2003,** *316* (2–3), 331-337.

(98) Kerr, J. L.; Baldwin, D. S.; Tobin, M. J.; Puskar, L.; Kappen, P.; Rees, G. N.; Silvester, E. High spatial resolution infrared micro-spectroscopy reveals the mechanism of leaf lignin decomposition by aquatic fungi. *PLoS One,* **2013,** *8* (4), e60857.

(99) Prats Mateu, B.; Hauser, M.-T.; Heredia, A.; Gierlinger, N. Waterproofing in Arabidopsis: Following Phenolics and Lipids In situ by Confocal Raman Microscopy. *Frontiers in Chemistry,* **2016,** *4*.

(100) Butler, H. J.; Ashton, L.; Bird, B.; Cinque, G.; Curtis, K.; Dorney, J.; Esmonde-White, K.; Fullwood, N. J.; Gardner, B.; Martin-Hirsch, P. L.; Walsh, M. J.; McAinsh, M. R.; Stone, N.; Martin, F. L. Using Raman spectroscopy to characterize biological materials. *Nature Protocols,* **2016,** *11* (4), 664-687.

(101) Yuan, P.; He, H. P.; Wu, D. Q.; Wang, D. Q.; Chen, L. J. Characterization of diatomaceous silica by Raman spectroscopy. *Spectrochimica Acta A,* **2004,** *60* (12), 2941-5.

(102) Lutz, M.; Breton, J. Chlorophyll associations in the chloroplast: Resonance raman spectroscopy. *Biochemical and Biophysical Research Communications,* **1973,** *53* (2), 413-418.

(103) Atalla, R. H.; Agarwal, U. Raman Microprobe Evidence for Lignin Orientation in the Cell Walls of Native Woody Tissue. *Science,* **1985,** *227* (4687), 636-638.

(104) Atalla, R. H.; Agarwal, U. Raman Microprobe Optimization and Sampling Technique for Studies of Plant Cell Walls, In *Microbeam Analysis*, **1984**.

(105) Agarwal, U.; Ralph, S. A.; Atalla, R. H., FT Raman Spectroscopic Study of Softwood Lignin, **1997**.

(106) Agarwal, U.; Ralph, S. Determination of ethylenic residues in wood and TMP of spruce by FT-Raman spectroscopy. *Holzforschung,* **2008,** *62* (6), 667-675.

(107) Agarwal, U. P. Raman imaging to investigate ultrastructure and composition of plant cell walls: distribution of lignin and cellulose in black spruce wood (*Picea mariana*). *Planta,* **2006,** *224* (5), 1141.

(108) Agarwal, U. P.; Atalla, R. H. Raman Spectroscopic Evidence for Coniferyl Alcohol Structures in Bleached and Sulfonated Mechanical Pulps. In *Photochemistry of Lignocellulosic Materials*, American Chemical Society: **1993**; Vol. 531, pp 26-44.

(109) Agarwal, U. P.; McSweeny, J. D.; Ralph, S. A. FT–Raman Investigation of Milled-Wood Lignins: Softwood, Hardwood, and Chemically Modified Black Spruce Lignins. *Journal of Wood Chemistry and Technology,* **2011,** *31* (4), 324-344.

(110) Gierlinger, N.; Schwanninger, M.; Reinecke, A.; Burgert, I. Molecular Changes during Tensile Deformation of Single Wood Fibers Followed by Raman Microscopy. *Biomacromolecules,* **2006,** *7* (7), 2077-2081.

(111) Agarwal, U. P.; Ralph, S. A.; Reiner, R. S.; Baez, C. New cellulose crystallinity estimation method that differentiates between organized and crystalline phases. *Carbohydrate Polymers,* **2018,** *190*, 262-270.

(112) Agarwal, U. P.; Ralph, S. A.; Reiner, R. S.; Baez, C. Probing crystallinity of never-dried wood cellulose with Raman spectroscopy. *Cellulose,* **2016,** *23* (1), 125-144.

(113) Agarwal, U. P.; Reiner, R. S.; Ralph, S. A. Cellulose I crystallinity determination using FT–Raman spectroscopy: univariate and multivariate methods. *Cellulose,* **2010,** *17* (4), 721-733.

(114) Agarwal, U.; Terashima, N. FT-Raman Study of Dehydrogenation Polymer (DHP) Lignins, In *12th ISWPC International Symposium on Wood and Pulping Chemistry*, Madison, Wisconsin USA, **2003**; Vol. 3.

(115) Agarwal, U.; Weinstock, I.; Atalla, R. H. FT-Raman Spectroscopy for Direct Measurement of Lignin Concentrations in Kraft Pulps. *Tappi Journal,* **2003**, 22-26.

(116) Stark, N.; Yelle, D.; Agarwal, U. Techniques for Characterizing Lignin. In *Lignin in Polymer Composites*, **2015**; pp 49-66.

(117) Diehn, S.; Zimmermann, B.; Tafintseva, V.; Seifert, S.; Bağcıoğlu, M.; Ohlson, M.; Weidner, S.; Fjellheim, S.; Kohler, A.; Kneipp, J. Combining Chemical Information From Grass Pollen in Multimodal Characterization. *Frontiers in Plant Science,* **2020,** *10* (1788).

(118) Zimmerman, B. A high-throughput FTIR spectroscopy approach to assess adaptive variation in the chemical composition of pollen. *Ecology and Evolution,* **2017,** *7*, 10839– 10849.

(119) Zimmerman, B.; Tafintseva, V.; Bagcioglu, M.; Hoegh Berdahl, M.; Kohler, A. Analysis of Allergenic Pollen by FTIR Microspectroscopy. *Analytical chemistry* **2016,** *88* (1), 803-11.

(120) Zimmermann, B. Characterization of Pollen by Vibrational Spectroscopy. *Applied Spectroscopy,* **2010,** *64* (12), 1364-1373.

(121) Zimmermann, B.; Kohler, A. Optimizing Savitzky-Golay parameters for improving spectral resolution and quantification in infrared spectroscopy. *Applied Spectroscopy,* **2013,** *67* (8), 892-902.

(122) Schulz, H.; Baranska, M. Identification and quantification of valuable plant substances by IR and Raman spectroscopy. *Vibrational Spectroscopy,* **2007,** *43* (1), 13-25.

(123) Knoll, B.; Keilmann, F. Near-field probing of vibrational absorption for chemical microscopy. *Nature,* **1999,** *399*, 134.

(124) Huber, A. J.; Keilmann, F.; Wittborn, J.; Aizpurua, J.; Hillenbrand, R. Terahertz Near-Field Nanoscopy of Mobile Carriers in Single Semiconductor Nanodevices. *Nano Letters,* **2008,** *8* (11), 3766-3770.

(125) Khatib, O.; Bechtel, H. A.; Martin, M. C.; Raschke, M. B.; Carr, G. L. Far Infrared Synchrotron Near-Field Nanoimaging and Nanospectroscopy. *ACS Photonics,* **2018,** *5* (7), 2773-2779.

(126) Autore, M.; Mester, L.; Goikoetxea, M.; Hillenbrand, R. Substrate Matters: Surface-Polariton Enhanced Infrared Nanospectroscopy of Molecular Vibrations. *Nano Letters,* **2019,** *19* (11), 8066-8073.

(127) Huth, F.; Govyadinov, A.; Amarie, S.; Nuansing, W.; Keilmann, F.; Hillenbrand, R. Nano-FTIR Absorption Spectroscopy of Molecular Fingerprints at 20 nm Spatial Resolution. *Nano Letters,* **2012,** *12* (8), 3973-3978.

(128) Keilmann, F.; Hillenbrand, R. Near-field microscopy by elastic light scattering from a tip. *Philos Trans A Math Phys Eng Sci,* **2004,** *362* (1817), 787-805.

(129) Hillenbrand, R.; Keilmann, F. Complex Optical Constants on a Subwavelength Scale. *Physical Review Letters,* **2000,** *85* (14), 3029-3032.

(130) Tamayo, J.; García, R. Deformation, Contact Time, and Phase Contrast in Tapping Mode Scanning Force Microscopy. *Langmuir,* **1996,** *12* (18), 4430-4435.

(131) Madella, M.; Alexandre, A.; Ball, T. International code for phytolith nomenclature 1.0. *Annals of botany,* **2005,** *96* (2), 253-260.

(132) Hodson, M. J. The Relative Importance of Cell Wall and Lumen Phytoliths in Carbon Sequestration in Soil: A Hypothesis. *Frontiers in Earth Science,* **2019,** *7* (167).

(133) Watling, K. M.; Parr, J. F.; Rintoul, L.; Brown, C. L.; Sullivan, L. A. Raman, infrared and XPS study of bamboo phytoliths after chemical digestion. *Spectrochimica Acta Part A: Molecular and Biomolecular Spectroscopy,* **2011,** *80* (1), 106-111.

(134) Cabanes, D.; Shahack-Gross, R. Understanding Fossil Phytolith Preservation: The Role of Partial Dissolution in Paleoecology and Archaeology. *PLOS ONE,* **2015,** *10* (5), e0125532.

(135) Gallagher, K. L.; Alfonso-Garcia, A.; Sanchez, J.; Potma, E. O.; Santos, G. M. Plant growth conditions alter phytolith carbon. *Frontiers in plant science,* **2015,** *6*, 753.

(136) Perry, C. C.; Moss, E. J.; Williams, R. J. P.; Clarke, B. C. A staining agent for biological silica. *Proceedings of the Royal Society of London. Series B: Biological Sciences,* **1990,** *241* (1300), 47-50.

(137) Mitani, N.; Ma, J. F. Uptake system of silicon in different plant species. *Journal of Experimental Botany,* **2005,** *56* (414), 1255-1261.

(138) Sakurai, G.; Satake, A.; Yamaji, N.; Mitani-Ueno, N.; Yokozawa, M.; Feugier, F. In Silico Simulation Modeling Reveals the Importance of the Casparian Strip for Efficient Silicon Uptake in Rice Roots. *Plant & cell physiology,* **2015,** *56*.

(139) Perry, C. C. Silicification: The Processes by Which Organisms Capture and Mineralize Silica. *Reviews in Mineralogy and Geochemistry,* **2003,** *54* (1), 291-327.

(140) Wang, M.; Gao, L.; Dong, S.; Sun, Y.; Shen, Q.; Guo, S. Role of Silicon on Plant–Pathogen Interactions. *Frontiers in Plant Science,* **2017,** *8* (701).

(141) Hamdan, H.; Muhid, M. N. M.; Endud, S.; Listiorini, E.; Ramli, Z. 29Si MAS NMR, XRD and FESEM studies of rice husk silica for the synthesis of zeolites. *Journal of Non-Crystalline Solids,* **1997,** *211* (1), 126-131.

(142) Mueller, R.; Kammler, H. K.; Wegner, K.; Pratsinis, S. E. OH Surface Density of SiO2 and TiO2 by Thermogravimetric Analysis. *Langmuir,* **2003,** *19* (1), 160-165.

(143) Sharma, S. K.; Mammone, J. F.; Nicol, M. F. Raman investigation of ring configurations in vitreous silica. *Nature,* **1981,** *292* (5819), 140-141.

(144) Bertoluzza, A.; Fagnano, C.; Antonietta Morelli, M.; Gottardi, V.; Guglielmi, M. Raman and infrared spectra on silica gel evolving toward glass. *Journal of Non-Crystalline Solids,* **1982,** *48* (1), 117-128.

(145) Ram, M. S.; Dowell, F.; Seitz, L. FT-Raman Spectra of Unsoaked and NaOH-Soaked Wheat Kernels, Bran, and Ferulic Acid. *Cereal Chemistry,* **2003,** *80*.

(146) Bock, P.; Nousiainen, P.; Elder, T.; Blaukopf, M.; Amer, H.; Zirbs, R.; Potthast, A.; Gierlinger, N. Infrared and Raman spectra of lignin substructures: Dibenzodioxocin. *Journal of Raman Spectroscopy,* **2020**.

(147) Kirk, C. T. Quantitative analysis of the effect of disorder-induced mode coupling on infrared absorption in silica. *Physical Review B,* **1988,** *38* (2), 1255-1273.

(148) Humbert, B. Estimation of hydroxyl density at the surface of pyrogenic silicas by complementary NMR and raman experiments. *Journal of Non-Crystalline Solids,* **1995,** *191* (1), 29-37.

(149) Silverstein, R. M.; Webster, F. X.; Kiemle, D. J., Spectrometric Identification of Organic Compounds, 7th ed.; John Wiley & Sons: Hoboken, NJ, **2005**.

(150) Nguyen, M. N.; Meharg, A. A.; Carey, M.; Dultz, S.; Marone, F.; Cichy, S. B.; Tran, C. T.; Le, G. H.; Mai, N. T.; Nguyen, T. T. H. Fern, Dicranopteris linearis, derived

phytoliths in soil: Morphotypes, solubility and content in relation to soil properties. *European Journal of Soil Science,* **2019,** *70* (3), 507-517.

(151) Sato, K.; Ozaki, N.; Nakanishi, K.; Sugahara, Y.; Oaki, Y.; Salinas, C.; Herrera, S.; Kisailus, D.; Imai, H. Effects of nanostructured biosilica on rice plant mechanics. *RSC Advances,* **2017,** *7* (22), 13065-13071.

(152) Lazaro, A.; van de Griend, M. C.; Brouwers, H. J. H.; Geus, J. W. The influence of process conditions and Ostwald ripening on the specific surface area of olivine nano-silica. *Microporous and Mesoporous Materials,* **2013,** *181*, 254-261.

(153) Fry, S. C.; Nesselrode, B. H.; Miller, J. G.; Mewburn, B. R. Mixed-linkage (1-->3,1-->4)-beta-D-glucan is a major hemicellulose of Equisetum (horsetail) cell walls. *New Phytologist,* **2008,** *179* (1), 104-15.

(154) Law, C.; Exley, C. New insight into silica deposition in horsetail (*Equisetum arvense*). *BMC Plant Biology,* **2011,** *11* (1), 112.

(155) Soukup, M.; Martinka, M.; Bosnic, D.; Caplovicova, M.; Elbaum, R.; Lux, A. Formation of silica aggregates in sorghum root endodermis is predetermined by cell wall architecture and development. *Annals of Botany* **2017**.

(156) Kulich, I.; Vojtíková, Z.; Sabol, P.; Ortmannová, J.; Neděla, V.; Tihlaříková, E.; Žárský, V. Exocyst Subunit EXO70H4 Has a Specific Role in Callose Synthase Secretion and Silica Accumulation. *Plant Physiology,* **2018,** *176* (3), 2040-2051.

(157) Guerriero, G.; Stokes, I.; Exley, C. Is callose required for silicification in plants? *Biology Letters,* **2018,** *14* (10), 20180338.

(158) Van Opdenbosch, D.; Fritz-Popovski, G.; Paris, O.; Zollfrank, C. Silica replication of the hierarchical structure of wood with nanometer precision. *Journal of Materials Research,* **2011,** *26* (10), 1193-1202.

(159) Van Opdenbosch, D.; Zollfrank, C. Cellulose-Based Biotemplated Silica Structuring. *Advanced Engineering Materials,* **2014,** *16* (6), 699-712.

(160) Meunier, J. D.; Barboni, D.; Anwar-Ul-Haq, M.; Levard, C.; Chaurand, P.; Vidal, V.; Grauby, O.; Huc, R.; Laffont-Schwob, I.; Rabier, J.; Keller, C. Effect of phytoliths for mitigating water stress in durum wheat. *New Phytologist,* **2017,** *215* (1), 229-239.

(161) Elbaum, R.; Melamed-Bessudo, C.; Tuross, N.; Levy, A. A.; Weiner, S. New methods to isolate organic materials from silicified phytoliths reveal fragmented glycoproteins but no DNA. *Quaternary International,* **2009,** *193* (1–2), 11-19.

(162) Fulcher, R. G.; O'Brien, T. P.; Lee, J. W. Studies on the Aleurone Layer I. Oonventional and Fluorescence Microscopy of the Cell Wall With Emphasis on Phenol-Carbohydrate Complexes in Wheat. *Australian Journal of Biological Sciences,* **1972,** *25* (1), 23-34.

(163) Lawton, J. R. Observations on the structure of epidermal cells, particularly the cork and silica cells, from the flowering stem internode of Lolium temulentum L. (Gramineae). *Botanical Journal of the Linnean Society,* **1980,** *80* (2), 161-177.

(164) Lichtenthaler, H. K.; Schweiger, J. Cell wall bound ferulic acid, the major substance of the blue-green fluorescence emission of plants. *Journal of Plant Physiology,* **1998,** *152* (2), 272-282.

(165) Notburga Gierlinger , a. S. The potential of Raman microscopy and Raman imaging in plant research. *Spectroscopy,* **2007,** *21*.

(166) Siesler, R. S. H. W., Infrared and Raman Spectroscopic Imaging, Wiley-VCH Verlag & Co. KGaA: Weinheim, Germany, **2014**.

(167) Prats Mateu, B.; Felhofer, M.; De Juan, A.; Gierlinger, N. Multivariate unmixing approaches on Raman images of plant cell walls: New insights or overinterpretation of results? *Plant Methods,* **2018,** *14*.

(168) Larsen, K. L.; Barsberg, S. Theoretical and Raman Spectroscopic Studies of Phenolic Lignin Model Monomers. *The Journal of Physical Chemistry B,* **2010,** *114* (23), 8009-8021.

(169) Bock, P.; Gierlinger, N. Infrared and Raman spectra of lignin substructures: Coniferyl alcohol, abietin, and coniferyl aldehyde. *Journal of Raman Spectroscopy,* **2019,** *50*.

(170) Agarwal, U.; Reiner, R. S.; Pandey, A.; Ralph, S. A.; Hirth, K.; Atalla, R. H. Raman Spectra of Lignin Model Compounds, In *Appita Annual Conference*, **2005**; Vol. 3.

(171) Chu, L.-Q.; Masyuko, R.; Sweedler, J. V.; Bohn, P. W. Base-induced delignification of *miscanthus x giganteus* studied by three-dimensional confocal raman imaging. *Bioresource Technology,* **2010,** *101* (13), 4919-4925.

(172) Shlens, J. A Tutorial on Principal Component Analysis. *Educational,* **2014,** *51*.

(173) Agarwal, U. P.; Atalla, R. Vibrational spectroscopy. In *Lignin and Lignans: Advances in Chemistry*, **2010**; pp 103-136.

(174) Saariaho, A.-M.; Jääskeläinen, A.-S.; Nuopponen, M.; Vuorinen, T. Ultra Violet Resonance Raman Spectroscopy in Lignin Analysis: Determination of Characteristic

Vibrations of p-Hydroxyphenyl, Guaiacyl, and Syringyl Lignin Structures. *Applied Spectroscopy,* **2003,** *57* (1), 58-66.

(175) Agarwal, U. P. Analysis of Cellulose and Lignocellulose Materials by Raman Spectroscopy: A Review of the Current Status. *Molecules,* **2019,** *24* (9), 1659.

(176) Sun, L.; Simmons, B. A.; Singh, S. Understanding tissue specific compositions of bioenergy feedstocks through hyperspectral Raman imaging. *Biotechnology and Bioengineering,* **2011,** *108* (2), 286-295.

(177) Lupoi, J.; Singh, S.; Davis, M.; Lee, D.; Shepherd, M.; Simmons, B.; Henry, R. High-throughput prediction of eucalypt lignin syringyl/guaiacyl content using multivariate analysis: A comparison between mid-infrared, near-infrared, and Raman spectroscopies for model development. *Biotechnology for biofuels,* **2014,** *7*, 93.

(178) Schulte, F.; Mader, J.; Kroh, L. W.; Panne, U.; Kneipp, J. Characterization of pollen carotenoids with in situ and high-performance thin-layer chromatography supported resonant Raman spectroscopy. *Analytical Chemistry,* **2009,** *81* (20), 8426-33.

(179) Yu, M. M. L.; Schulze, H. G.; Jetter, R.; Blades, M. W.; Turner, R. F. B. Raman Microspectroscopic Analysis of Triterpenoids Found in Plant Cuticles. *Applied Spectroscopy,* **2007,** *61* (1), 32-37.

(180) Robert, P.; Marquis, M.; Barron, C.; Guillon, F.; Saulnier, L. FT-IR Investigation of Cell Wall Polysaccharides from Cereal Grains. Arabinoxylan Infrared Assignment. *Journal of Agricultural and Food Chemistry,* **2005,** *53* (18), 7014-7018.

(181) Bandekar, J. Amide modes and protein conformation. *Biochimica et Biophysica Acta (BBA) - Protein Structure and Molecular Enzymology,* **1992,** *1120* (2), 123-143.

(182) Faix, O. Classification of Lignins from Different Botanical Origins by FT-IR Spectroscopy. *Holzforschung - International Journal of the Biology, Chemistry, Physics and Technology of Wood,* **1991,** *45* (s1), 21.

(183) Makarem, M.; Lee, C. M.; Kafle, K.; Huang, S.; Chae, I.; Yang, H.; Kubicki, J. D.; Kim, S. H. Probing cellulose structures with vibrational spectroscopy. *Cellulose,* **2019,** *26* (1), 35-79.

(184) Lupoi, J. S.; Singh, S.; Parthasarathi, R.; Simmons, B. A.; Henry, R. J. Recent innovations in analytical methods for the qualitative and quantitative assessment of lignin. *Renewable and Sustainable Energy Reviews,* **2015,** *49*, 871-906.

(185) Agarwal, U. P. 1064 nm FT-Raman spectroscopy for investigations of plant cell walls and other biomass materials. *Frontiers in Plant Science,* **2014,** *5*, 490.

(186) Hanninen, T.; Kontturi, E.; Vuorinen, T. Distribution of lignin and its coniferyl alcohol and coniferyl aldehyde groups in Picea abies and Pinus sylvestris as observed by Raman imaging. *Phytochemistry,* **2011,** *72* (14-15), 1889-95.

(187) Barsberg, S.; Matousek, P.; Towrie, M.; Jørgensen, H.; Felby, C. Lignin Radicals in the Plant Cell Wall Probed by Kerr-Gated Resonance Raman Spectroscopy. *Biophysical Journal,* **2006,** *90* (8), 2978-2986.

(188) Borowska-Wykręt, D.; Dulski, M. Raman Spectroscopy in Nonwoody Plants. In *Plant Cell Morphogenesis: Methods and Protocols*, Cvrčková, F.; Žárský, V., Eds. Springer New York: New York, NY, **2019**; pp 83-107.

(189) Heitner, C.; Dimmel, D.; Schmidt, J., Lignin and Lignans: Advances in Chemistry, CRC Press: **2016**.

(190) Sene, C.; McCann, M. C.; Wilson, R. H.; Grinter, R. Fourier-Transform Raman and Fourier-Transform Infrared Spectroscopy (An Investigation of Five Higher Plant Cell Walls and Their Components). *Plant Physiology,* **1994,** *106* (4), 1623-1631.

(191) Ha, M.-A.; MacKinnon, I. M.; Šturcová, A.; Apperley, D. C.; McCann, M. C.; Turner, S. R.; Jarvis, M. C. Structure of cellulose-deficient secondary cell walls from the irx3 mutant of Arabidopsis thaliana. *Phytochemistry,* **2002,** *61* (1), 7-14.

(192) Yoshino, H.; Kamiya, K.; Nasu, H. IR study on the structural evolution of sol-gel derived SiO2 gels in the early stage of conversion to glasses. *Journal of Non-Crystalline Solids,* **1990,** *126* (1), 68-78.

(193) Gunde, M. K. Vibrational modes in amorphous silicon dioxide. *Physica B: Condensed Matter,* **2000,** *292* (3), 286-295.

(194) Nascimento, J.; Bioucas-Dias, J. Vertex component analysis: A fast algorithm to unmix hyperspectral data. *IEEE T. Geoscience and Remote Sensing,* **2005,** *43*, 898-910.

(195) Yu, P. Application of cluster analysis (CLA) in feed chemical imaging to accurately reveal structural-chemical features of feeds and plants within cellular dimension. *Journal of agricultural and food chemistry,* **2005,** *53* (8), 2872-80.

(196) Chester, G. M.; Paul, R. N. The Involvement of Cork-Silica Cell Pairs in the Production of Wax Filaments in Johnsongrass (Sorghum halepense) Leaves. *Weed Science,* **1989,** *37* (3), 458-470.

(197) Jenks, M. A.; Rich, P. J.; Ashworth, E. N. Involvement of Cork Cells in the Secretion of Epicuticular Wax Filaments on Sorghum bicolor (L.) Moench. *International Journal of Plant Sciences,* **1994,** *155* (5), 506-518.

(198) Espelie, K. E.; Kolattukudy, P. E. Composition of the Aliphatic Components of Suberin of the Endodermal Fraction from the First Internode of Etiolated Sorghum Seedlings. *Plant Physiology,* **1979,** *63* (3), 433-435.

(199) Pelletier, M. J. Quantitative Analysis Using Raman Spectrometry. *Applied Spectroscopy,* **2003,** *57* (1), 20A-42A.

(200) O'Grady, A.; Dennis, A.; Denvir, D.; McGarvey, J.; Bell, S. Quantitative Raman Spectroscopy of Highly Fluorescent Samples Using Pseudosecond Derivatives and Multivariate Analysis. *Analytical chemistry,* **2001,** *73*, 2058-65.

(201) Albinsson, B.; Li, S.; Lundquist, K.; Stomberg, R. The origin of lignin fluorescence. *Journal of Molecular Structure,* **1999,** *508* (1), 19-27.

(202) Olmstead, J. A.; Gray, D. G. Fluorescence Spectroscopy of Cellulose, Lignin and Mechanical Pulps: A Review. *Journal of Pulp and Paper Science,* **1997,** *23* (12), J571-J581.

(203) Djikanović, D.; Kalauzi, A.; Radotić, K.; Lapierre, C.; Jeremić, M. Deconvolution of lignin fluorescence spectra: A contribution to the comparative structural studies of lignins. *Russian Journal of Physical Chemistry A,* **2007,** *81* (9), 1425-1428.

(204) Lähdetie, A.; Nousiainen, P.; Sipilä, J.; Tamminen, T.; Jääskeläinen, A.-S. Laser-induced fluorescence (LIF) of lignin and lignin model compounds in Raman spectroscopy. *Holzforschung,* **2013,** *67* (5), 531.

(205) Zexer, N.; Elbaum, R. Unique lignin modifications pattern the nucleation of silica in sorghum endodermis. *Journal of Experimental Botany,* **2020**.

(206) Elbaum, R.; Zaltzman, L.; Burgert, I.; Fratzl, P. The role of wheat awns in the seed dispersal unit. *Science,* **2007,** *316* (5826), 884-6.

(207) Gal, A.; Hirsch, A.; Siegel, S.; Li, C.; Aichmayer, B.; Politi, Y.; Fratzl, P.; Weiner, S.; Addadi, L. Plant cystoliths: a complex functional biocomposite of four distinct silica and amorphous calcium carbonate phases. *Chemistry,* **2012,** *18* (33), 10262-70.

(208) Gierlinger, N.; Goswami, L.; Schmidt, M.; Burgert, I.; Coutand, C.; Rogge, T.; Schwanninger, M. In Situ FT-IR Microscopic Study on Enzymatic Treatment of Poplar Wood Cross-Sections. *Biomacromolecules,* **2008,** *9* (8), 2194-2201.

(209) Heraud, P.; Caine, S.; Sanson, G.; Gleadow, R.; Wood, B. R.; McNaughton, D. Focal plane array infrared imaging: a new way to analyse leaf tissue. *New Phytologist,* **2007,** *173* (1), 216-25.

(210) Cao, C.; Yang, Z.; Han, L.; Jiang, X.; Ji, G. Study on in situ analysis of cellulose, hemicelluloses and lignin distribution linked to tissue structure of crop stalk internodal transverse section based on FTIR microspectroscopic imaging. *Cellulose,* **2014,** *22*, 139-149.

(211) Harris, C. W.; Silvester, E.; Rees, G. N.; Pengelly, J.; Puskar, L. Proteins are a major component of dissolved organic nitrogen (DON) leached from terrestrially aged *Eucalyptus camaldulensis* leaves. *Environmental Chemistry,* **2016,** *13* (5), 877-887.

(212) Farber, C.; Wang, R.; Chemelewski, R.; Mullet, J.; Kurouski, D. Nanoscale Structural Organization of Plant Epicuticular Wax Probed by Atomic Force Microscope Infrared Spectroscopy. *Analytical Chemistry,* **2019,** *91* (3), 2472-2479.

(213) Abraham, Y.; Elbaum, R. Quantification of microfibril angle in secondary cell walls at subcellular resolution by means of polarized light microscopy. *New Phytologist,* **2013,** *197* (3), 1012-1019.

(214) Keplinger, T.; Konnerth, J.; Aguié-Béghin, V.; Rüggeberg, M.; Gierlinger, N.; Burgert, I. A zoom into the nanoscale texture of secondary cell walls. *Plant Methods,* **2014,** *10* (1), 1.

(215) Bokor, B.; Soukup, M.; Vaculík, M.; Vd'ačný, P.; Weidinger, M.; Lichtscheidl, I.; Vávrová, S.; Šoltys, K.; Sonah, H.; Deshmukh, R.; Bélanger, R. R.; White, P. J.; El-Serehy, H. A.; Lux, A. Silicon Uptake and Localisation in Date Palm (*Phoenix dactylifera*) – A Unique Association With Sclerenchyma. *Frontiers in Plant Science,* **2019,** *10* (988).

(216) Ugarte, L.; Santamaria-Echart, A.; Mastel, S.; Autore, M.; Hillenbrand, R.; Corcuera, M. A.; Eceiza, A. An alternative approach for the incorporation of cellulose nanocrystals in flexible polyurethane foams based on renewably sourced polyols. *Industrial Crops and Products,* **2017,** *95*, 564-573.

(217) Paulite, M.; Fakhraai, Z.; Li, I. T. S.; Gunari, N.; Tanur, A. E.; Walker, G. C. Imaging Secondary Structure of Individual Amyloid Fibrils of a β2-Microglobulin Fragment Using Near-Field Infrared Spectroscopy. *Journal of the American Chemical Society,* **2011,** *133* (19), 7376-7383.

(218) Brehm, M.; Taubner, T.; Hillenbrand, R.; Keilmann, F. Infrared Spectroscopic Mapping of Single Nanoparticles and Viruses at Nanoscale Resolution. *Nano Letters,* **2006,** *6* (7), 1307-1310.

(219) Amenabar, I.; Poly, S.; Goikoetxea, M.; Nuansing, W.; Lasch, P.; Hillenbrand, R. Hyperspectral infrared nanoimaging of organic samples based on Fourier transform infrared nanospectroscopy. *Nature Communications,* **2017,** *8*, 14402.

(220) Amenabar, I.; Poly, S.; Nuansing, W.; Hubrich, E. H.; Govyadinov, A. A.; Huth, F.; Krutokhvostov, R.; Zhang, L.; Knez, M.; Heberle, J.; Bittner, A. M.; Hillenbrand, R. Structural analysis and mapping of individual protein complexes by infrared nanospectroscopy. *Nature Communications,* **2013,** *4*, 2890.

(221) Amarie, S.; Zaslansky, P.; Kajihara, Y.; Griesshaber, E.; Schmahl, W. W.; Keilmann, F. Nano-FTIR chemical mapping of minerals in biological materials. *Beilstein J Nanotechnol,* **2012,** *3*, 312-23.

(222) Bechtel, H. A.; Muller, E. A.; Olmon, R. L.; Martin, M. C.; Raschke, M. B. Ultrabroadband infrared nanospectroscopic imaging. *Proceedings of the National Academy of Sciences,* **2014,** *111* (20), 7191-7196.

(223) Pereira, L.; Flores-Borges, D. N. A.; Bittencourt, P. R. L.; Mayer, J. L. S.; Kiyota, E.; Araújo, P.; Jansen, S.; Freitas, R. O.; Oliveira, R. S.; Mazzafera, P. Infrared Nanospectroscopy Reveals the Chemical Nature of Pit Membranes in Water-Conducting Cells of the Plant Xylem. *Plant Physiology,* **2018,** *177* (4), 1629-1638.

(224) Landreau, X.; Lanfant, B.; Merle, T.; Dublanche-Tixier, C.; Tristant, P. A thorough FT-IR spectroscopy study on micrometric silicon oxide films deposited by atmospheric pressure microwave plasma torch. *The European Physical Journal,* **2012,** *66* (6).

(225) Huber, A. J.; Wittborn, J.; Hillenbrand, R. Infrared spectroscopic near-field mapping of single nanotransistors. *Nanotechnology,* **2010,** *21* (23), 235702.

(226) Hillenbrand, R.; Taubner, T.; Keilmann, F. Phonon-enhanced light–matter interaction at the nanometre scale. *Nature,* **2002,** *418*, 159.

(227) Amarie, S.; Keilmann, F. Broadband-infrared assessment of phonon resonance in scattering-type near-field microscopy. *Physical Review B,* **2011,** *83* (4), 045404.

(228) Peleg, Z.; Saranga, Y.; Fahima, T.; Aharoni, A.; Elbaum, R. Genetic control over silica deposition in wheat awns. *Physiologia Plantarum,* **2010,** *140* (1), 10-20.

(229) (1-2) Marchessault, R. H. Application of infra-red spectroscopy to cellulose and wood polysaccharides, In *Pure and Applied Chemistry*, **1962**; Vol. 5, p 107.

(230) Magonov, S. N.; Reneker, D. H. Characterization of polymer surfaces with atomic force microscopy. *Annual Review of Materials Science,* **1997,** *27* (1), 175-222.

(231) Elbaum, R.; Gorb, S.; Fratzl, P. Structures in the cell wall that enable hygroscopic movement of wheat awns. *J Struct Biol,* **2008,** *164* (1), 101-7.

(232) Hattori, T.; Inanaga, S.; Tanimoto, E.; Lux, A.; Luxová, M.; Sugimoto, Y. Silicon-Induced Changes in Viscoelastic Properties of Sorghum Root Cell Walls. *Plant and Cell Physiology,* **2003,** *44* (7), 743-749.

(233) Fleck, A. T.; Nye, T.; Repenning, C.; Stahl, F.; Zahn, M.; Schenk, M. K. Silicon enhances suberization and lignification in roots of rice (Oryza sativa). *Journal of Experimental Botany,* **2011,** *62* (6), 2001-2011.

(234) Inanaga, S.; Okasaka, A. Calcium and silicon binding compounds in cell walls of rice shoots. *Soil Science and Plant Nutrition,* **1995,** *41* (1), 103-110.

(235) Inanaga, S.; Okasaka, A.; Tanaka, S. Does silicon exist in association with organic compounds in rice plant? *Soil Science and Plant Nutrition,* **1995,** *41* (1), 111-117.

(236) Fang, J. Y.; Ma, X. L. In vitro simulation studies of silica deposition induced by lignin from rice. *Journal of Zhejiang University Science B,* **2006,** *7* (4), 267-71.

(237) Suzuki, S.; Ma, J. F.; Yamamoto, N.; Hattori, T.; Masahiro, S.; Umezawa, T. Silicon deficiency promotes lignin accumulation in rice. *Plant Biotechnology,* **2012,** *29*, 391-394.

(238) Zhang, C.; Wang, L.; Zhang, W.; Zhang, F. Do lignification and silicification of the cell wall precede silicon deposition in the silica cell of the rice (*Oryza sativa L.*) leaf epidermis? *Plant and Soil,* **2013,** *372* (1), 137-149.

(239) Fleck, A. T.; Schulze, S.; Hinrichs, M.; Specht, A.; Waßmann, F.; Schreiber, L.; Schenk, M. K. Silicon Promotes Exodermal Casparian Band Formation in Si-Accumulating and Si-Excluding Species by Forming Phenol Complexes. *PLoS One,* **2015,** *10* (9), e0138555.

(240) Klotzbücher, T.; Klotzbücher, A.; Kaiser, K.; Vetterlein, D.; Jahn, R.; Mikutta, R. Variable silicon accumulation in plants affects terrestrial carbon cycling by controlling lignin synthesis. *Global Change Biology,* **2017,** *24* (1), e183-e189.

(241) George, N.; Antony, A.; Ramachandran, T.; Hamed, F.; Kamal-Eldin, A. Microscopic Investigations of Silicification and Lignification Suggest Their Coexistence in Tracheary Phytoliths in Date Fruits (*Phoenix dactylifera L.*). *Frontiers in Plant Science,* **2020,** *11* (977).

(242) Barros, J.; Serk, H.; Granlund, I.; Pesquet, E. The cell biology of lignification in higher plants. *Annals of Botany,* **2015,** *115* (7), 1053-74.

(243) Ralph, J.; Kim, H.; Lu, F.; Grabber, J. H.; Leple, J. C.; Berrio-Sierra, J.; Derikvand, M. M.; Jouanin, L.; Boerjan, W.; Lapierre, C. Identification of the structure and origin of a thioacidolysis marker compound for ferulic acid incorporation into

angiosperm lignins (and an indicator for cinnamoyl CoA reductase deficiency). *Plant Journal,* **2008,** *53* (2), 368-79.

(244) Casey, W. H.; Kinrade, S. D.; Knight, C. T. G.; Rains, D. W.; Epstein, E. Aqueous silicate complexes in wheat, Triticum aestivum L. *Plant, Cell & Environment,* **2004,** *27* (1), 51-54.

(245) Wood, D. L.; Rabinovich, E. M. Study of Alkoxide Silica Gels by Infrared Spectroscopy. *Applied Spectroscopy,* **1989,** *43* (2), 263-267.

(246) Fang, J.; Wang, H.; Chen, Y.; Zhang, F. Silica nanospheres formation induced by peroxidase-catalyzed phenol polymerization. *Progress in Natural Science,* **2003,** *13* (7), 501-504.

(247) Tuma, R. Raman spectroscopy of proteins: from peptides to large assemblies. *Journal of Raman Spectroscopy,* **2005,** *36* (4), 307-319.

(248) Soukup, M.; Rodriguez Zancajo, V. M.; Kneipp, J.; Elbaum, R. Formation of root silica aggregates in sorghum is an active process of the endodermis. *Journal of Experimental Botany,* **2019**.

(249) Carver, T. L. W.; Robbins, M. P.; Thomas, B. J.; Troth, K.; Raistrick, N.; Zeyen, R. J. Silicon deprivation enhances localized autofluorescent responses and phenylalanine ammonia-lyase activity in oat attacked by *Blumeria graminis. Physiological and Molecular Plant Pathology,* **1998,** *52* (4), 245-257.

(250) Carver, T. L. W.; Thomas, B. J.; Robbins, M. P.; Zeyen, R. J. Phenylalanine ammonia-lyase inhibition, autofluorescence, and localized accumulation of silicon, calcium and manganese in oat epidermis attacked by the powdery mildew fungus *Blumeria graminis* (DC) Speer. *Physiological and Molecular Plant Pathology,* **1998,** *52* (4), 223-243.

(251) Zhang, J.; Zou, W.; Li, Y.; Feng, Y.; Zhang, H.; Wu, Z.; Tu, Y.; Wang, Y.; Cai, X.; Peng, L. Silica distinctively affects cell wall features and lignocellulosic saccharification with large enhancement on biomass production in rice. *Plant Science,* **2015,** *239*, 84-91.

(252) Cabrera, Y.; Cabrera, A.; Larsen Flemming, H.; Felby, C. Solid-state 29Si NMR and FTIR analyses of lignin-silica coprecipitates. *Holzforschung,* **2016,** *70* (8), 709.

List of abbreviations

AFM	Atomic force microscopy
AsLS	Asymmetric Least Squares Smoothing
CP	Cross polarization
DP	Direct polarization
DFT	Density functional theory
DTG	Differential thermal gravimetric
DHPs	Dehydrogenation polymers
EDX	Energy dispersive X-ray spectroscopy
EMSC	Extended multiplicative signal correction
ESEM	Environmental scanning electron microscopy
FAA	Formaldehyde, acetic acid and ethanol
FTIR	Fourier-transform infrared
HCA	Hierarchical cluster analysis
ICP-MS	Inductively coupled plasma mass spectrometry
LIF	Laser induced fluorescence
MAD	Microwave-assisted digestion
MAS	Magic angle spinning
MCR	Multivariate curve resolution–alternating least squares
MS	mass spectrometry
PCA	Principal component analysis
Si	Silicon
s-SNOM	Scattering-type near-field optical microscope
SONE	$H_2SO_4/H_2O_2/HNO_3$ extraction
SS-NMR	Solid-state ^{29}Si Nuclear magnetic resonance
TEM	Transmission electron microscopy
VCA	vertex component analysis
XRD	X-Ray diffraction

List of Figures

Figure 4.1: Scanning electron micrographs of sorghum leaves demonstrating typical silica deposition. 29

Figure 4.2: Solid State Magic Angle Spinning Nuclear Magnetic Resonance (SS-MAS-NMR) of 29Si atoms in leaf silica extracted by SONE and MAD. 31

Figure 4.3: Diffractogram of sorghum phytoliths extracted by MAD in red, and SONE in black. 32

Figure 4.4: Thermogravimetric analyses of extracted phytoliths 33

Figure 4.5: Scanning electron micrographs of silicified cells extracted by wet or microwave digestion 34

Figure 4.6: Preprocessed mean Raman spectra of the most abundant sorghum leaf phytoliths and intensity ratio of the Si-OH to Si-O-Si Raman bands. 36

Figure 4.7: Discrimination between long cell phytoliths extracted by two methods based on Raman microspectroscopy.....38

Figure 4.8: Discrimination of Raman spectra of individual phytoliths extracted by two methods 39

Figure 4.9: Discrimination of Raman spectra of individual phytoliths extracted by SONE 39

Figure 4.10: Discrimination between phytolith types based on the first derivatives of the Raman data shown in Figure 4.9.....40

Figure 4.11: Synchrotron Fourier transform infrared (FTIR) spectra of long and bilobate cells extracted by SONE 41

Figure 4.12: (A) Scores plot of a PCA at the spectral region 2700–3000 cm^{-1} attributed to the organic matter occluded in long (L) and silica (S) cells..... 42

Figure 4.13: Discrimination between phytolith types based on Infrared spectra second derivatives. Synchrotron Fourier transform infrared spectra were collected from long (L) and bilobate (S) cells extracted by SONE.....43

Figure 5.1: Fluorescence microscopy images of leaf cross-sections of sorghum plants grown with and without silicic acid supplementation 50

Figure 5.2: (A) Average Raman spectra of the epidermis, bundle sheath, phloem, sclerenchyma and xylem of sorghum leaves and (B) FTIR spectra of the epidermis, bundle sheath, phloem, sclerenchyma and xylem of sorghum leaves 51

Figure 5.3: Multimodal imaging of a sorghum leaf cross-section grown in absence of silicic acid. 56

Figure 5.4: Multimodal imaging of a sorghum leaf cross-section grown in with silicic acid supplementation. 57

Figure 5.5: Multimodal imaging of a sorghum leaf cross-section grown in absence of silicic acid. 59

Figure 5.6: Multimodal imaging of a sorghum leaf cross-section grown with silicon supplementation. 61

Figure 5.7: Results of the PCA of the Raman data shown in Figure 5.3. 63

Figure 5.8: Results of the VCA of the Raman data shown in Figure 5.3.....64

Figure 5.9: Hierarchical cluster analysis of the Raman data shown in Figure 5.3.....65

Figure 5.10: Results of the PCA of selected spectra from epidermis and sclerenchyma tissues. 67

Figure 5.11: HCA of a Raman map containing sclerenchyma and epidermis.....68

Figure 5.12: PCA results of the vascular tissue comparison after the cluster selection....69

Figure 5.13: Results of the PCA of epidermis spectra selected from four maps, 2 maps for +Si and 2 maps for –Si samples.....70

Figure 5.14: Results of the PCA analysis of spectra classified as sclerenchyma after EMSC correction.....72

Figure 5.15: PCA results of the of the sclerenchyma spectra classified as high fluorescence (F) and low to non-fluorescence (N) 73

Figure 5.16: Average spectra and the second derivative of spectra classified as high fluorescence and non-fluorescence 74

Figure 5.17: Deconvolution analysis of the lignin band. the best deconvolution fitting obtained for 1500 to 1750 cm-1 range for the fluorescence (A) and non-fluorescence (B) average spectra 75

Figure 5.18: Scheme of lignin formation. Canonical monolignols are incorporated into the polymer through different types of bonds marked in the lignin structure by circles.....78

Figure 6.1. Images of samples analysed by nano IR. 84

Figure 6.2: Nano-IR spectra of an extracted phytolith (sorghum biosilica) 86

Figure 6.3: Spectra from microwave extracted phytoliths from different points of the same phytolith and spectra recorded from the epoxy resin 87

Figure 6.4: Silica structures in phytoliths of sorghum leaves.....88

Figure 6.5. Comparison of FTIR spectra (synchrotron FTIR in black and Nano FTIR in red) taken from the cell wall of sorghum leaves 89

Figure 6.6: Images obtained from a resin-embedded wheat awn 91

Figure 6.7: Nano-FTIR absorption spectra taken at positions marked in Figure 6.6 93

Figure 6.8: Broadband spectrally integrated infrared SNOM image of silicified sclerenchyma and nano-FTIR absorption spectra 94

Figure 6.9: Mechanical phase image and profile of the sclerenchyma sample shown in Figure 6.8 96

Figure 6.10: Nano FTIR images and spectra taken from unembedded samples 97

Figure 7.1: Raman spectra of Coniferyl alcohol (CA), Ferulic acid (FA) and synthetic lignin (dehydrogenated polymer) synthesized from CA, and a mixture of CA and FA 103

Figure 7.2: FTIR spectra of arabinoxylan (a), coniferyl alcohol (b) and ferulic acid (c) ..104

Figure 7.3: Infrared spectra of synthetic lignin, silica gel, and silica formed with the synthetic lignin 105

Figure 7.4: Reaction yields of the *in vitro* lignin and silica formation.....106

Figure 7.5: Comparison of silica obtained by silicic acid autopolymerization (SiO2-Auto) and silica precipitated together with the lignin like polymer (SiO2-CAp) 107

Figure 7.6: Infrared spectra of synthetic lignin and SiO2-CAp at 3 and 18 hours.....108

Figure 7.7: Representative Raman spectra of peptide-1 (Pep1), peptide-3 (Pep3), silica precipitates using peptide 1 (Pep1+Si I and Pep1+Si II), silica precipitate using peptide 3 (Pep3+Si) and supernatant recovered from precipitation with peptide I 110

Figure 7.8: FTIR spectra of the silica obtained after precipitation with peptide 1 and peptide 3 111

List of Tables

Table 4.1: Average of silicic acid concentration and standard deviation measured in duplicate from three sorghum plants in sap just after incision and after 4 hours 30

Table 4.2: Raman shifts, IR absorbance maxima and tentative assignment of bands observed in the spectra of extracted phytoliths 37

Table 5.1: Raman bands, assignment to molecular vibration and tentative assignment to cell wall component according to the cited literature 54

Table 5.2: IR absorption bands, assignment to molecular vibration and tentative assignment to cell wall component according to the cited literature 55

Table 5.3: Summary results of the best deconvolution fitting obtained for 1500 to 1750 cm^{-1} range for the fluorescence and non-fluorescence average spectra 76

List of publications

Journal articles discussed in this thesis

- Soukup, M.; **Zancajo, V. M. R.;** Kneipp, J.; Elbaum, R. Formation of root silica aggregates in sorghum is an active process of the endodermis. *Journal of Experimental Botany,* **2019**.

- **Zancajo, V. M. R.;** Diehn, S.; Filiba, N.; Goobes, G.; Kneipp, J.; Elbaum, R. Spectroscopic Discrimination of Sorghum Silica Phytoliths. *Frontiers in Plant Science,* **2019,** *10* (1571).

- **Zancajo, V. M. R.;** Lindtner, T.; Eisele, M.; Huber, A. J.; Elbaum, R.; Kneipp, J. FTIR Nanospectroscopy Shows Molecular Structures of Plant Biominerals and Cell Walls. *Analytical Chemistry,* **2020**.

- **Zancajo, V. M. R.;** Diehn, S.; Elbaum, R.; Kneipp, J. Multimodal analysis and imaging of sorghum leaves. *In preparation*.

Other journal articles

- **Zancajo, V. M. R.;** Brito, J.; Carrasco, M. P.; Bronze, M. R.; Moreira, R.; Lopes, A. Analytical profiles of "legal highs" containing cathinones available in the area of Lisbon, Portugal. *Forensic Science International,* **2014,** *244*, 102-110.

Conference contributions

- **Zancajo**, **V. M. R.;** Soukup, M.; Filiba, N.; Goobes, G.; Emmerling, F.; Kneipp, J.; Elbaum, R. Multimodal structural and functional analysis of sorghum tissues and sorghum biosilica. 1st International Plant spectroscopy conference, 29-30 August 2017, Umeå, Sweden (Abstract & Talk).

- Zeise, I.; Heiner, Z.; Joester, M.; Diehn, S; **Zancajo, V. M. R.;** Emmerling, F.; Elbaum, R.; Kneipp, J.; Analysis of plant tissues using vibrational and other spectroscopic methods and multivariate approaches, FT-IR Spectroscopy in Microbiological and

Medical Diagnostics, 19- 20 October 2017, Berlin, Germany (Abstract & Poster, poster prize).

- **Zancajo**, **V. M. R.;** Diehn, S.; Soukup, M.; Filiba, N.; Goobes, G.; Emmerling, F.; Kneipp, J.; Elbaum, R, Multimodal structural and functional analysis of sorghum tissues and sorghum biosilica, 1st International Plant spectroscopy conference, 24-28 August 2017, Bengaluru, India (Abstract & Talk).

- **Zancajo**, **V. M. R.;** Eisele, M.; Huber, A. J.; Elbaum, R.; Kneipp, J. Nano-FTIR Spectroscopy of in situ and extracted silica phytoliths, 2nd International Plant Spectroscopy Conference 24-28 March 2019, Berlin, Germany (Abstract & Talk).

- **Zancajo**, **V. M. R.;** Lindtner, T.; Diehn, S.; Elbaum, R.; Kneipp, J. "FTIR Microspectroscopy of Organic and Inorganic Components of Plant Cells", FT-IR Spectroscopy in Microbiological and Medical Diagnostics, Berlin, Germany, 10-11.10.2019 (Abstract & Poster, poster prize).

- **Zancajo**, **V. M. R.;** , Diehn, S.; Elbaum, R.; Kneipp, J. "Unravelling Plant Silicification – Using Spectroscopy to Discriminate Between Phytolith Types", "Make and Measure in Analytical Sciences 2019", Berlin, Germany, 25-26.10.2019 (Abstract & Talk).

- **Zancajo**, **V. M. R.;** Eisele, M.; Huber, A. J.; Elbaum, R.; Kneipp, J. "Nano-FTIR Spectroscopy of in Situ and Extracted Silica Phytoliths", 2nd International Plant Spectroscopy Conference (IPSC), Berlin, Germany, 24-28.03.2019 (Abstract & Talk).

- **Zancajo**, **V. M. R.;** Lindtner, T.; Diehn, S.; Elbaum, R.; Kneipp, J. "FTIR Microspectroscopy of Organic and Inorganic Components of Plant Cells", 12th BESSY@HZB User Meeting, Berlin, Germany, 10.12.2020 (Abstract & Poster).

Acknowledgements

I want to express my appreciation to all the people who have directly or indirectly contributed to this work and that has helped me during these years.

I would like to express special gratitude to Prof. Janina Kneipp who has been the best supervisor I could imagine. I am grateful for all her support and enthusiasm, and for all the things I have learned from her during these four years. I feel sincere admiration for her, not only as a scientist but also as a person. I would like to thank also to Prof. Dr Rivka Elbaum, for all her support and motivation. For the guidance she provided me, the fruitful discussions and explanations.

I would like to thank the members of the Kneipp group for the great discussions and friendly environment, especially Sabrina Diehn for all her patience with me and her help with MatLab, and all the conversations and enjoyable time we spent together. To Dr Virginia Merk, a great office companion, for all the chats we had and for the help she provided me. I am also thankful to Tom Linder that together with Sabrina made the BESSY shifts smooth and easy. To Dr Zsuzsanna Heiner for her willingness to help and to Fani, Vesna, Cecilia and Yang for great discussions, all the fun, and great time we spent together, and enjoyable meals we shared. I also thank Annette for all the technical help she always provided.

I would like to acknowledge all the support and help that the members of the Elbaum group provided me during my time at the Hebrew University of Jerusalem, Dr Santosh Kumar, Nerya Zexer and particularly to Dr Milan Soukup for all the explanations, discussions and the time we shared.

I would like to thank Dr Ulrich Schade and Dr Ljiljana Puskar for all the support with the FTIR experiments at BESSY II in Berlin and all other wonderful scientists with whom I have had the unique opportunity of collaborating.

I would also like to extend my gratitude to the SALSA for the funding and to the SALSA team, Katharina Gliege, Katharina Schulthens, Stefanie Sellon, Esther Santel, Kristin Kuschnerik and Pablo Lores Lareo for their help with all the administration work. Also, a big thank you goes to Barbara Franke.

I would like to thank the people in BAM where I performed several experiments, Dr Franziska Emmerling and Dominik. To Jose and Ander for their friendship. To Carsten Prinz, for the innumerable times he helped to solve the issues with my computer. To Ralf Biener who was always willing to help me and to Dr Thomas Schmid for his help troubleshooting instruments and the interesting technical discussions.

In addition, I thank my family, my parents for the support they have provided me during my whole life. And especially to my wife, Suzana Zakovic, my companion in life and science, for all her support, motivation, help and inspiration in this pa

Declaration

I declare that I have completed the thesis independently using only the aids and tools specified. I have not applied for a doctor's degree in the doctoral subject elsewhere and do not hold a corresponding doctor's degree. I have taken due note of the Faculty of Mathematics and Natural Sciences PhD Regulations, published in the Official Gazette of Humboldt-Universität zu Berlin no. 42/2018 on 11/07/2018.
I declare that the written and electronic version of the dissertation written by me in the University Library agrees with the accepted dissertation. I have only remedied the deficiencies and fulfilled the conditions which had been communicated to me in the defense.

…….

Berlin, 29.09.2021